Resistive and electrochemical sensing of Cu^{2+} and Bi^{3+} ion in aqueous solution using Ni_2O_3 and its metal-doped nanostructure

Thesis submitted towards partial fulfillment of the requirements for the award of the Degree of Master of Technology in Nano Science and Technology

By

Sourav Debnath

Registration No: **160446** of **2021-2022**

Class Roll No: **002130701025**

Examination Roll No: **M4NST23020**

Under the guidance of

Professor Chandan Kumar Ghosh

School of Material Science and Nano TechnologyJadavpur University,
Kolkata- 700032, INDIA.

July, 2023

We hereby recommend that the thesis entitled as " **Resistive and electrochemical sensing of Cu^{2+} and Bi^{3+} ion in aqueous solution using Ni_2O_3 and its metal-doped nanostructure** ", prepared by **Mr. Sourav Debnath** (Class Roll No: 002130701025, Registration No: 160446 of 2021-2022, Examination Roll No; M4NST23020) under our guidance, be accepted in partial fulfillment of the requirement for the award of the Degree of Master of Technology in Nano Science and Technology from the School of Material Science and Nano Technology of Jadavpur University.

HOD / Director
Dr. Sourav Sarkar
Director,
School of Material Science & Nano Technology,
Jadavpur University

Thesis Advisor
Dr. Chandan Kumar Ghosh
Professor,
School of Material Science & Nano Technology,
Jadavpur University

Dean-FISLM,
Jadavpur University,
Kolkata – 700032

Acknowledgement

I would like to express my deepest gratitude to my supervisor, Dr. Chandan Kumar Ghosh, Assistant Professor, School of Materials Science and Nanotechnology, Jadavpur University, for his invaluable guidance, expertise, and constant support throughout this research endeavor. His mentorship has been instrumental in shaping this thesis and my growth as a researcher.

I am immensely grateful to Dr. Sayan Dey, Assistant Professor, School of Electrical Sciences, IIT Bhubaneswar, for his continuous support, encouragement, and motivation throughout this journey. His insightful inputs and assistance have been invaluable in overcoming challenges and pushing the boundaries of this research.

I extend my heartfelt thanks to Prof. Prasanta Kumar Guha, Associate Professor, department of Electronics and Electrical Communication Engineering, IIT Kharagpur for providing me with the opportunity to work in his lab through the INUP-i2i program. His trust and support have been instrumental in the successful completion of this work.

I would like to acknowledge and thank all the faculty members of the School of Materials Science and Nanotechnology, Jadavpur University for their valuable insights, constructive feedback, and for fostering an intellectually stimulating research environment.

I am indebted to the members of the Nanolab, including Panchanan Sahoo, Sudip Kundu, Riddhiman Sahoo, Roshni Begum, Raushan Kabir Khan, Aditya Debapriya Gayen, Soumyajit Das, Koninika Biswas, and others, for their collaborative spirit, technical assistance, and stimulating discussions that have enriched my research experience.

I am grateful to the members of the VLSI Lab (Microdevices and System Engineering), Department of Electronics and Electrical Communication Engineering, IIT Kharagpur, including Bidesh Mahata, Abhijit Eshore, Nikita Dey, and Souryadip Roy, for their support and guidance in various aspects of my work.

Lastly, I would like to express my deepest appreciation to my parents and elder sister for their unwavering faith, unconditional love, support, encouragement, and quiet patience throughout my academic journey. Their belief in me has been a constant source of strength and inspiration.

I am grateful to everyone mentioned above, as well as any individuals who have contributed to this research in any way, for their invaluable support, which has been instrumental in the successful completion of this thesis.

-Sourav Debnath

Dedicated to my elder sister

ABSTRACT

Heavy metal ion detection is necessary due to the detrimental effects these pollutants can have on the environment and human health. Cu^{2+} and Bi^{3+} ions, in particular, are known to pose serious risks when present in elevated concentrations in water sources. They can contaminate drinking water supplies, accumulate in ecosystems, and have toxic effects on aquatic life. Therefore, the development of sensitive and reliable sensing platforms for their detection is crucial for effective monitoring, ensuring water safety, and implementing appropriate remediation strategies. This thesis focuses on the detection and analysis of specific heavy metal ions, namely Cu^{2+} and Bi^{3+}, in water samples. The material of choice for this study is Ni_2O_3, which exhibits favourable properties for sensing applications. To enhance its sensing capabilities, Cu and Fe doping were employed on Ni_2O_3. The synthesized materials were characterized using X-ray Diffraction (XRD) and Field Emission Scanning Electron Microscopy (FESEM). XRD analysis provided insights into the crystal structure and phase composition of the materials, while FESEM imaging allowed for the examination of their morphological features and surface characteristics. Following characterization, working electrodes were prepared using Ni_2O_3, and resistive sensors were fabricated by drop-casting pure Ni_2O_3 as well as Ni_2O_3 doped with 5% Fe and Cu^{2+} ions. These sensors were designed to detect and quantify the presence of Cu^{2+} and Bi^{3+} ions in water samples. The performance of the fabricated sensors was evaluated through a series of experiments and measurements. Specifically, electrochemical and resistive sensing techniques were employed. Pure Ni_2O_3 was utilized for electrochemical sensing of Cu, while resistive sensing was employed for both Cu^{2+} sensing using Fe-doped Ni_2O_3 and Bi^{3+} sensing using Cu-doped Ni_2O_3. The results of the experiments demonstrated the efficacy of the Ni_2O_3-based sensors in accurately detecting and quantifying the targeted heavy metal ions. The electrochemical and resistive sensing approaches exhibited promising performance and sensitivity for the detection of Cu^{2+} and Bi^{3+} ions in water samples.

Table of Contents

List of Figures

Figure 5.8: (a) Response time, (b) Amperometric plot, (c) Sensing response and, (d) Selectivity (Cu(II) sensing using pure Ni_2O_3-based sensor)

Figure 5.9: I-V characteristics of pure Ni_2O_3-based sensor during measurement of (a) 10 ppb, (b) 100 ppb, (c) 1 ppm, (d) 10 ppm and, (e) 100 ppm Cu(II) ion

Figure 5.10: (a) Response time, (c) Sensing response and, (d) Selectivity (Cu(II) sensing using 5% Fe-doped Ni_2O_3-based sensor)

Figure 5.11: I-V characteristics of 5 % Fe-doped Ni2O3-based sensor during measurement of (a) 10 ppb, (b) 100 ppb, (c) 1 ppm, (d) 10 ppm and, (e) 100 ppm Cu(II) ion

Figure 5.12: (a) Response time, (b) Amperometric plot, (c) Sensing response and, (d) Selectivity (Bi(III) sensing using 5 % Cu-doped Ni_2O_3-based sensor)

Figure 5.13: I-V characteristics of 5 % Cu-doped Ni_2O_3-based sensor during measurement of (a) 10 ppb, (b) 100 ppb, (c) 1 ppm, (d) 10 ppm and, (e) 100 ppm Cu(III) ion

List of Abbreviations

STM – Scanning Tunneling Microscope

AFM – Atomic Force Microscope

A/F – Air to Fuel

CMOS – Complementary Metal-Oxide Semiconductor

MEMS – Micro-Electromechanical Systems

WHO – World Health Organization

EPA – Environmental Protection Agency

BIS – Bureau of Indian Standards

CBS – Colloidal Bismuth Subcitrate

RBC – Ranitidine Bismuth Citrate

BIS – Bismuth Subsalicylate

CNS – Central Nervous System

PNS – Peripheral Nervous System

GI – Gastrointestinal tract

GU – Genitourinary

AAS – Atomic Absorption Spectroscopy

ICP – Inductively Coupled Plasma spectrometry

XRF – X-ray Fluorescence

NAA – Neutron Activation Analysis

IC – Ion Chromatography

LIBS – Laser-Induced Breakdown Spectroscopy

CV-AAS – Cold Vapor Atomic Absorption Spectroscopy

CV-AFS – Cold Vapor-Atomic Fluorescence Spectroscopy

ICP-OES – Inductively Coupled Plasma-Optical Emission Spectroscopy

ICP-MS – Inductively Coupled Plasma-Mass Spectrometry

HPLC – High-Performance Liquid Chromatography

ppm – parts per million

ppb – parts per billion

NPs – Nanoparticles

GO – Graphene Oxide

CNTs – Carbon Nanotubes

SWASV – Square Wave Anodic Stripping Voltammetry

DMSA – Dimercaptosuccinic Acid

TMDCs – Transition Metal Dichalcogenides

CVD – Chemical Vapor Deposition

DI – Deionized

PEG – Polyethylene Glycol

PVDF – Polyvinylidene Fluoride

NMP – N-methyl-2-pyrrolidone

IDE – Inter Digitated Electrodes

SPM – Scanning Probe Microscopy

XRD – X-Ray Diffraction

FTIR – Fourier Transform Infrared Spectroscopy

CRT – Cathode Ray Tube

FESEM – Field Emission Scanning Electron Microscope

FEG – Field Emission Electron Guns

DNA – Deoxyribonucleic Acid

BSEs – Backscattered Electrons

W-H – Williamson-Hall

SSP – Size-Strain Plot

CV – Cyclic Voltammetry

WE – Working Electrode

RE – Reference Electrode

CE – Counter Electrode

CHAPTER 1

1 Introduction

This chapter provides a concise introduction to chemical sensors, including their history, evolution, and the specific focus on heavy metal ion sensors. It discusses the various parameters used to evaluate sensors and provides an overview of the different types studied to date. The chapter also highlights the motivation of the present work.

1.1 Preamble

In the vast realm of engineering, the development of novel sensors plays a pivotal role in enhancing our understanding of the chemical world and addressing pressing environmental and health concerns. Among the myriad of pollutants that pose a significant threat, heavy metal ions stand out as formidable adversaries due to their toxicity, persistence, and potential to accumulate in various ecosystems.

This thesis delves into the realm of heavy metal ion sensing, aiming to contribute to the ever-growing body of knowledge and advancements in this crucial field. By employing cutting-edge techniques and exploiting the inherent properties of heavy metal ions, this research endeavors to develop an efficient and reliable sensor capable of detecting and quantifying these hazardous species with unprecedented accuracy and sensitivity.

Chemical sensors are devices that can convert a chemical signal into an analytic one. The chemical signal is created through a selective interaction between a sensing material placed in the sensor and a target analyte, and each chemical sensor consists of a sensing element and a transducer. In the context of heavy metal ion sensing, the sensing element is designed to specifically interact with heavy metal ions, allowing for their detection and quantification. The transducer, on the other hand, converts the chemical signal generated by the sensing element into a measurable output, such as an electrical or optical signal.

Building upon this foundation, the subsequent chapters delve into the design, fabrication, and optimization of a novel heavy metal ion sensor. Synthesis and characterization of semiconductor metal oxide explored to engineer a sensing platform capable of selective and efficient detection. The integration of these materials into various

transduction schemes, including electrochemical, optical, or colorimetric methods, is thoroughly investigated to exploit their unique properties for signal generation and analysis.

1.2 Sensors

A sensor is a device capable of detecting changes in physical quantities. The term "sensor" originated from the Latin word "*Sentire*" which means "to feel." In a broader context, it can be regarded as an electronic module that perceives a measurable alteration in its input, which could be in the form of any signal, and then converts it into electrical signals. These electrical signals are subsequently transmitted to the supporting circuitry for further analysis, actuation, output display, and other functions. Sensors are essential in numerous aspects of daily human life, ranging from motion and proximity sensors in elevators to the multitude of sensors found in aircraft cockpits, responsible for monitoring altitude, roll, pitch, vertical speed, and various other parameters. Depending on the nature of the input they respond to, sensors can be optical (based on light), tactile (based on touch), piezoelectric (based on pressure), chemical (based on chemical reactions), thermal (based on temperature), and so on. Sensors have been in existence for a considerable period, taking various forms and finding application in diverse fields.

Sensors can be categorized into various types based on their sensing technique and output characteristics. The different classifications are as follows:

- Chemoresistive
- Conductometric
- Capacitive
- Optical
- Piezoresistive
- Colorimetric
- Electrochemical

Both chemoresistive and electrochemical type sensors come under the type of chemical sensor.

1.3 Chemical sensors: A brief history and evolution

Humans have always experienced the world through sensory organs to get information of its surroundings. This involved the use of sensory organs, such as taste and smell, to discern the presence of certain compounds. Humans are capable of identifying and discerning between an estimated 10,000 scents or more, while only possessing 400 olfactory receptors [1]. These primitive methods laid the foundation for the development of more sophisticated sensor technologies.

In the late 18th and early 19th centuries, significant advancements occurred. Sir Humphry Davy, a British chemist, developed his safety lamp for miners around 1815. It employs his discovery that wire mesh can disseminate heat rapidly enough to prevent a candle's heat from igniting methane gas. The flame would turn bluer and brighter around methane, and would dim or extinguish around too little oxygen. The Davy lamp gave miners a way to detect dangerously low levels of oxygen, and reduced the possibility of explosions, saving an incalculable number of lives. In the late 18th and early 19th centuries, significant advancements occurred in chemical analysis [2]. Swedish chemist Carl Wilhelm Scheele developed a chemical test to detect arsenic in corpses in 1773 [3]. His work was further elaborated by German chemist Valentin Ross in 1806 to detect poison in stomach walls. In 1836, Scottish chemist James Marsh did the first application of this as a forensic science technique [4]. The first example of a fluorescent chemosensor can be documented to be that of Friedrich Goppelsroder, who in 1867, developed a method for the determination/sensing of aluminium ion, using fluorescent ligand/chelate [5].

In the speech titled "There's Plenty of Room at the Bottom" delivered at the American Physical Society in 1959, Richard Feynman introduced the concept of manipulating matter at the atomic level, which subsequently spurred the development of micro and nanotechnology [6]. From then research in the area of modern electronic chemical sensors began to gain momentum in the 1960s with the demonstration of metal-oxide semiconductor sensors capable of sensing oxygen [7]. Since the 1970s, the microelectronic chemical sensor has been explored as a low-cost alternative chemical sensing methods when the Titania based sensor was primarily used to detect stoichiometric air-to-fuel (A/F) ratio [8]. From the invention of the transistor by Bell lab researchers Walter Brattain, John Bardeen, and William Shockley in 1947, the electronic industry has experienced rapid technological advances. In 1956, they

were all awarded the Nobel Prize in Physics [9]. In 1981, the scanning tunneling microscope (STM) was developed, followed by the atomic force microscope (AFM) in 1986, pioneered by IBM research teams in Zurich led by Binnig and Rohrer. In recognition of their contributions, they were awarded the Nobel Prize in Physics in 1986 [10, 11]. These breakthroughs facilitated the development of products at the nanometer scale, leading to the emergence of nanoscience and technology. Subsequently, the discovery of nanotubes [12], and graphene [13] opened up new possibilities for the production of low-cost and robust chemosensors. These advancements have revolutionized the field of sensing by enabling highly sensitive and efficient detection systems.

1.4 Heavy metal ion sensor

A heavy metal ion sensor is a chemical sensor employed to detect the presence of heavy metal ions in drinking water, ensuring compliance with safety standards. Monitoring and removing heavy metals such as Cd(II), Hg(II), Cr(VI), As(V), Cr(III), Cu(II), and Bi(III) is crucial as they tend to accumulate in the food chain and can enter living systems through food and drinkable water [14]. Heavy metal ion sensors come in various types, including optical, electrochemical, and semiconducting materials-based sensors [15-18]. Optical methods provide accurate measurements but are costly, require skilled professionals for operation, and are bulky, limiting their everyday use [19]. Electrochemical sensors, on the other hand, utilize liquid electrolytes, which make them unsuitable for routine heavy metal ion detection by the general public. Their usage necessitates proper training and the expertise of skilled professionals.

1.5 Sensor parameters

The efficiency of a chemical sensor is evaluated in terms of several parameters. All the parameters are discussed below in detail:

Response **-** It is the ratio of the baseline resistance of the device when exposed to the solvent (without analyte) (R_{base}) to the resistance during exposure to the analyte ($R_{analyte}$) of the device. This definition is valid when the resistance of the sensor increases or decreases after interacting with the target analyte and the change in resistance is huge.

$$Response\ (in\ times) = \frac{R_{base}}{R_{analyte}} \qquad (1.1)$$

Sensitivity - Sensitivity is defined as a change of output with respect to a change in input. If Δy and Δx respectively change in output and input, then sensitivity can be written as:

$$Sensitivity = \frac{\Delta y}{\Delta x} \qquad (1.2)$$

Response time ($t_{90\%}$) **-** The time taken by a sensor to reach 90% of its maximum response against a particular concentration of analyte is known as its response time. A sensor with a very short response time is desired for many practical applications.

Recovery time ($t_{10\%}$) - It is the time required by the sensor to reach 10% of its initial state (base resistance) after sensing a particular concentration of analyte. An efficient sensor should be able to fast recover to its baseline.

Selectivity - Selectivity refers to the ability of a sensor to respond to a specific analyte in a measurable manner, distinguishing it from other similar analytes present in a mixture. If a sensor exhibits a response to a group of analytes or all analytes in the mixture, its selectivity is considered poor. On the other hand, a good sensor demonstrates high selectivity, meaning its response is significantly higher for the target analyte compared to other analytes. Selectivity is typically evaluated based on the magnitude of response, where the sensor's response to the target analyte is notably higher than that of other analytes. While practical sensors may exhibit non-zero responses to other analytes, these responses are generally much lower in comparison to the target analyte for which the sensor displays selectivity.

Apart from the above parameters, sensors are also evaluated in ***operating voltage*** and ***temperature***; a sensor should be operated at near room temperature and under comparatively lower voltages. This would improve the power and energy budget of the device; cost; a chemosensor is expected to be very cost-efficient (this can be achieved by using (i) low-cost fabrication techniques for sensing materials, (ii) batch fabrication of devices. i.e., if many sensor devices can be fabricated simultaneously, (iii) low-cost substrate, and (iv) sensor and interface electronics on the same die, e.g., this is possible if the sensor can be developed in a commercial foundry using CMOS-MEMS process steps); ***lifetime*** should be reasonably long (a couple of years, but it depends on the application); ***linearity***; the response of a good sensor increase or decreases output linearly; also, a sensor should not show ***hysteresis*** in its response.

1.6 Motivation for the work

The detection and monitoring of heavy metal ions in various environmental matrices, such as drinkable water, have become crucial due to their detrimental effects on human health and the ecosystem. Among these heavy metal ions, Copper (Cu^{2+}) [20, 21] and Bismuth (Bi^{3+}) [22-24] are of particular concern due to their widespread presence and potential toxicity. Developing efficient and reliable sensors for the selective detection of these ions has become an urgent research priority. In this context, the use of semiconducting materials as sensing elements presents a promising avenue for heavy metal ion sensing. Semiconductors offer unique properties that can be tailored to selectively interact with specific target ions, providing a basis for sensitive and specific detection. Metal oxide semiconductors, in particular, have demonstrated potential for heavy metal ion sensing due to their tunable properties, stability, and compatibility with sensor fabrication processes [25-31].

Motivated by the need for accurate and selective heavy metal ion sensing, this work focuses on the development of a novel sensor using doped metal oxides as the sensing material. By harnessing the unique properties of these semiconducting materials, we aim to design a sensor capable of effectively detecting and quantifying Cu^{2+} and Bi^{3+} ions in complex samples, such as drinkable water. The motivation behind this research stems from the urgent demand for cost-effective, robust, and portable heavy metal ion sensors. Current detection methods often rely on expensive and complex instrumentation, limiting their accessibility and practicality. By leveraging the properties of semiconducting materials and exploring doping strategies, we envision the development of a sensor that can address these challenges. The successful realization of a Cu^{2+} and Bi^{3+} ion sensor using semiconducting materials holds great potential for a range of applications, including environmental monitoring, industrial process control, and ensuring the safety of drinkable water. By providing accurate and real-time detection capabilities, this research aims to contribute to the protection of public health and the preservation of ecosystems.

References

[1] K. J. Albert, D. R. Walt, D. S. Gill, and T. C. Pearce, "Optical multibead arrays for simple and complex odor discrimination," Analytical Chemistry, vol. 73, no. 11, pp. 2501-2508, 2001.

[2] J. M. Thomas, "Sir Humphry Davy and the coal miners of the world: A commentary on Davy (1816)'An account of an invention for giving light in explosive mixtures of fire-damp in coal mines'," Philosophical Transactions of the Royal Society A: Mathematical, Physical and Engineering Sciences, vol. 373, no. 2039, p. 20140288, 2015.

[3] S. Bell, Drugs, poisons, and chemistry. Infobase Publishing, 2009.

[4] W. B. Jensen, "The marsh test for arsenic," Notes from the Oesper Collections May/June, 2014.

[5] D. Wu, A. C. Sedgwick, T. Gunnlaugsson, E. U. Akkaya, J. Yoon, and T. D. James, "Fluorescent chemosensors: the past, present and future," Chemical Society Reviews, vol. 46, no. 23, pp. 7105-7123, 2017.

[6] G. Stylios, "There is plenty of room at the bottom, RP Feynman," International Journal of Clothing Science and Technology, vol. 25, no. 5, 2013.

[7] T. Seiyama, K. Fujiishi, M. Nagatani, and A. Kato, "A new detector for gaseous components using zinc oxide thin films," J. Soc. Chem. Ind. Japan, vol. 66, no. 5, pp. 652-655, 1963.

[8] A. Cederquist, E. Gibbons, and A. Meitzler, "Characterization of zirconia and titania engine exhaust gas sensors for air/fuel feedback control systems," SAE Technical Paper, 0148-7191, 1976.

[9] W. F. Brinkman, D. E. Haggan, and W. W. Troutman, "A history of the invention of the transistor and where it will lead us," IEEE journal of solid-state circuits, vol. 32, no. 12, pp. 1858-1865, 1997.

[10] C. Quate, C. Gerber, and C. Binnig, "Atomic force microscope," Phys. Rev. Lett, vol. 56, no. 9, pp. 930-933, 1986.

[11] G. Binnig and H. Rohrer, "Scanning tunneling microscopy—from birth to adolescence," reviews of modern physics, vol. 59, no. 3, p. 615, 1987.

[12] S. Iijima, "Helical microtubules of graphitic carbon," nature, vol. 354, no. 6348, pp. 56-58, 1991.

[13] A. K. Geim and K. S. Novoselov, "The rise of graphene," Nature materials, vol. 6, no. 3, pp. 183-191, 2007.

[14] M. Li, H. Gou, I. Al-Ogaidi, and N. Wu, "Nanostructured sensors for detection of heavy metals: a review," ed: ACS Publications, 2013.

[15] A. Nigam, N. Sharma, S. Tripathy, and M. Kumar, "Development of semiconductor based heavy metal ion sensors for water analysis: A review," Sensors and Actuators A: Physical, vol. 330, p. 112879, 2021.

[16] X. Xu, S. Yang, Y. Wang, and K. Qian, "Nanomaterial-based sensors and strategies for heavy metal ion detection," Green Analytical Chemistry, vol. 2, p. 100020, 2022.

[17] A. G.-M. Ferrari, P. Carrington, S. J. Rowley-Neale, and C. E. Banks, "Recent advances in portable heavy metal electrochemical sensing platforms," Environmental Science: Water Research & Technology, vol. 6, no. 10, pp. 2676-2690, 2020.

[18] U. O. Aigbe et al., "Electrochemical Detection of Heavy Metals," Modified Nanomaterials for Environmental Applications: Electrochemical Synthesis, Characterization, and Properties, pp. 25-63, 2022.

[19] M. E. Mahmoud, I. Kenawy, M. A. Hafez, and R. Lashein, "Removal, preconcentration and determination of trace heavy metal ions in water samples by AAS via chemically modified silica gel N-(1-carboxy-6-hydroxy) benzylidenepropylamine ion exchanger," Desalination, vol. 250, no. 1, pp. 62-70, 2010.

[20] M. R. Awual, M. Ismael, M. A. Khaleque, and T. Yaita, "Ultra-trace copper (II) detection and removal from wastewater using novel meso-adsorbent," Journal of Industrial and Engineering Chemistry, vol. 20, no. 4, pp. 2332-2340, 2014.

[21] B. R. Stern, "Essentiality and toxicity in copper health risk assessment: overview, update and regulatory considerations," Journal of Toxicology and Environmental Health, Part A, vol. 73, no. 2-3, pp. 114-127, 2010.

[22] R. Somphonsane, T. Chiawchan, W. Bootsa-ard, and H. Ramamoorthy, "CVD Synthesis of MoS2 Using a Direct MoO2 Precursor: A Study on the Effects of Growth Temperature on Precursor Diffusion and Morphology Evolutions," Materials, vol. 16, no. 13, p. 4817, 2023.

[23] M. Legrand et al., "Alpine-ice record of bismuth pollution implies a major role of military use during World War II," Scientific Reports, vol. 13, no. 1, p. 1166, 2023.

[24] R. Wang, H. Li, and H. Sun, "Bismuth: environmental pollution and health effects," Encyclopedia of environmental health, p. 415, 2019.

[25] Y. Deng and Y. Deng, Sensing mechanism and evaluation criteria of semiconducting metal oxides gas sensors. Springer, 2019.

[26] S. Dey, S. Santra, S. K. Ray, and P. K. Guha, "Fe x Ni (1-x) O/NiO Heterojunction-Based Selective VOC Sensor Device by Using Temperature Tunability," IEEE Sensors Journal, vol. 20, no. 14, pp. 7503-7508, 2019.

[27] S. Dey, S. Nag, S. Santra, S. K. Ray, and P. K. Guha, "Voltage-controlled NiO/ZnO p–n heterojunction diode: A new approach towards selective VOC sensing," Microsystems & nanoengineering, vol. 6, no. 1, p. 35, 2020.

[28] S. Dey, S. Santra, A. Midya, P. K. Guha, and S. K. Ray, "Synthesis of $Cu_xNi_{(1-x)}$ O coral-like nanostructures and their application in the design of a reusable toxic heavy metal ion sensor based on an adsorption-mediated electrochemical technique," Environmental Science: Nano, vol. 4, no. 1, pp. 191-202, 2017.

[29] I. Singh, S. Dey, S. Santra, K. Landfester, R. Muñoz-Espí, and A. Chandra, "Cerium-doped copper (II) oxide hollow nanostructures as efficient and tunable sensors for volatile organic compounds," ACS omega, vol. 3, no. 5, pp. 5029-5037, 2018.

[30] S. Dey, S. Santra, S. Sen, D. Burman, S. K. Ray, and P. K. Guha, "Photon-assisted ultra-selective formaldehyde sensing by defect induced NiO-based resistive sensor," IEEE Sensors Journal, vol. 18, no. 14, pp. 5656-5661, 2018.

CHAPTER 2

2 Review of the literature

This chapter explores the topic of heavy metal ions, including their sources and the associated toxicity. It discusses the limitations of conventional detection methods for heavy metal ions. Furthermore, it highlights ongoing research efforts in the development of nanomaterials-based sensors for heavy metal ions. The chapter also provides detailed insights into various fabrication techniques and the selection of sensitive materials used in previous studies as the sensing layer.

2.1 Heavy metals: Introduction and a brief history

The term heavy metal has been widely used as a group of metals and metalloids. These elements have relatively high densities, atomic weights, and atomic numbers [1]. Generally, the density ranges from 3.5 g/cm^3 to above 7 g/cm^3 [2]. The term "heavy metal" first appeared in 1817, when German chemist Leopold Gmelin classified the elements into nonmetals, light metals, and heavy metals [3]. Heavy metals like Mercury (Hg), Lead (Pb), Arsenic (As), Cadmium (Cd), and Chromium (Cr) have been reported. These heavy metals also often interact with biological and chemical ligands that contain sulfur, nitrogen, and oxygen to create complexes. As a result, the protein molecular structural changes, enzyme inhibition, and hydrogen bond breakage are all possible. Thus, these intricate heavy metal formations can potentially cause cancer and have negative consequences on the kidneys, liver, skin, bones, teeth, and the central nervous system (CNS) [4]. For metabolism, a small amount of several heavy metals, are necessary for living things [5]. Essential nutrients needed for various metabolic processes include heavy metals including iron (Fe), chromium (Cr), copper (Cu), cobalt (Co), manganese (Mn), molybdenum (Mo), magnesium (Mg), nickel (Ni), and zinc (Zn) [6, 7].

2.2 Sources of heavy metal ions and their toxicity

In recent years, there has been a growing global public health concern associated with the environmental damage by these metals. Additionally, human exposure has increased dramatically due to an exponential increase in their use in several industrial, agricultural,

domestic, and technological applications [8]. Reported sources of heavy metals in the environment include geogenic, industrial, agricultural, pharmaceutical, domestic, and atmospheric effluents [9]. Environmental pollution is very significant in point source operations such as mining, smelters, and other industrial operations based on [8-10].

Due to their toxic, carcinogenic, and non-biodegradable characteristics, heavy metal ions are typically known as an environmental health risk. They can quickly accumulate in the ecosystem via the food chain and have a negative impact on human health. As soon as heavy metal ions are present in the body, complexes that form with proteins allow them to interfere with cellular functions. This disturbance can cause toxicity, organ failure, and cancer [11]. Many health organizations throughout the world have set permitted limits in their guidelines for the presence of heavy metal ions in water due to their toxicity and carcinogenic behaviour. In order to detect harmful heavy metal ions below the allowable limits, several research groups are focusing on developing efficient sensing techniques [12-16]. Table 2.1 lists sources of heavy metals, their health consequences, and the maximum permitted limits of several heavy metal ions set by the World Health Organization (WHO), Environmental Protection Agency (EPA), and Bureau of Indian Standards (BIS).

Table 2.1: Standard values of the maximum permissible limit of heavy metal ions in drinking water recommended by the WHO, EPA, and BIS [4,17,18]

Heavy metal ions	Standard guideline values (in ppm)		
	WHO	**EPA**	**BIS**
As^{3+}	0.01	0.01	0.01
Cd^{2+}	0.003	0.005	0.003
Cr^{3+}	0.05	0.1	0.05
Cu^{2+}	2	1.3	0.05
Pb^{2+}	0.01	0.015	0.01
Hg^{2+}	0.001	0.002	0.001
Bi^{3+}	-	-	-

The analysis of the environmental occurrence, resources, potential for human exposure, and worldwide impact of some of the highly toxic heavy metal ions like lead, mercury, cadmium, arsenic, bismuth, copper, and chromium are described as follows.

2.2.1 Lead (Pb)

Lead (Pb) is a commonly found heavy metal in the environment, present in various sources such as hair dye, ores, sanitary materials, pipes, mining sites, fertilizer, paints, drinking water, and food [19]. Industries like electroplating, electrical, steel, and explosive manufacturing contribute to the release of Pb into the environment through water, directly impacting both surface and groundwater [20]. Pb is highly hazardous, causing irreversible damage to the nervous system, neurodegenerative diseases, cardiovascular and developmental disorders, kidney damage, hyperirritability, decreased bone growth in children, and various blood-related issues [19]. Elevated levels of Pb^{2+} adversely affect soft tissues and organs, potentially leading to cancer. Prolonged exposure to Pb in the bloodstream can result in coma and even death [11,19, 21, 22].

Due to its toxicity, the World Health Organization (WHO) and Environmental Protection Agency (EPA) have set maximum permissible limits for Pb^{2+} ions in drinking water at 10 ppb and 15 ppb, respectively [23, 24]. Studies have shown that adults absorb around 35-50% of Pb^{2+} through drinking water, with absorption rates exceeding 50% in children [6]. A survey conducted in Mexico to detect heavy metal ions in water revealed that approximately 43% of the samples exceeded the acceptable limit for Pb [25,26]. Therefore, monitoring the concentration of Pb^{2+} ions in water resources is crucial to mitigate its hazardous impacts on human health.

2.2.2 Mercury (Hg)

Mercury (Hg) is a widespread environmental toxin found in three different forms: elemental, organic, and inorganic, each with its own level of toxicity in the environment [27]. Elemental mercury is a liquid at room temperature. Humans can be exposed to mercury through various sources, both direct and indirect, including food contamination, medical and dental procedures, and agricultural activities. Industries such as plastic, chloro-alkali, paper and pulp, pharmaceuticals, and oil refineries also contribute to mercury and its compound discharges into water resources [20,11,28]. Additionally, mercury can contaminate water through natural off-gassing from the earth's crust and enter the food chain through fish and shellfish [29,30]. Increased exposure to mercury has adverse effects on the gastrointestinal tract and can easily cross the placental and blood-brain barriers due to its lipid solubility [6].

Even small amounts of mercury in water can affect the kidneys, reproductive and respiratory systems, the brain, neurological tissues, and the liver [12].

2.2.3 Cadmium (Cd)

Cadmium is a naturally occurring heavy metal found in sedimentary rocks, marine phosphates, and industrial effluents. It is highly toxic and commonly used in alloys, plating, cadmium-nickel batteries, pigments, fertilizers, and stabilizers [20]. Small amounts of cadmium can also be found in certain foods such as potatoes, leafy vegetables, grains, seeds, and mollusks [31]. The toxicity of cadmium and its compounds is significant even at low concentrations. It can cause hepatic toxicity, lung cancer, and various diseases, severely impacting the respiratory system, kidneys, liver, and reproductive organs [32,33].

Cadmium easily accumulates in the food chain through farming practices. Industries often discharge cadmium-contaminated waste into natural water resources like rivers, which are then used by farmers for crop irrigation. This allows cadmium to enter the food chain, posing a threat to human health. A well-known example is the "Itai-Itai" disease in Japan, where cadmium accumulation in the river caused bone softening, fractures, and skeletal damage in humans [34]. In Japan, the Jinzu River was contaminated with cadmium from the Kamioka Zinc Mine, leading to various kidney-related problems among the affected population [35]. In 2013, the Chinese government conducted tests on rice samples in South China, revealing contamination with cadmium [36]. Therefore, there is a need for an on-site and economically viable detection method to remove cadmium from water sources.

2.2.4 Arsenic (As)

Arsenic is a highly toxic heavy metal that is widely present in the environment. It exists mainly in the forms of trivalent and pentavalent arsenate. Environmental pollution from arsenic occurs naturally through soil erosion and volcanic eruptions. Numerous agricultural industries produce products such as herbicides, insecticides, algicides, wood preservatives, and dyes that contain high levels of arsenic compounds. Arsenic and its compounds have also been used in the medical field to treat conditions such as African sleeping sickness, syphilis, amoebic dysentery, and trypanosomiasis. Veterinary applications of arsenic-based drugs include treating parasitic diseases, blackheads in turkeys, filariasis in dogs, and tapeworm eradication in cattle [6, 37].

Human exposure to high concentrations of arsenic in drinking water can lead to various health issues, including cardiovascular and peripheral vascular diseases, diabetes, hearing loss, neurological and neurobehavioral disorders, hematological disorders like anemia and leukopenia, and cancer [7,37]. Several areas with arsenic pollution have reported higher mortality rates for cancers of the skin, bladder, and liver [38,39]. Industries involved in ceramic and pesticide production, metallic ore refining, and wood preservation discharge elevated levels of arsenic into the water, directly impacting the surrounding environment [11].

Numerous studies have highlighted the toxicity of arsenic and its impact on human health in various countries such as India, Bangladesh, Iran, Brazil, China, Taiwan, Thailand, Mexico, Chile, Finland, Argentina, Vietnam, and Hungary [6, 40-44]. In Bangladesh, the groundwater in 50 districts exceeded the standard limits set by the World Health Organization (WHO), Environmental Protection Agency (EPA), and Bangladesh itself, affecting approximately 40 million people, particularly in the floodplain and deltaic regions [45,46]. Studies have also found elevated arsenic concentrations in groundwater samples from Makkah, Saudi Arabia, where 42% of samples exceeded the WHO standard value of 10 µg/L [47]. Additionally, arsenic concentrations in grounded drinking water ranged from 0.1 to 1340 µg/L in Cambodia and the neighboring Mekong Delta floodplains of Southern Vietnam. In the Sonitpur district of Assam, India, drinking water from tea gardens contained arsenic concentrations of up to 90 µg/L. Surface water samples collected from the Patancheru industrial town in Hyderabad, Telangana, India, showed high arsenic concentrations (average: 29.2 µg/L) generated by pharmaceutical, fertilizer, paint, and pesticide industries. Groundwater samples collected from the same location exhibited even higher arsenic concentrations (average: 146.5 µg/L) due to migration from surface water and geogenic contamination [48]. These reports indicate that approximately 37% of groundwater and drinking water sources exceed the standard acceptable limit for arsenic [25,49]. Thus, there is a need for arsenic detection in drinking water to ensure it falls below the maximum permissible limits set by the WHO.

2.2.5 Copper (Cu)

Copper is a highly toxic metal at elevated concentrations in water. However, a small amount of copper is necessary for enzyme synthesis and bone development in humans [50]. In the environment, copper is present in various forms, including metallic copper (Cu^0),

cuprous copper (Cu^{+}), and cupric copper (Cu^{2+}). Among these forms, Cu^{2+} is more abundant and toxic [51]. Copper plays a crucial role in the functioning of oxidative stress-related enzymes such as cytochrome c oxidases, superoxide dismutase, catalase, peroxidase, ferroxidases, monoamine oxidase, and dopamine β-monooxygenase [51,52]. It is also involved in the activity of metalloenzymes required for carbohydrate metabolism, hemoglobin formation, and hair keratin synthesis [6].

However, copper can be potentially toxic due to the transition between Cu^{2+} and Cu^{+}, leading to the formation of superoxide and hydroxyl radicals. Excessive intake of copper can result in cellular damage and contribute to conditions such as Wilson's disease, Alzheimer's disease, Parkinson's disease, and even death [50]. Major sources of copper include metallurgy and mining industries, steel industries, chemical manufacturing, paints, fertilizers, and electroplating [53,54]. While copper is highly toxic at higher concentrations and essential at lower concentrations for nutrition, it is crucial to detect copper levels below the specified limits set by the World Health Organization (WHO) and other standards.

2.2.6 Bismuth (Bi)

Bismuth, despite its long history of use, remains one of the least understood elements in the periodic table. It has found widespread application in the manufacturing of alloys, pigments, cosmetics, and pharmaceuticals. Bismuth is considered a "green" heavy metal and has been used as a substitute for lead in certain industries to address environmental concerns related to heavy metal pollution. In the field of healthcare, bismuth-based drugs such as colloidal bismuth subcitrate (CBS), ranitidine bismuth citrate (RBC), bismuth subsalicylate (BSS), bismuth iodoform, and radioactive bismuth ($^{212}Bi/^{213}Bi$) complexes have been developed and utilized to treat various diseases. These bismuth therapies generally exhibit high efficacy with minimal side effects. However, there have been reported cases of bismuth toxicity resulting from excessive bismuth dosage [135]. Bismuth compounds have low solubility, leading to poor absorption in the body, with an absorption rate of approximately 0.2%. The majority of ingested bismuth, about 90%, is excreted through urine, resulting in the highest concentration of bismuth being found in the kidneys. The elimination half-life of bismuth is approximately 21 days. Long-term exposure to bismuth toxicity primarily affects the central nervous system and behavior, suggesting the accumulation of bismuth in lysosomes and specific cells such as those in the reticular, hypothalamic, oculomotor,

hypoglossal, and Purkinje regions. Bismuth distribution in the body seems to occur through axonal transport [134,136].

2.2.7 Chromium (Cr)

Chromium (Cr) is the seventh most abundant element on Earth and is naturally present in various oxidation or valence states in the earth's crust. Chromium ions range from Cr^{2+} to Cr^{6+} in terms of availability, with Cr^{3+} being the most stable form and Cr^{6+} being the second most stable form [55]. The major sources of chromium in water are metallurgical, refractory, and chemical industries. While Cr^{3+} compounds are naturally occurring, Cr^{6+} compounds are primarily of anthropogenic origin. However, there have been reports of natural occurrences of Cr^{6+} compounds in ground and surface waters, exceeding the World Health Organization's (WHO) drinking water limit of 50 ppb for Cr^{6+} [56]. It is worth noting that Cr^{3+} compounds are generally less toxic than Cr^{6+} compounds. Cr^{3+} is actually an essential nutrient that plays a key role in metabolic activities.

On the other hand, Cr^{6+} compounds are known to cause various health issues, including irritation, ulcers in the stomach and small intestine, anemia, damage to sperm, and male reproductive system impairment. Increased incidence of stomach tumors has also been observed in individuals exposed to Cr^{6+} through drinking water. Accidental or intentional exposure to high concentrations of Cr^{6+} can lead to renal, cardiovascular, gastrointestinal, hepatic, hematological, and neurological effects, potentially resulting in death or long-term complications even in those who survive with medical treatment [57-59]. Given the severe health effects associated with Cr^{6+} exposure, it is crucial to detect its presence in drinking water and ensure it remains below the permissible limits set by the WHO.

The types of heavy metals, their major sources, and their effect on human health are summarized in Table 2.2.

Table 2.2: Major sources of heavy metal ion and their impact on human health

Heavy metal ions	Major sources	Effects on human health
Lead (Pb)	Solder joints, paint, airborne Pb from gasoline combustion, PVC pipes in sanitation, agriculture, jewelry lead batteries, lunch boxes	The nervous system, kidneys. Highly toxic to infants and pregnant women. Brain damage, Alzheimer's disease, Senile Dementia, kidney damage, decreased bone growth, behavioral issues, ataxia, hyperirritability, and stupor
Mercury (Hg)	Combustion of coal, municipal solid waste incineration, fisheries, volcanic emissions, and paint paper manufacture, used in fungicides, rock, and hydrothermal areas	The nervous system, Impaired neurologic development, effects on the digestive system, immune system, lungs, kidneys, skin and eyes, Minamata, acrodynia, salivation increment, hypotonia, hypertension, kidneys problems
Cadmium (Cd)	Paints, pigments, electroplated parts, batteries, plastics, synthetic rubber, photographic and engraving process, photoconductors and photovoltaic cells, abandoned mines, rocks.	Renal toxicity, hypertension, weight loss, fatigue, microcytic hypochromic anemia, lymphocytosis, pulmonary fibrosis, atherosclerosis, peripheral neuropathy, lung cancer, osteomalacia, osteoporosis, and hyperuricemia, kidney-related problems, hypertension, anemia, liver, Skeleton banding, ITAI-ITAI diseases

Arsenic (As)	Pesticides, industrial wastes, smelter operations, rocks, wooden electricity poles that are treated with arsenic-based preservatives, pesticides, fertilizers, the release of untreated effluents, oxidation of pyrite (FeS) and arseno pyrite (FeAsS)	Causes effects on the central nervous system (CNS), peripheral nervous system (PNS), cardiovascular, pulmonary diseases, gastrointestinal tract (GI), genitourinary (GU), hemopoietic, dermatologic, foetal and teratogenic diseases, anorexia, brown pigmentation, hyper-pigmentation, localized edema, and skin cancer
Copper (Cu)	Fertilizers, tanning, and photovoltaic cells	Adreno-cortisol hyperactivity, allergies, anemia, alopecia, arthritis, autism, cystic fibrosis, diabetes, hemorrhaging, and kidney disorders
Bismuth (Bi)	Cosmetic products, medication, Hair dyes, wart treatments, burn ointments, antiseptic powders, dentistry, coal burning, non-ferrous smelters, and production of aluminum, steel and alloys	Neurological decline, kidney disease, gastrointestinal spasms, and anemia
Chromium (Cr)	Abandoned mines, electroplating, leather industry, tanning, and chrome plating industries	Reproductive toxicity, embryotoxicity, teratogenicity, mutagenicity, carcinogenicity, lung cancer, dermatitis, skin ulcers, perforation of the septum, irritant contact dermatitis, liver, and kidney effects

2.3 Conventional methods of heavy metal ion detection

The conventional determination of heavy metals in is achieved by means of standard spectroscopic techniques such as Atomic Absorption Spectroscopy (AAS), Inductively Coupled Plasma spectrometry (ICP), Laser-Induced Breakdown Spectroscopy (LIBS), X-ray Fluorescence (XRF), Neutron Activation Analysis (NAA), Ion Chromatography (IC). All the methods have been described below.

2.3.1 Atomic Absorption Spectroscopy (AAS)

Atomic absorption spectroscopy (AAS) is a widely utilized technique for the trace determination of heavy metal ions in various sample types. It enables the analysis of a single element per determination [60]. Additionally, cold vapor-atomic fluorescence spectroscopy (CV-AFS) and cold vapor AAS (CV-AAS) are employed for similar purposes.

2.3.2 Inductively Coupled Plasma spectrometry (ICP)

Inductively coupled plasma spectrometry (ICP) is a versatile technique used for analyzing multiple elements. It can be categorized into two methods: inductively coupled plasma-optical emission spectroscopy (ICP-OES) [61] and inductively coupled plasma-mass spectrometry (ICP-MS) [62].

2.3.3 Laser-Induced Breakdown Spectroscopy (LIBS)

Laser-induced breakdown spectroscopy (LIBS) is a flexible and adaptable method that allows for the quick analysis and monitoring of heavy metals in water. This technique enables the identification of elements present in water by utilizing their unique spectral signatures [63]. LIBS offers a rapid and non-destructive approach to elemental analysis, making it suitable for various applications such as environmental monitoring, industrial quality control, and research.

2.3.4 X-ray Fluorescence (XRF)

X-ray fluorescence (XRF) is a method of analyzing the elemental composition of a sample. It involves using X-ray tubes to generate primary excitation sources, which in turn induce the emission of X-ray photons with specific wavelengths from the elements present in

the sample. These emitted X-ray photons are then detected and analyzed using specialized detectors [17]. This technique allows for the identification and quantification of the elements within the sample based on their characteristic X-ray emissions.

2.3.5 Neutron Activation Analysis (NAA)

Neutron activation analysis (NAA) is a highly sensitive method used to measure the concentrations of various heavy metals. This technique combines the sensitivity of neutron irradiation with the analysis of emitted radiation from the radioactive sample. By examining the spectra of the emitted radiation, the concentrations of different elements can be determined [18]. NAA is particularly useful in detecting trace amounts of heavy metals in samples due to its exceptional sensitivity.

2.3.6 Ion Chromatography (IC)

Ion chromatography (IC) is a straightforward method used for the simultaneous analysis and quantification of heavy metal ions in solution. It is a high-performance liquid chromatography (HPLC) technique that employs ion exchange resins to determine multiple ionic species in aqueous solutions, even at parts per million (ppm) and parts per billion (ppb) levels. IC offers distinct advantages over spectroscopic methods when it comes to cation analysis [65]. This technique is particularly advantageous in accurately detecting and measuring heavy metal ions in various environmental, industrial, and biological samples.

All the conventional heavy metals detection methods and their merits and demerits have been shown in Table 2.3

Table 2.3: Conventional techniques of heavy metal ion detection and their merits and demerits

Method	Merits	Demerits	References
Atomic Absorption Spectroscopy (AAS)	• Cheapness • Comparatively easy and simple to manipulate the machine • Sensitivity such that many elements can be determined at ppm level or even less • High precision and	• Limited application as only about 70 elements excluding earth metals have been detected by this method. • Cannot yet detect non-metals	[66]

	accuracy obtained by the calibration curves • Absorption signal considerably free from inter-element interferences		
Inductively Coupled Plasma spectrometry (ICP)	• Very reliable, with overnight or unattended operation possible • Fast; it can scan the mass spectrum from 3 to 250 in just a few seconds • Capable of moving from mass to mass with a high degree of precision • It has high sensitivity, being able to detect trace quantities of many metals at levels well below part per billion (ppb)	• The inability to resolve target isotopes easily from molecular interferences • High background noise on the detector caused by the ion optics of the quadrupole mass analyzer, higher noise levels could result in degraded or reduced detection limits • Relatively slow analysis speed • Mass drift	[61,62]
Laser Induced Breakdown Spectroscopy (LIBS)	• Costs are low • Can analyze a large number of samples in a short span of time • All states of matter (solid, liquid, and gases) can be analyzed. Able to analyze extremely hard materials • Capable of doing multi-elemental analysis simultaneously • Minimal sample preparation is required which reduces worker exposure to hazardous radioactive or toxic substances • Requires small amount (μ gm) of sample	• Difficult to obtain suitable standards for LIBS analysis because of the matrix effect • Detection limits for solids are generally not good • Dissolved gases and bubbles produced by prior laser pulses can lead to the un-focusing of the laser beam • Due to these inherent problems, LIBS analysis of liquids has not been widely successful	[63]
X-ray Fluorescence	• Non-destructive analytical technique	• Analysis of relatively large spot of sample (typically >1g)	[64]

(XRF)	• Relatively simple spectra line void of many interferences • Speed and convenience of the procedure which permits multi-element analyses to be completed in a few minutes • High accuracy with precision.	• Difficulty in quantifying elements lighter than sodium • Difficulty in distinguishing variations among isotopes of an element or ions of the same elements in different valence state • Difficulty in achieving high sensitivity of weak peak when strong one is present and • High cost of instrument	
Neutron Activation Analysis (NAA)	• Excellent sensitivity and accuracy especially in respect of some trace elements • Multi-element character, i.e. it enables the simultaneous determination of many elements without chemical separation	• Number of suitable activation nuclear reactors is declining in many countries due to the shutdown of many research reactors, • Expensive equipment, • Analysis requires special laboratories and highly qualified personnel • Requiring handling	[67]
Ion Chromatography (IC)	• Applicable for the analysis of cations and anions, but mostly used for detecting anions, because there are better methods for the detection of cations • Provides accurate quantitative analyses	• Only ion concentrations can be determined • Complete salt phases are determined by deduction, which is only possible for simple systems	[65]

2.4 Types of heavy metal ion sensor

2.4.1 Optical sensors

The optical response of spherical gold nanoparticles (Au NPs) is well-known for exhibiting a single absorption band associated with the collective dipole oscillation known as

surface plasmon resonance. Due to their tunable optical and electronic properties, Au NPs are commonly used in sensors relying on this phenomenon. The color of Au NPs can vary from ruby red for smaller individual particles to purple or deep blue for larger particles or aggregates. In the case of sensor operation, the introduction of a specific analyte can induce uncontrolled aggregation of the Au NPs through binding, leading to a change in the solution color (surface plasmon resonance) [68]. This color change can be attributed to slight changes in the refractive index of the surrounding medium or alterations in the interactions between the NPs during the binding of targeted analytes.

Fluorescent sensors based on two-dimensional nanomaterials, such as graphene nanosheets, have gained significant attention for the detection of heavy metal ions. Graphene nanosheets offer excellent biocompatibility, chemical inertness, and lower cytotoxicity, making them a promising candidate for metal ion detection. For instance, Wu et al. reported the use of graphene oxide (GO) as a charge transfer-based fluorescent sensor for heavy metal ions [69].

2.4.2 Electrochemical sensors

Nanomaterial-based electrochemical sensors have been extensively employed for the rapid detection of heavy metal ions, complementing the capabilities of optical sensors. These sensors utilize the electrocatalytic activity of the working electrode within a redox system to detect the analyte, with selectivity determined by the oxidation peak location and sensitivity measured by the reaction current. The performance of electrochemical sensors relies heavily on the choice of electrode materials.

Nanomaterials have garnered significant attention as electrode materials in electrochemical sensors due to their small size, large accessible surface area, and high catalytic activity. Various nanomaterials, including nanoparticles, nanofibers, carbon nanotubes (CNTs), graphene, titanate nanosheets, and nanocomposites, have been extensively studied for heavy metal ion detection. These materials offer advantages such as high efficiency in pre-concentration and deposition of metal ions, as well as superior catalytic activity in stripping tests.

Graphene and its composites have demonstrated exceptional performance in electrochemical systems for heavy metal ion detection owing to their high conductivity and large specific surface area. For example, an electrochemical platform combining the high

adsorption capacity of γ-AlOOH with the conductivity of graphene was reported for the simultaneous detection of Cd^{2+} and Pb^{2+} ions using the square wave anodic stripping voltammetry (SWASV) technique [70].

The electrochemical method, such as anodic stripping voltammetry (ASV), stands out as a promising and elegant technique for the sensitive detection of trace levels of toxic heavy metal ions. This method offers advantages such as high sensitivity, selectivity, short detection time, and the capability to detect multiple heavy metals simultaneously [71].

2.4.3 Semiconductor-based heavy metal ion sensor

2.4.3.1 Metal oxides

Nanostructured metal oxides have excellent electron-transfer kinetics and possess strong adsorption capabilities on the surface of the working electrode, enabling them to detect a wide range of ions. Several metal oxides, including ZnO, CuO, Fe_3O_4, SnO_2, ZrO_2, TiO_2, MgO, and MnO_2, are commonly employed for heavy metal ion sensing due to their advantageous properties such as biocompatibility, low toxicity, and enhanced catalytic activity [71]. In a study conducted by Wei et al. [72], they achieved highly selective and sensitive detection of Pb^{2+} and Cd^{2+} ions by creating adsorptive porous magnesium oxide (MgO) nanoflowers. By employing stripping voltammetry analysis, they were able to detect Pb^{2+} ions with a detection limit of 2.1 pM and Cd^{2+} ions with a detection limit of 81 pM. Another recent report by Buica et al. [73] demonstrated an integrated sensing system for the detection of heavy metals such as Cd^{2+}, Pb^{2+}, Hg^{2+}, and Cu^{2+}. They utilized Zr/ZrO_2-based electrodes and observed enhanced sensitivity rates under UV irradiation. Similarly, Yantasee et al. [74] presented a straightforward method for detecting Pb^{2+} ions in urine using dimercaptosuccinic acid (DMSA) functionalized superparamagnetic Fe_3O_4 nanoparticles. This sensor also exhibited the ability to detect other heavy metals like Cd, Pb, Cu, and Ag in natural waters at concentrations below 1 ppb. Gao et al. developed a rapid and direct electrochemical detection method for Arsenic (As) in drinking water, without the need for noble metals [75]. Xie et al. synthesized a graphene-decorated CeO2 nanocomposite using a hydrothermal approach, demonstrating excellent electrochemical detection of heavy metal ions in aqueous solutions [76]. Zhou et al. reported improved electrochemical sensing performance for heavy metal ions using l-cysteine functionalized $MnFe_2O_4$ mesoporous nanospheres as electrochemical sensors, enabling the identification of Pb^{2+}, Cu^{2+}, Hg^{2+}, and

Cd^{2+} in aqueous solutions [77]. Wu et al. prepared NiO nanosheets through calcination, achieving promising results for the detection of Hg^{2+} ions, even at low concentrations [78].

2.4.3.2 Transition metal dichalcogenides

Transition Metal Dichalcogenides (TMDCs) are a group of two-dimensional layered materials known for their unique structural properties and diverse range of applications, including energy storage, thermal management, optoelectronics, catalysis, superconductivity, heavy metal ion detection, and gas sensing [79-82]. These materials are composed of hexagonal layers of metal atoms (M), which can be any transition metal element from groups IV-VII B (such as Mo, W, V, Nb, Ta, Ti, Zr, Hf, and Re), sandwiched between two layers of chalcogen atoms (X) like S, Se, or Te, resulting in a three-layer atomic structure [83]. One of the remarkable features of TMDCs is their tunable bandgap, which plays a crucial role in determining their specific applications. TMDCs exhibit a high surface-to-volume ratio, providing a larger number of active sites on their surfaces for enhanced adsorption capacity, making them suitable for addressing environmental pollution challenges [84]. Various synthesis methods, including mechanical exfoliation, chemical vapor deposition, flux growth, hydrothermal synthesis, and physical evaporation, can be employed to fabricate TMDCs [85]. Rahman et al. achieved the successful synthesis of 1T-WS2 microflowers using a straightforward hydrothermal method. These micro flowers demonstrated improved sensitivity for detecting ultra-trace levels of Hg^{2+} ions in aqueous solutions, offering high accuracy and reliability. The measured detection limit for Hg^{2+} was approximately 79.8 pM, surpassing the standard permissible limits recommended for drinking water [86]. Yin et al. (2017) demonstrated the selective detection of Cd^{2+} ions using a self-assembled nanocomposite called MoS_2/TMPyP. The nanocomposite exhibited high sensitivity, allowing for the detection of Cd^{2+} ions at lower limits of up to 7.2×10^{-8} mol/L [87]. Li et al. achieved the successful synthesis of flower-like microspheres of WS_2 and WSe_2 using facile and high-yield solvothermal methods. These microspheres exhibited remarkable detection capability for Pb^{2+} and Hg^{2+}, highlighting their significant potential for detecting heavy metals even at traceable limits [88].

The advantages and disadvantages of different sensor types are listed in Table 2.4

Table 2.4: Advantages and disadvantages of different sensor

Sensor type	Advantages	Disadvantages	References
Optical sensor	• Simple • High sensitivity • High selectivity	• Requires optical instruments and light sources • Interference from other substances or light source	[89,90]
Electrochemical sensor	• Fast and distinctive responses to different metal ions • Suitable for simultaneous detection of multiple metal ions. • Low cost • Easy operation	• Requires electrode materials and modifications. • Interference from other electroactive species • Limited stability • Reproducibility	[91,92]
Semiconducting sensor	• High sensitivity • Selectivity • Compatible with microfabrication and integration.	• Limited to specific metal ions • Susceptibility to environmental factors	[89,90]

2.5 Fabrication of sensing layer

The sensing layer plays a crucial role in the fabrication of effective heavy metal sensors. In recent times, nanostructured materials have gained significant attention as sensing layers due to their remarkable adsorption and catalytic properties. The synthesis techniques for nanostructured materials can be categorized into two divisions: (i) top-down approaches and (ii) bottom-up approaches. These methods offer diverse approaches to create nanostructured materials with desirable properties for sensing applications.

2.5.1 Top-down approaches

Top-down approaches involve the fragmentation or division of bulk materials to obtain nanostructured materials. Various methods fall under the category of top-down approaches, including mechanical milling, laser ablation, etching, sputtering, and electro-

explosion. These techniques enable the transformation of bulk materials into nanostructured forms through controlled processes.

2.5.1.1 Mechanical milling

Mechanical milling is an economically viable technique employed to create nanoscale materials from bulk materials. It offers a cost-effective approach for producing blends of different phases and is particularly useful in the production of nanocomposites. The process of mechanical milling, as illustrated in Figure 2.1, involves the use of ball milling to achieve desired results [93]. This method finds application in the synthesis of various materials, including oxide and carbide-strengthened aluminum alloys, wear-resistant spray coatings, aluminum/nickel/magnesium/copper-based nanoalloys, and a range of nanocomposite materials [94]

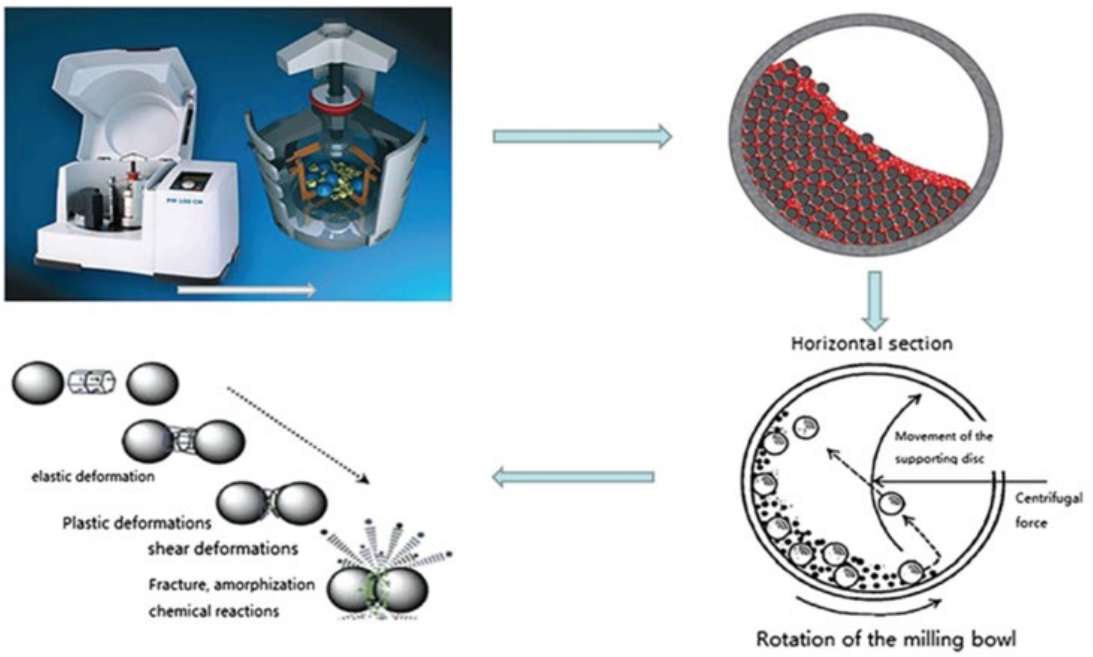

Figure 2.1: The process of ball milling method (adopted from [93])

2.5.1.2 Electrospinning

Electrospinning is a straightforward top-down method widely employed for the fabrication of nanostructured materials, particularly nanofibers. It is commonly utilized for generating nanofibers from diverse materials, with polymers being the predominant choice [95]. A significant advancement in electrospinning is coaxial electrospinning, wherein the spinneret consists of two coaxial capillaries. This configuration allows for the use of two viscous liquids or a viscous liquid as the shell and a non-viscous liquid as the core to form core-shell nano architectures under an electric field. Coaxial electrospinning is a simple and effective technique for producing large-scale core-shell ultrathin fibers, with lengths extending up to several centimeters. This approach has facilitated the development of various core-shell and hollow polymer, inorganic, organic, and hybrid materials [96]. A schematic diagram illustrating the coaxial electrospinning process is presented in Figure 2.2 [97].

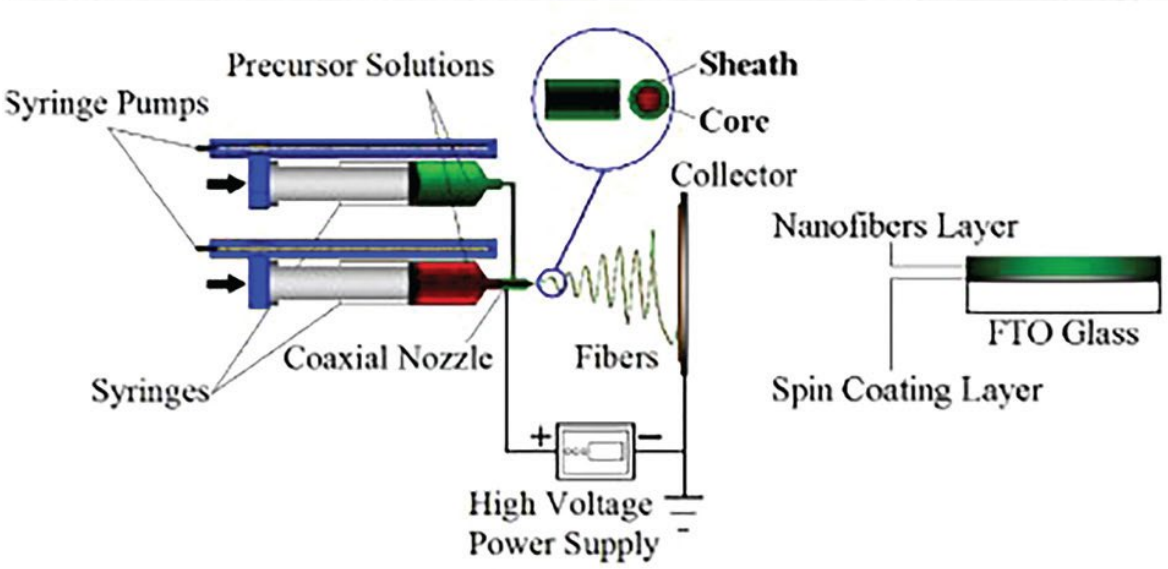

Figure 2.2: A schematic diagram of the electrospinning technique (adopted from [97])

2.5.1.3 Lithography

Lithography serves as a valuable tool for the fabrication of nanoarchitectures, involving the utilization of a focused beam of light or electrons. It can be categorized into two primary types: masked lithography and maskless lithography [98]. Masked lithography involves the transfer of nanopatterns across a large surface area using a specific mask or template. Examples of masked lithography techniques include photolithography [99], nanoimprint lithography [100], and soft lithography [101]. On the other hand, maskless

lithography encompasses scanning probe lithography [102], focused ion beam lithography [103], and electron beam lithography, where nanopattern writing can be carried out without

the involvement of a mask. Furthermore, by combining focused ion beam with wet chemical etching, 3D freeform micro-nano-fabrication can be achieved through ion implantation, as depicted in Figure 2.3 [104].

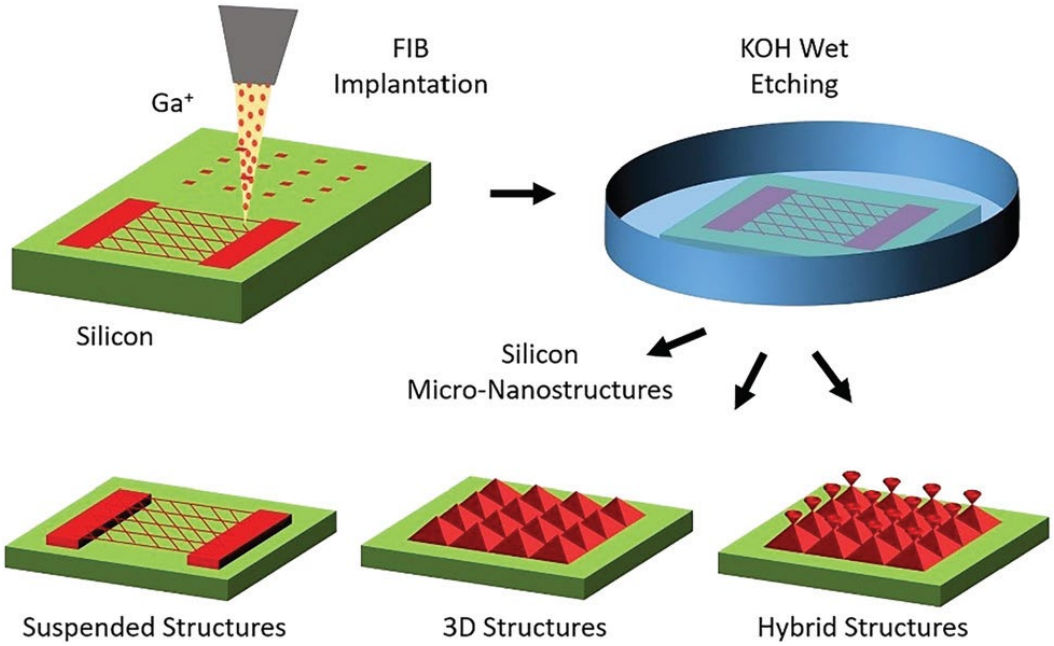

Figure 2.3: A schematic diagram of the fabrication of 3D micro-nanostructures with an ion beam through bulk Si structuring (adopted from [104])

2.5.1.4 Sputtering

Sputtering is a process that involves bombarding solid surfaces with high-energy particles, such as plasma or gas, to produce nanomaterials. It is widely recognized as the cathode target, and free electrons collide with the gas to produce gas ions. These positively charged ions accelerate towards the cathode target under the influence of the electric field, with the target surface and causing atoms to be ejected from the surface [108]. For instance, magnetron sputtering is employed to produce WSe_2-layered nanofilms on substrates such as SiO_2 and carbon paper [109]. The sputtering technique is notable because the composition of

the sputtered nanomaterial remains consistent with the target material, the impurities. It is a cost-effective alternative to electron-beam lithography.

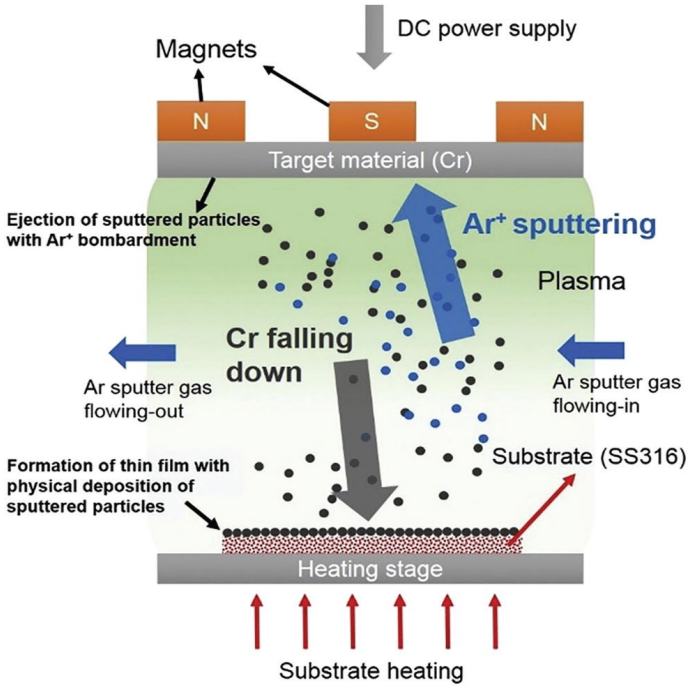

Figure 2.4: A schematic diagram of the DC magnetron sputtering (adopted from [106])

2.5.1.5 Laser ablation

Laser ablation synthesis is a method used to generate nanoparticles by directing a powerful laser beam at a target material. During the process, the target material or precursor is vaporized due to the high energy of the laser irradiation, leading to the formation of nanoparticles. The process is shown in Figure 2.5. One notable advantage of laser ablation is its eco-friendly nature, as it eliminates the need for stabilizing agents or additional chemicals [110]. This technique offers a wide range of possibilities for producing various nanomaterials, including metal nanoparticles [111], carbon nanomaterials [112,113], oxide composites [114], and ceramics [115]. Pulsed laser ablation in liquids is an especially intriguing approach for producing uniform colloidal nanoparticle solutions without the use of surfactants or ligands.

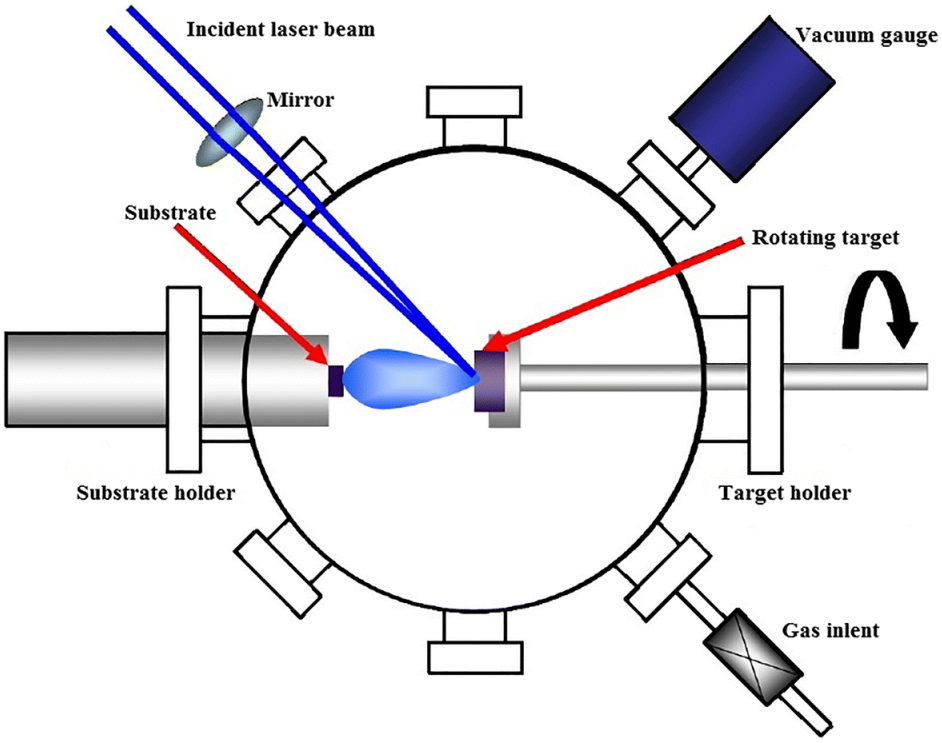

Figure 2.5: Schematic diagram of laser ablation method (adopted from [116])

2.5.2 Bottom-up approaches

2.5.2.1 Chemical vapor deposition (CVD)

Chemical vapor deposition (CVD) methods hold immense importance in the production of carbon-based nanomaterials. In the CVD process, vapor-phase precursors undergo a chemical reaction to form a thin film on the surface of a substrate. A precursor is deemed suitable for CVD if it possesses desirable characteristics such as adequate volatility, high chemical purity, stability during evaporation, low cost, non-hazardous nature, and long shelf-life. The entire schematic is shown in Figure 2.6. It is also crucial that its decomposition does not result in residual impurities [117]. For instance, in the synthesis of carbon nanotubes using CVD, a substrate is placed in an oven and subjected to high temperatures. Subsequently, a carbon-containing gas, such as hydrocarbons, is slowly introduced into the system as a precursor. At elevated temperatures, the gas decomposes, releasing carbon atoms that subsequently recombine to form carbon nanotubes on the substrate [118]. It should be noted that the choice of catalyst significantly influences the morphology and type of nanomaterial obtained.

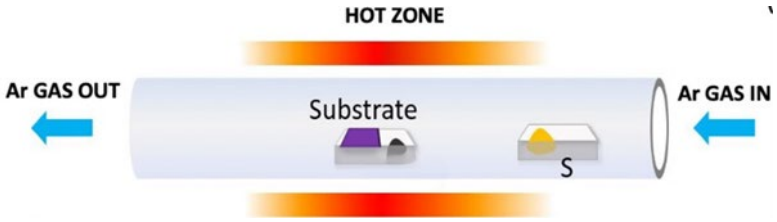

Figure 2.6: Schematic diagram of Chemical Vapor Deposition (adopted from [134])

2.5.2.2 Solvothermal and hydrothermal methods

The hydrothermal process is widely known and extensively employed for the synthesis of nanostructured materials [120,121]. It involves a heterogeneous reaction conducted in an aqueous environment under high pressure and temperature near the critical point within a sealed container [122]. Similarly, the solvothermal method shares similarities with the hydrothermal method but is performed in a non-aqueous medium. The schematic of the hydrothermal method is shown in Figure 2.7. Both hydrothermal and solvothermal approaches are typically carried out in enclosed systems [123]. Recently, the microwave-assisted hydrothermal method has gained considerable attention for the fabrication of nanomaterials by combining the benefits of hydrothermal and microwave techniques [124]. Hydrothermal and solvothermal methods offer promising avenues for producing various nanostructures such as nanowires, nanorods, nanosheets, and nanospheres [125–127]. These methods present exciting opportunities for engineering materials with desired nano-geometries.

Figure 2.7: Schematic diagram of the hydrothermal synthesis (adopted from [128])

2.5.2.3 Sol-gel method

The sol-gel method is a widely employed wet chemical technique for the synthesis of nanomaterials, particularly high-quality metal-oxide-based materials. This method derives its name from the transformation of a liquid precursor into a sol, which subsequently undergoes gelation to form a network structure [129]. Metal alkoxides are commonly used as conventional precursors for nanomaterial synthesis via the sol-gel method. The synthesis process involves several steps. Initially, hydrolysis of the metal oxide precursor occurs in water or with the assistance of alcohol, leading to the formation of a sol. Subsequently, condensation takes place, resulting in an increase in solvent viscosity and the formation of porous structures. These structures undergo aging, during which polycondensation reactions occur, leading to the formation of metal-hydroxo or metal-oxo-polymers in solution [130]. During the aging process, further polycondensation occurs, causing changes in the structure, properties, and porosity of the material. The porosity decreases, while the distance between colloidal particles increases. After aging, the gel is subjected to drying to remove water and organic solvents, followed by calcination to obtain nanoparticles [131]. Figure 2.8 illustrates the formation of films and powders using the sol-gel method [132]. The final product obtained through the sol-gel method is influenced by factors such as the precursor nature, hydrolysis rate, aging time, pH, and the molar ratio between water and the precursor [133].

The sol-gel method offers several advantages, including its eco-friendly nature, homogeneity of the produced material, low processing temperature, and its ability to facilitate the production of composites and complex nanostructures. It is a cost-effective and straightforward approach for synthesizing a wide range of nanomaterials [131].

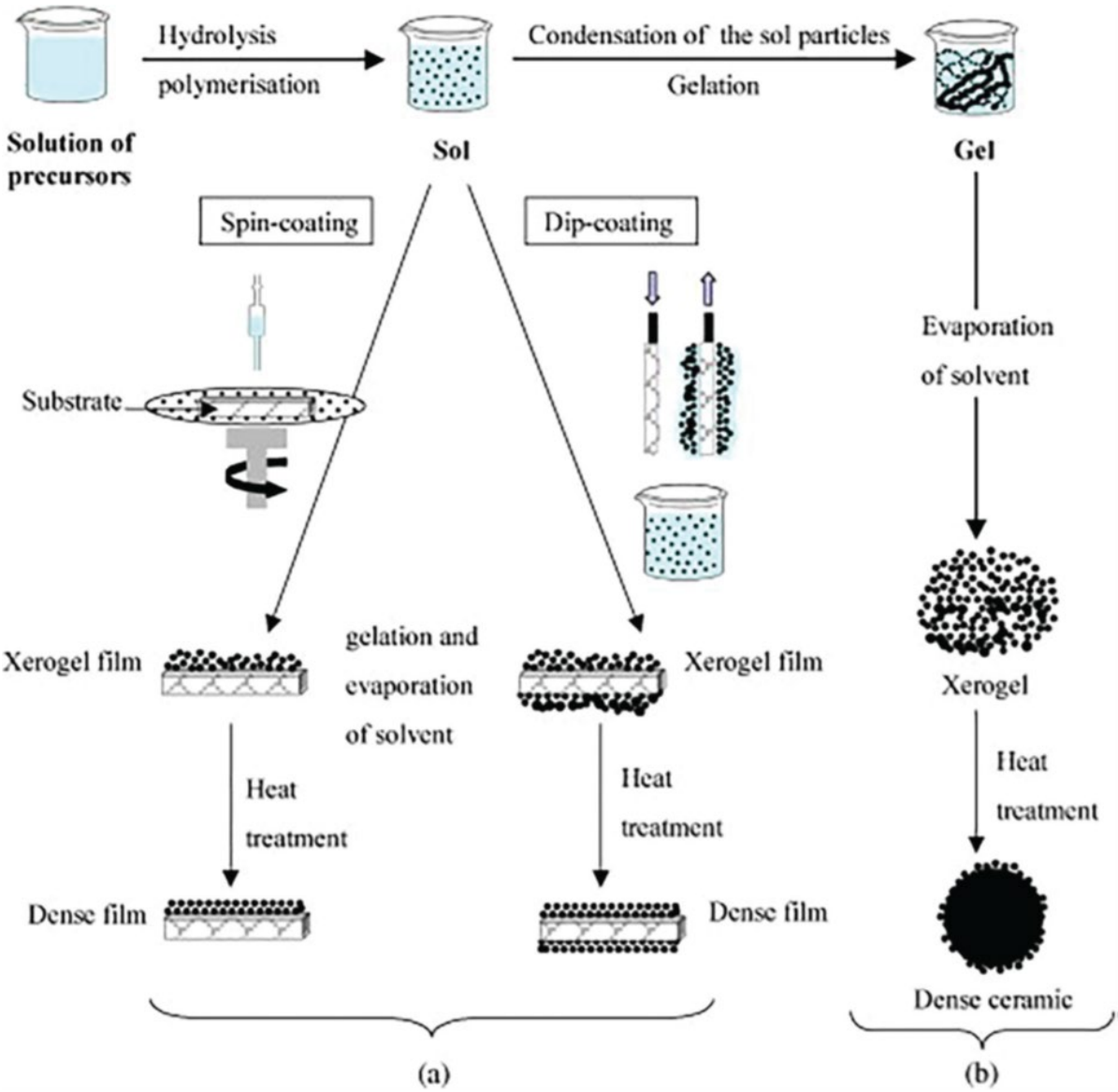

Figure 2.8: An overview showing two sol–gel method synthesis examples: (a) films from a colloidal sol and (b) powder from a colloidal sol transformed into a gel (adopted from [132])

References

[1] O. Pourret, J.-C. Bollinger, and A. Hursthouse, "Heavy metal: a misused term?," Acta Geochimica, vol. 40, pp. 466-471, 2021.

[2] J. H. Duffus, "" Heavy metals" a meaningless term?(IUPAC Technical Report)," Pure and applied chemistry, vol. 74, no. 5, pp. 793-807, 2002.

[3] F. Habashi, "Gmelin and his Handbuch," Bulletin for the History of Chemistry, vol. 34, no. 2, p. 30, 2009.

[4] G. Aragay, J. Pons, and A. Merkoçi, "Recent trends in macro-, micro-, and nanomaterial-based tools and strategies for heavy-metal detection," Chemical reviews, vol. 111, no. 5, pp. 3433-3458, 2011.

[5] N. P. Raval, P. U. Shah, and N. K. Shah, "Adsorptive removal of nickel (II) ions from aqueous environment: A review," Journal of Environmental Management, vol. 179, pp. 1-20, 2016.

[6] P. B. Tchounwou, C. Yedjou, A. Patlolla, D. Sutton, and A. Luch, "Molecular, clinical and environmental toxicology," Molecular, Clinical and Environmental Toxicology, vol. 3, pp. 133-164, 2012.

[7] G. WHO, "Guidelines for drinking-water quality," World health organization, vol. 216, pp. 303-304, 2011.

[8] H. Bradl, "Heavy metals interaction in the environment; origin, interactions, and remediation," ed: London Academic Press (6), 2002.

[9] Z. L. He, X. E. Yang, and P. J. Stoffella, "Trace elements in agroecosystems and impacts on the environment," Journal of Trace elements in Medicine and Biology, vol. 19, no. 2-3, pp. 125-140, 2005.

[10] J. E. Fergusson and F. P. Prucha, The heavy elements: chemistry, environmental impact and health effects. Pergamon press Oxford, 1990.

[11] M. B. Gumpu, S. Sethuraman, U. M. Krishnan, and J. B. B. Rayappan, "A review on detection of heavy metal ions in water–an electrochemical approach," Sensors and actuators B: chemical, vol. 213, pp. 515-533, 2015.

[12] G. Zhou et al., "Ultrasensitive mercury ion detection using DNA-functionalized molybdenum disulfide nanosheet/gold nanoparticle hybrid field-effect transistor device," Acs Sensors, vol. 1, no. 3, pp. 295-302, 2016.

[13] O. Synhaivska et al., "Detection of Cu^{2+} ions with GGH peptide realized with Si-nanoribbon ISFET," Sensors, vol. 19, no. 18, p. 4022, 2019.

[14] B. Dhir, P. Sharmila, and P. P. Saradhi, "Potential of aquatic macrophytes for removing contaminants from the environment," Critical Reviews in Environmental Science and Technology, vol. 39, no. 9, pp. 754-781, 2009.

[15] S. Yang, J. Li, D. Shao, J. Hu, and X. Wang, "Adsorption of Ni (II) on oxidized multi-walled carbon nanotubes: effect of contact time, pH, foreign ions and PAA," Journal of hazardous materials, vol. 166, no. 1, pp. 109-116, 2009.

[16] A. Nigam, V. S. Bhati, T. N. Bhat, S. B. Dolmanan, S. Tripathy, and M. Kumar, "Sensitive and selective detection of Pb^{2+} ions using 2, 5-dimercapto-1, 3, 4-thiadiazole functionalized AlGaN/GaN high electron mobility transistor," IEEE Electron Device Letters, vol. 40, no. 12, pp. 1976-1979, 2019.

[17] G. WHO, "Hardness in Drinking-water: background document for development of WHO guidelines for drinking-water quality," ed: World Health Organization Geneva, 2011.

[18] C. W. Commission, "Status of trace and toxic metals in Indian Rivers," Ministry of Jal Shakti, Department of Water Resources, River Development, and Ganga Rejuvenation: New Delhi, India, 2019.

[19] Y.-T. Chen et al., "High-field modulated ion-selective field-effect-transistor (FET) sensors with sensitivity higher than the ideal Nernst sensitivity," Scientific reports, vol. 8, no. 1, p. 8300, 2018.

[20] C. F. Carolin, P. S. Kumar, A. Saravanan, G. J. Joshiba, and M. Naushad, "Efficient techniques for the removal of toxic heavy metals from aquatic environment: A review," Journal of environmental chemical engineering, vol. 5, no. 3, pp. 2782-2799, 2017.

[21] Shaily, A. Kumar, I. Parveen, and N. Ahmed, "Highly selective and sensitive coumarin–triazole-based fluorometric 'turn-off'sensor for detection of Pb2+ ions," Luminescence, vol. 33, no. 4, pp. 713-721, 2018.

[22] C. B. Swearingen, D. P. Wernette, D. M. Cropek, Y. Lu, J. V. Sweedler, and P. W. Bohn, "Immobilization of a catalytic DNA molecular beacon on Au for Pb (II) detection," Analytical chemistry, vol. 77, no. 2, pp. 442-448, 2005.

[23] B. Bansod, T. Kumar, R. Thakur, S. Rana, and I. Singh, "A review on various electrochemical techniques for heavy metal ions detection with different sensing platforms," Biosensors and Bioelectronics, vol. 94, pp. 443-455, 2017.

[24] C. Ariño, N. Serrano, J. M. Díaz-Cruz, and M. Esteban, "Voltammetric determination of metal ions beyond mercury electrodes. A review," Analytica chimica acta, vol. 990, pp. 11-53, 2017.

[25] G. WHO, "Hardness in Drinking-water: background document for development of WHO guidelines for drinking-water quality," ed: World Health Organization Geneva, 2011.

[26] C. J. Wyatt, C. Fimbres, L. Romo, R. Mendez, and M. Grijalva, "Incidence of heavy metal contamination in water supplies in Northern Mexico," Environmental research, vol. 76, no. 2, pp. 114-119, 1998.

[27] T. W. Clarkson, L. Magos, and G. J. Myers, "The toxicology of mercury—current exposures and clinical manifestations," New England Journal of Medicine, vol. 349, no. 18, pp. 1731-1737, 2003.

[28] A. Bhan and N. Sarkar, "Mercury in the environment: effect on health and reproduction," Reviews on environmental health, vol. 20, no. 1, pp. 39-56, 2005.

[29] B. Gworek, O. Bemowska-Kałabun, M. Kijeńska, and J. Wrzosek-Jakubowska, "Mercury in marine and oceanic waters—a review," Water, Air, & Soil Pollution, vol. 227, no. 10, p. 371, 2016.

[30] C. Sanfeliu, J. Sebastià, R. Cristòfol, and E. Rodríguez-Farré, "Neurotoxicity of organomercurial compounds," Neurotoxicity research, vol. 5, pp. 283-305, 2003.

[31] S. Satarug et al., "A global perspective on cadmium pollution and toxicity in non-occupationally exposed population," Toxicology letters, vol. 137, no. 1-2, pp. 65-83, 2003.

[32] S. Demim, N. Drouiche, A. Aouabed, T. Benayad, O. Dendene-Badache, and S. Semsari, "Cadmium and nickel: Assessment of the physiological effects and heavy metal removal using a response surface approach by L. gibba," Ecological Engineering, vol. 61, pp. 426-435, 2013.

[33] M. Filipič, "Mechanisms of cadmium induced genomic instability," Mutation Research/Fundamental and Molecular Mechanisms of Mutagenesis, vol. 733, no. 1-2, pp. 69-77, 2012.

[34] T. Inaba et al., "Estimation of cumulative cadmium intake causing Itai–itai disease," Toxicology letters, vol. 159, no. 2, pp. 192-201, 2005.

[35] F. Yoshida, A. Hata, and H. Tonegawa, "Itai-Itai disease and the countermeasures against cadmium pollution by the Kamioka mine," Environmental Economics and Policy Studies, vol. 2, pp. 215-229, 1999.

[36] Y. Guo, Y. Zhang, H. Shao, Z. Wang, X. Wang, and X. Jiang, "Label-free colorimetric detection of cadmium ions in rice samples using gold nanoparticles," Analytical chemistry, vol. 86, no. 17, pp. 8530-8534, 2014.

[37] Y.-S. Hong, K.-H. Song, and J.-Y. Chung, "Health effects of chronic arsenic exposure," Journal of preventive medicine and public health, vol. 47, no. 5, p. 245, 2014.

[38] J.-H. Lu, H.-S. Yu, and C.-H. Lee, "Arsenic skin carcinogenesis: A prototypic model of chemical carcinogenesis featured with abnormal differentiation and aberrant immune responses," Essential and Toxic Trace Elements and Vitamins in Human Health, pp. 165-170, 2020.

[39] I. Palma-Lara et al., "Arsenic exposure: A public health problem leading to several cancers," Regulatory Toxicology and Pharmacology, vol. 110, p. 104539, 2020.

[40] S. Bhardwaj, R. Soni, S. K. Gupta, and D. P. Shukla, "Mercury, arsenic, lead and cadmium in waters of the Singrauli coal mining and power plants industrial zone, Central East India," Environmental monitoring and assessment, vol. 192, pp. 1-20, 2020.

[41] Z. Li, Q. Yang, Y. Yang, C. Xie, and H. Ma, "Hydrogeochemical controls on arsenic contamination potential and health threat in an intensive agricultural area, northern China," Environmental Pollution, vol. 256, p. 113455, 2020.

[42] I. Mihajlov et al., "Arsenic contamination of Bangladesh aquifers exacerbated by clay layers," Nature communications, vol. 11, no. 1, p. 2244, 2020.

[43] S. Sheikhi, Z. Faraji, and H. Aslani, "Arsenic health risk assessment and the evaluation of groundwater quality using GWQI and multivariate statistical analysis in rural areas, Hashtroud, Iran," Environmental Science and Pollution Research, vol. 28, pp. 3617-3631, 2021.

[44] M. C. Teixeira, A. C. Santos, C. S. Fernandes, and J. C. Ng, "Arsenic contamination assessment in Brazil–Past, present and future concerns: A historical and critical review," Science of the total environment, vol. 730, p. 138217, 2020.

[45] D. Chakraborti et al., "Status of groundwater arsenic contamination in Bangladesh: a 14-year study report," Water research, vol. 44, no. 19, pp. 5789-5802, 2010.

[46] M. M. Karim, "Arsenic in groundwater and health problems in Bangladesh," Water Research, vol. 34, no. 1, pp. 304-310, 2000.

[47] N. H. Khdary and A. E. Gassim, "The distribution and accretion of some heavy metals in Makkah Wells," Journal of Water Resource and Protection, vol. 2014, 2014.

[48] A. K. Krishna, M. Satyanarayanan, and P. K. Govil, "Assessment of heavy metal pollution in water using multivariate statistical techniques in an industrial area: a case study from Patancheru, Medak District, Andhra Pradesh, India," Journal of hazardous materials, vol. 167, no. 1-3, pp. 366-373, 2009.

[49] J. Buschmann et al., "Contamination of drinking water resources in the Mekong delta floodplains: Arsenic and other trace metals pose serious health risks to population," Environment international, vol. 34, no. 6, pp. 756-764, 2008.

[50] E. L. Que, D. W. Domaille, and C. J. Chang, "Metals in neurobiology: probing their chemistry and biology with molecular imaging," Chemical reviews, vol. 108, no. 5, pp. 1517-1549, 2008.

[51] M. R. Awual, M. Ismael, M. A. Khaleque, and T. Yaita, "Ultra-trace copper (II) detection and removal from wastewater using novel meso-adsorbent," Journal of Industrial and Engineering Chemistry, vol. 20, no. 4, pp. 2332-2340, 2014.

[52] B. R. Stern, "Essentiality and toxicity in copper health risk assessment: overview, update and regulatory considerations," Journal of Toxicology and Environmental Health, Part A, vol. 73, no. 2-3, pp. 114-127, 2010.

[53] D. Mehta, S. Mazumdar, and S. Singh, "Magnetic adsorbents for the treatment of water/wastewater—a review," Journal of Water Process Engineering, vol. 7, pp. 244-265, 2015.

[54] M. R. Awual, T. Yaita, S. A. El-Safty, H. Shiwaku, S. Suzuki, and Y. Okamoto, "Copper (II) ions capturing from water using ligand modified a new type mesoporous adsorbent," Chemical Engineering Journal, vol. 221, pp. 322-330, 2013.

[55] J. A. Jacobs and S. M. Testa, "Overview of chromium (VI) in the environment: background and history," Chromium (VI) handbook, pp. 1-21, 2005.

[56] V. Velma, S. Vutukuru, and P. B. Tchounwou, "Ecotoxicology of hexavalent chromium in freshwater fish: a critical review," Reviews on environmental health, vol. 24, no. 2, pp. 129-146, 2009.

[57] J. A. Jacobs and S. M. Testa, "Overview of chromium (VI) in the environment: background and history," Chromium (VI) handbook, pp. 1-21, 2005.

[58] T. Davidson et al., "Exposure to chromium (VI) in the drinking water increases susceptibility to UV-induced skin tumors in hairless mice," Toxicology and applied pharmacology, vol. 196, no. 3, pp. 431-437, 2004.

[59] D. Paustenbach, B. Finley, F. Mowat, and B. Kerger, "Human health risk and exposure assessment of chromium (VI) in tap water," Journal of Toxicology and Environmental Health, Part A, vol. 66, no. 14, pp. 1295-1339, 2003.

[60] R. Mohamed, A. Abdel-Lateef, H. Mahmoud, and A. Helal, "Determination of trace elements in water and sediment samples from Ismaelia Canal using ion chromatography and atomic absorption spectroscopy," Chemical Speciation & Bioavailability, vol. 24, no. 1, pp. 31-38, 2012.

[61] L. Eddaif, A. Shaban, J. Telegdi, and I. Szendro, "A piezogravimetric sensor platform for sensitive detection of lead (ii) ions in water based on calix [4] resorcinarene macrocycles: synthesis, characterization and detection," Arabian Journal of Chemistry, vol. 13, no. 2, pp. 4448-4461, 2020.

[62] M. Batsala, B. Chandu, B. Sakala, S. Nama, and S. Domatoti, "Inductively coupled plasma mass spectrometry (ICP-MS)," Int J Res Pharm Chem, vol. 2, no. 3, pp. 671-680, 2012.

[63] F. Zhao, Z. Chen, F. Zhang, R. Li, and J. Zhou, "Ultra-sensitive detection of heavy metal ions in tap water by laser-induced breakdown spectroscopy with the assistance of electrical-deposition," Analytical Methods, vol. 2, no. 4, pp. 408-414, 2010.

[64] L. Borgese, A. Zacco, E. Bontempi, M. Pellegatta, L. Vigna, and L. Patrini, "L. Riboldi, Rubino FM, Depero LE Use of total reflection X-ray fluorescence (TXRF) for the evaluation of heavy metal poisoning due to the improper use of a traditional ayurvedic drug," J. Pharm. Biomed. Anal, vol. 52, pp. 787-790, 2010.

[65] C. Sarzanini and M. C. Bruzzoniti, "Metal species determination by ion chromatography," TrAC Trends in Analytical Chemistry, vol. 20, no. 6-7, pp. 304-310, 2001.

[66] R. Mohamed, A. Abdel-Lateef, H. Mahmoud, and A. Helal, "Determination of trace elements in water and sediment samples from Ismaelia Canal using ion chromatography and atomic absorption spectroscopy," Chemical Speciation & Bioavailability, vol. 24, no. 1, pp. 31-38, 2012.

[67] V. Guinn and C. Wagner, "Instrumental neutron activation analysis," Analytical Chemistry, vol. 32, no. 3, pp. 317-323, 1960.

[68] Y. Yang, S. Matsubara, M. Nogami, J. Shi, and W. Huang, "One-dimensional self-assembly of gold nanoparticles for tunable surface plasmon resonance properties," Nanotechnology, vol. 17, no. 11, p. 2821, 2006.

[69] M. Li, X. Zhou, W. Ding, S. Guo, and N. Wu, "Fluorescent aptamer-functionalized graphene oxide biosensor for label-free detection of mercury (II)," Biosensors and Bioelectronics, vol. 41, pp. 889-893, 2013.

[70] C. Gao, X.-Y. Yu, R.-X. Xu, J.-H. Liu, and X.-J. Huang, "AlOOH-reduced graphene oxide nanocomposites: one-pot hydrothermal synthesis and their enhanced electrochemical activity for heavy metal ions," ACS applied materials & interfaces, vol. 4, no. 9, pp. 4672-4682, 2012.

[71] A. Economou and P. Fielden, "Mercury film electrodes: developments, trends and potentialities for electroanalysis," Analyst, vol. 128, no. 3, pp. 205-213, 2003.

[72] Y. Wei, R. Yang, X.-Y. Yu, L. Wang, J.-H. Liu, and X.-J. Huang, "Stripping voltammetry study of ultra-trace toxic metal ions on highly selectively adsorptive porous magnesium oxide nanoflowers," Analyst, vol. 137, no. 9, pp. 2183-2191, 2012.

[73] G.-O. Buica, A. B. Stoian, C. Manole, I. Demetrescu, and C. Pirvu, "Zr/ZrO_2 nanotube electrode for detection of heavy metal ions," Electrochemistry Communications, vol. 110, p. 106614, 2020.

[74] W. Yantasee et al., "Direct detection of Pb in urine and Cd, Pb, Cu, and Ag in natural waters using electrochemical sensors immobilized with DMSA functionalized magnetic nanoparticles," Analyst, vol. 133, no. 3, pp. 348-355, 2008.

[75] C. Gao, X.-Y. Yu, S.-Q. Xiong, J.-H. Liu, and X.-J. Huang, "Electrochemical detection of arsenic (III) completely free from noble metal: Fe3O4 microspheres-room temperature ionic liquid composite showing better performance than gold," Analytical chemistry, vol. 85, no. 5, pp. 2673-2680, 2013.

[76] Y.-L. Xie, S.-Q. Zhao, H.-L. Ye, J. Yuan, P. Song, and S.-Q. Hu, "Graphene/CeO2 hybrid materials for the simultaneous electrochemical detection of cadmium (II), lead (II), copper (II), and mercury (II)," Journal of Electroanalytical Chemistry, vol. 757, pp. 235-242, 2015.

[77] S.-F. Zhou et al., "Individual and simultaneous electrochemical detection toward heavy metal ions based on L-cysteine modified mesoporous $MnFe_2O_4$ nanocrystal clusters," Journal of Alloys and Compounds, vol. 721, pp. 492-500, 2017.

[78] Z. Wu, L. Jiang, Y. Zhu, C. Xu, Y. Ye, and X. Wang, "Synthesis of mesoporous NiO nanosheet and its application on mercury (II) sensor," Journal of Solid State Electrochemistry, vol. 16, pp. 3171-3177, 2012.

[79] Y.-P. Gao, X. Wu, K.-J. Huang, L.-L. Xing, Y.-Y. Zhang, and L. Liu, "Two-dimensional transition metal diseleniums for energy storage application: a review of recent developments," CrystEngComm, vol. 19, no. 3, pp. 404-418, 2017.

[80] J. Lu et al., "Evidence for two-dimensional Ising superconductivity in gated MoS_2," Science, vol. 350, no. 6266, pp. 1353-1357, 2015.

[81] R. Kumar, N. Goel, and M. Kumar, "UV-activated MoS_2 based fast and reversible NO_2 sensor at room temperature," ACS sensors, vol. 2, no. 11, pp. 1744-1752, 2017.

[82] A. Nigam et al., "Real time detection of Hg^{2+} ions using MoS_2 functionalized AlGaN/GaN high electron mobility transistor for water quality monitoring," Sensors and Actuators B: Chemical, vol. 309, p. 127832, 2020.

[83] R. Kappera et al., "Phase-engineered low-resistance contacts for ultrathin MoS_2 transistors," Nature materials, vol. 13, no. 12, pp. 1128-1134, 2014.

[84] X. Zhang, S. Y. Teng, A. C. M. Loy, B. S. How, W. D. Leong, and X. Tao, "Transition metal dichalcogenides for the application of pollution reduction: A review," Nanomaterials, vol. 10, no. 6, p. 1012, 2020.

[85] H. Wang, C. Li, P. Fang, Z. Zhang, and J. Z. Zhang, "Synthesis, properties, and optoelectronic applications of two-dimensional MoS_2 and MoS_2-based heterostructures," Chemical Society Reviews, vol. 47, no. 16, pp. 6101-6127, 2018.

[86] M. T. Rahman et al., "Metallic 1T phase tungsten disulfide microflowers for trace level detection of Hg^{2+} ions," Advanced Sustainable Systems, vol. 4, no. 9, p. 2000068, 2020.

[87] W. Yin et al., "MoS_2-nanosheet-assisted coordination of metal ions with porphyrin for rapid detection and removal of cadmium ions in aqueous media," ACS Applied Materials & Interfaces, vol. 9, no. 25, pp. 21362-21370, 2017.

[88] S. M. Rosolina, S. A. Bragg, R. Ouyang, J. Q. Chambers, and Z.-L. Xue, "Highly sensitive detection of hexavalent chromium utilizing a sol-gel/carbon nanotube modified electrode," Journal of Electroanalytical Chemistry, vol. 781, pp. 120-125, 2016.

[89] A. Nigam, N. Sharma, S. Tripathy, and M. Kumar, "Development of semiconductor based heavy metal ion sensors for water analysis: A review," Sensors and Actuators A: Physical, vol. 330, p. 112879, 2021.

[90] X. Xu, S. Yang, Y. Wang, and K. Qian, "Nanomaterial-based sensors and strategies for heavy metal ion detection," Green Analytical Chemistry, vol. 2, p. 100020, 2022.

[91] A. G.-M. Ferrari, P. Carrington, S. J. Rowley-Neale, and C. E. Banks, "Recent advances in portable heavy metal electrochemical sensing platforms," Environmental Science: Water Research & Technology, vol. 6, no. 10, pp. 2676-2690, 2020.

[92] U. O. Aigbe et al., "Electrochemical Detection of Heavy Metals," Modified Nanomaterials for Environmental Applications: Electrochemical Synthesis, Characterization, and Properties, pp. 25-63, 2022.

[93] S. Zhuang, E. S. Lee, L. Lei, B. B. Nunna, L. Kuang, and W. Zhang, "Synthesis of nitrogen-doped graphene catalyst by high-energy wet ball milling for electrochemical systems," International Journal of Energy Research, vol. 40, no. 15, pp. 2136-2149, 2016.

[94] T. P. Yadav, R. M. Yadav, and D. P. Singh, "Mechanical milling: a top down approach for the synthesis of nanomaterials and nanocomposites," Nanoscience and Nanotechnology, vol. 2, no. 3, pp. 22-48, 2012.

[95] R. Ostermann, J. Cravillon, C. Weidmann, M. Wiebcke, and B. M. Smarsly, "Metal–organic framework nanofibers via electrospinning," Chemical Communications, vol. 47, no. 1, pp. 442-444, 2011.

[96] P. S. Kumar et al., "Hierarchical electrospun nanofibers for energy harvesting, production and environmental remediation," Energy & environmental science, vol. 7, no. 10, pp. 3192-3222, 2014.

[97] P. Du et al., "Coaxial electrospun TiO_2/ZnO core–sheath nanofibers film: Novel structure for photoanode of dye-sensitized solar cells," Electrochimica Acta, vol. 78, pp. 392-397, 2012.

[98] A. Pimpin and W. Srituravanich, "Review on micro-and nanolithography techniques and their applications," Engineering Journal, vol. 16, no. 1, pp. 37-56, 2012.

[99] Z. Szabó, J. Volk, E. Fülöp, A. Deák, and I. Bársony, "Regular ZnO nanopillar arrays by nanosphere photolithography," Photonics and Nanostructures-Fundamentals and Applications, vol. 11, no. 1, pp. 1-7, 2013.

[100] C. W. Kuo, J. Y. Shiu, Y. H. Cho, and P. Chen, "Fabrication of large-area periodic nanopillar arrays for nanoimprint lithography using polymer colloid masks," Advanced materials, vol. 15, no. 13, pp. 1065-1068, 2003.

[101] Y. Yin, B. Gates, and Y. Xia, "A soft lithography approach to the fabrication of nanostructures of single crystalline silicon with well-defined dimensions and shapes," Advanced Materials, vol. 12, no. 19, pp. 1426-1430, 2000.

[102] K. Xu and J. Chen, "High-resolution scanning probe lithography technology: a review," Applied Nanoscience, vol. 10, no. 4, pp. 1013-1022, 2020.

[103] R. Matsumoto et al., "Maskless Patterning of Gallium-Irradiated Superconducting Silicon Using Focused Ion Beam," ACS Applied Electronic Materials, vol. 2, no. 3, pp. 677-682, 2020.

[104] V. Garg, R. G. Mote, and J. Fu, "Facile fabrication of functional 3D micro-nano architectures with focused ion beam implantation and selective chemical etching," Applied Surface Science, vol. 526, p. 146644, 2020.

[105] P. Ayyub, R. Chandra, P. Taneja, A. Sharma, and R. Pinto, "Synthesis of nanocrystalline material by sputtering and laser ablation at low temperatures," Applied Physics A, vol. 73, pp. 67-73, 2001.

[106] H. H. Son, G. H. Seo, U. Jeong, and S. J. Kim, "Capillary wicking effect of a Cr-sputtered superhydrophilic surface on enhancement of pool boiling critical heat flux," International Journal of Heat and Mass Transfer, vol. 113, pp. 115-128, 2017.

[107] H. Wender, P. Migowski, A. F. Feil, S. R. Teixeira, and J. Dupont, "Sputtering deposition of nanoparticles onto liquid substrates: Recent advances and future trends," Coordination Chemistry Reviews, vol. 257, no. 17-18, pp. 2468-2483, 2013.

[108] J. Muñoz-García, L. Vázquez, R. Cuerno, J. Sánchez-García, M. Castro, and R. Gago, "Toward functional nanomaterials," ZM Wang. sl: Springer, Dordrecht, p. 323, 2009.

[109] J. H. Nam et al., "Room-temperature sputtered electrocatalyst WSe_2 nanomaterials for hydrogen evolution reaction," Journal of Energy Chemistry, vol. 47, pp. 107-111, 2020.

[110] V. Amendola and M. Meneghetti, "Laser ablation synthesis in solution and size manipulation of noble metal nanoparticles," Physical chemistry chemical physics, vol. 11, no. 20, pp. 3805-3821, 2009.

[111] J. Zhang, M. Chaker, and D. Ma, "Pulsed laser ablation based synthesis of colloidal metal nanoparticles for catalytic applications," Journal of colloid and interface science, vol. 489, pp. 138-149, 2017.

[112] R. A. Ismail, M. H. Mohsin, A. K. Ali, K. I. Hassoon, and S. Erten-Ela, "Preparation and characterization of carbon nanotubes by pulsed laser ablation in water for

optoelectronic application," Physica E: Low-dimensional Systems and Nanostructures, vol. 119, p. 113997, 2020.

[113] J. Chrzanowska et al., "Synthesis of carbon nanotubes by the laser ablation method: Effect of laser wavelength," physica status solidi (b), vol. 252, no. 8, pp. 1860-1867, 2015.

[114] J. S. Duque, B. M. Madrigal, H. Riascos, and Y. P. Avila, "Colloidal metal oxide nanoparticles prepared by laser ablation technique and their antibacterial test," Colloids and Interfaces, vol. 3, no. 1, p. 25, 2019.

[115] S. S. Su and I. Chang, "Review of production routes of nanomaterials," Commercialization of nanotechnologies–a case study approach, pp. 15-29, 2018.

[116] H. Naser et al., "The role of laser ablation technique parameters in synthesis of nanoparticles from different target types," Journal of Nanoparticle Research, vol. 21, pp. 1-28, 2019.

[117] A. C. Jones and M. L. Hitchman, "Overview of chemical vapour deposition," Chemical Vapour Deposition: Precursors, Processes and Applications, vol. 1, pp. 1-36, 2009.

[118] K. Shah and B. Tali, "Materials science in semiconductor processing synthesis of carbon nanotubes by catalytic chemical vapour deposition: a review on carbon sources, catalysts and substrates," Mater. Sci. Semicond. Process, vol. 41, pp. 67-82, 2016.

[119] T. Chiawchan, H. Ramamoorthy, K. Buapan, and R. Somphonsane, "CVD Synthesis of Intermediate State-Free, Large-Area and Continuous MoS_2 via Single-Step Vapor-Phase Sulfurization of MoO_2 Precursor," Nanomaterials, vol. 11, no. 10, p. 2642, 2021.

[120] X. Wu, G. Q. M. Lu, and L. Wang, "Shell-in-shell TiO_2 hollow spheres synthesized by one-pot hydrothermal method for dye-sensitized solar cell application," Energy & Environmental Science, vol. 4, no. 9, pp. 3565-3572, 2011.

[121] S. Cao, C. Zhao, T. Han, and L. Peng, "Hydrothermal synthesis, characterization and gas sensing properties of the WO_3 nanofibers," Materials Letters, vol. 169, pp. 17-20, 2016.

[122] J. Li, Q. Wu, and J. Wu, "Handbook of nanoparticles," 2015.

[123] A. Chen and P. Holt-Hindle, "Platinum-based nanostructured materials: synthesis, properties, and applications," Chemical reviews, vol. 110, no. 6, pp. 3767-3804, 2010.

[124] L.-Y. Meng, B. Wang, M.-G. Ma, and K.-L. Lin, "The progress of microwave-assisted hydrothermal method in the synthesis of functional nanomaterials," Materials Today Chemistry, vol. 1, pp. 63-83, 2016.

[125] Y. Dong, X.-q. Du, P. Liang, and X.-l. Man, "One-pot solvothermal method to fabricate 1D-VS4 nanowires as anode materials for lithium ion batteries," Inorganic Chemistry Communications, vol. 115, p. 107883, 2020.

[126] Y. Jiang et al., "Facile in-situ Solvothermal Method to synthesize double shell $ZnIn_2S_4$ nanosheets/TiO_2 hollow nanosphere with enhanced photocatalytic activities," Ceramics International, vol. 44, no. 6, pp. 6115-6126, 2018.

[127] B. Chai, M. Xu, J. Yan, and Z. Ren, "Remarkably enhanced photocatalytic hydrogen evolution over MoS_2 nanosheets loaded on uniform CdS nanospheres," Applied Surface Science, vol. 430, pp. 523-530, 2018.

[128] B. P. Kafle, "Introduction to nanomaterials and application of UV–Visible spectroscopy for their characterization," Chemical analysis and material characterization by spectrophotometry, vol. 6, pp. 147-198, 2020.

[129] A. E. Danks, S. R. Hall, and Z. Schnepp, "The evolution of 'sol–gel'chemistry as a technique for materials synthesis," Materials Horizons, vol. 3, no. 2, pp. 91-112, 2016.

[130] T. K. Tseng, Y. S. Lin, Y. J. Chen, and H. Chu, "A review of photocatalysts prepared by sol-gel method for VOCs removal," International journal of molecular sciences, vol. 11, no. 6, pp. 2336-2361, 2010.

[131] M. Parashar, V. K. Shukla, and R. Singh, "Metal oxides nanoparticles via sol–gel method: a review on synthesis, characterization and applications," Journal of Materials Science: Materials in Electronics, vol. 31, pp. 3729-3749, 2020.

[132] L. Znaidi, "Sol–gel-deposited ZnO thin films: A review," Materials Science and Engineering: B, vol. 174, no. 1-3, pp. 18-30, 2010.

[133] C. de Coelho Escobar and J. H. Z. dos Santos, "Effect of the sol–gel route on the textural characteristics of silica imprinted with Rhodamine B," Journal of separation science, vol. 37, no. 7, pp. 868-875, 2014.

[134] R. Somphonsane, T. Chiawchan, W. Bootsa-ard, and H. Ramamoorthy, "CVD Synthesis of MoS2 Using a Direct MoO2 Precursor: A Study on the Effects of Growth Temperature on Precursor Diffusion and Morphology Evolutions," Materials, vol. 16, no. 13, p. 4817, 2023.

[135] M. Legrand et al., "Alpine-ice record of bismuth pollution implies a major role of military use during World War II," Scientific Reports, vol. 13, no. 1, p. 1166, 2023.

[136] R. Wang, H. Li, and H. Sun, "Bismuth: environmental pollution and health effects," Encyclopedia of environmental health, p. 415, 2019.

[137] C. D. Klaassen and M. O. Amdur, Casarett and Doull's toxicology: the basic science of poisons. McGraw-Hill New York, 2013.

CHAPTER 3

3 Experiments

In this chapter, detailed descriptions of the experiments involved in the synthesis and fabrication process are provided. The chapter covers the synthesis procedure for pure Ni_2O_3 as well as its metal doping with Cu and Fe. Additionally, the fabrication of the working electrode and resistive sensor is explained.

3.1 Synthesis of sensing material

Transitional metal oxides, such as $Co3O_4$, Mn_3O_4, NiO, and ZnO, were synthesized using a straightforward hydrothermal method. The hydrothermal synthesis approach offers several advantages, including simplicity, scalability, and the ability to control the size, morphology, and crystallinity of the resulting nanostructures. [1-4].

3.1.1 Synthesis of Ni_2O_3

Pure Ni_2O_3 is synthesized at room temperature by a facile oxidation process reported by Dey et al. [5].

3.1.1.1 Chemicals and instruments

Nickel nitrate hexahydrate ($Ni(NO_3)_2.6H_2O$), sodium hydroxide (NaOH), and sodium hypochlorite with 4% active chlorine (NaOCl) were purchased from Sigma-Aldrich. The instruments involved in the synthesis process are magnetic stirrer, centrifuge, ultrasonic bath sonicator, and hot air oven.

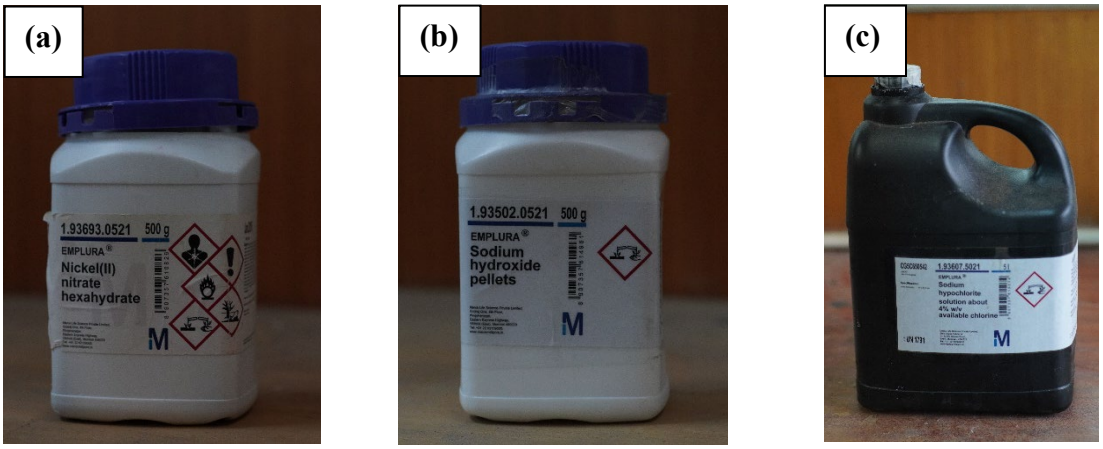

Figure 3.1: Image of the precursors (a) $Ni(NO_3)_2 \cdot 6\ H_2O$, (b) NaOH, (c) NaOCl

3.1.1.2 Synthesis procedure

In a standard procedure, Nickel (II) nitrate hexahydrate weighing 1.57 g was dissolved in 60 mL of deionized (DI) water while being continuously stirred, resulting in a uniform solution. Simultaneously, 1.6 g of NaOH was dissolved in 15 mL of NaOCl solution with 4% active chlorine concentration, creating an alkaline NaOCl solution. This alkaline solution was then gradually added drop by drop to the $Ni(NO_3)_2 \cdot 6H_2O$ solution under constant stirring, forming flocculates. The stirring process was maintained for one hour, forming black precipitates identified as $Ni_2O_3 \cdot xH_2O$. To separate the precipitates, the mixture was filtered using filter paper, and the obtained solid was dried to obtain a powdered form of $Ni_2O_3 \cdot xH_2O$. This powder was then transferred to a beaker.

(a)

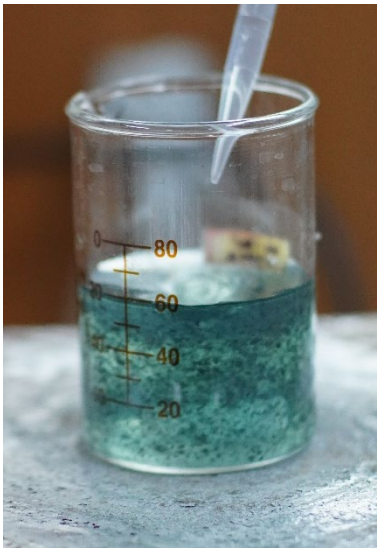

(b)

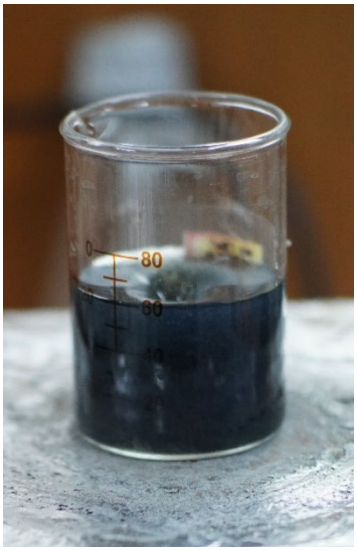

Figure 3.2: (a) Black flocculates after adding alkaline NaOCl (b) Hydrated Ni_2O_3 completely dispersed after stirring

Following this, 20 mL of NaOCl solution was added to the beaker containing the $Ni_2O_3 \cdot xH_2O$ powder, and the mixture was stirred for an additional hour. This step aimed to create a suspension of the precipitate. The suspension was then left undisturbed overnight until the bubbling stopped. Afterward, the black precipitate was washed with NaOCl solution and subsequently subjected to centrifugation at 14,000 rpm. Finally, the resulting precipitate was dried, resulting in the obtainment of pure Ni_2O_3.

3.1.2 Metal doping of Ni_2O_3

Metal doping of Ni_2O_3 is performed using an in situ hydrothermal procedure, specifically employing iron and copper as dopants.

3.1.2.1 Chemicals and materials

Nickel nitrate hexahydrate ($Ni(NO_3)_2.6H_2O$), copper sulphate pentahydrate ($CuSO_4.5H_2O$), ferrous sulphate heptahydrate ($FeSO_4.7H_2O$), sodium hydroxide (NaOH), urea ($(NH_2)_2CO$), polyethylene glycol 600 (PEG 600), and sodium hypochlorite with 4% active chlorine (NaOCl) were purchased from Sigma-Aldrich. The instruments involved in the synthesis process are magnetic stirrer, centrifuge, ultrasonic bath sonicator and hot air oven.

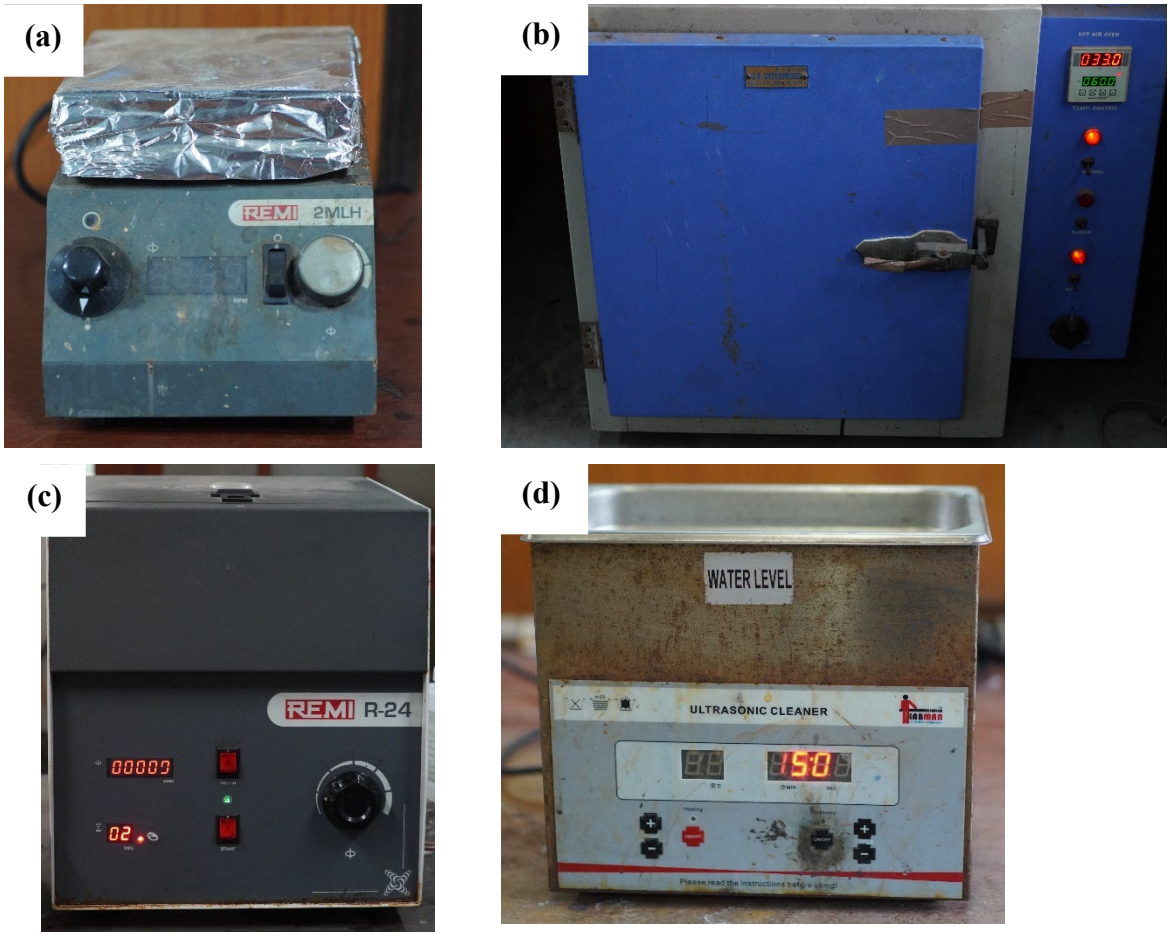

Figure 3.3: Instruments used in synthesis (a) Magnetic stirrer, (b) Hot air oven, (b) Centrifuge, (d) Ultrasonic bath sonicator

3.1.2.2 Synthesis procedure

Doped Nickel(III) oxide (Ni_2O_3) was synthesized through a multi-step process.

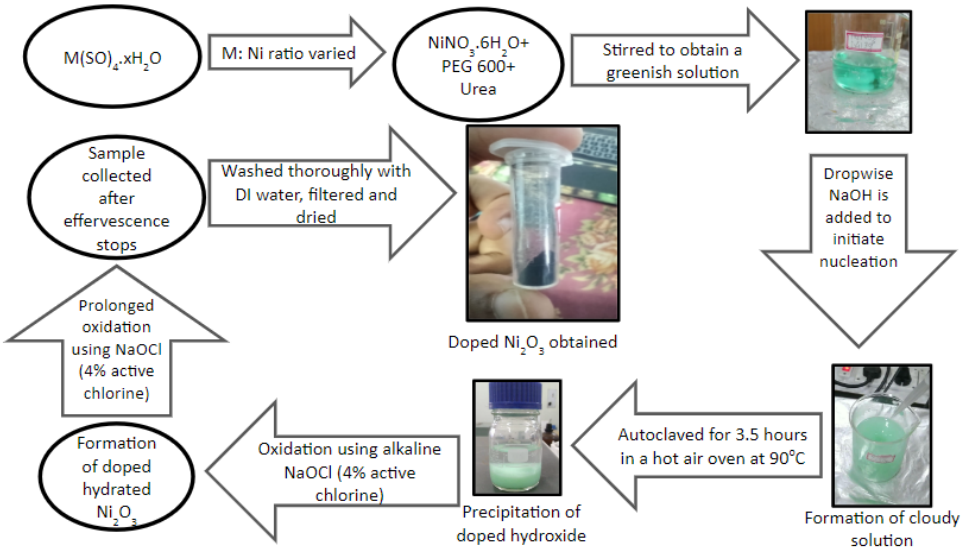

Figure 3.4: Schematic of doping of Nickel (III) oxide (applied for both Fe and Cu doping)

Step 1: Preparation of Metal Salt Solutions

- Nickel(II) nitrate hexahydrate ($NiNO_3 \cdot 6H_2O$) and the respective metal sulfate ($MSO_4 \cdot xH_2O$) (M = Cu, Fe) were weighed out to ensure the molar ratio between the metals and nickel was maintained.
- The weighed metal salts were dissolved in 60 mL of deionized water (DI water), ensuring complete dissolution and homogeneity.

Step 2: Formation of Clear Greenish Solution

- A mixture of equimolar polyethylene glycol 600 (PEG 600) and urea was prepared.
- The PEG 600-urea mixture was gradually added to the metal salt solutions while stirring until a clear greenish solution was obtained.

Step 3: Nucleation

- The pH of the solution was adjusted to 11 by dropwise addition of sodium hydroxide (NaOH).
- The solution turned cloudy, indicating nucleation and the formation of hydroxide precipitates.

Step 4: Hydrothermal reaction

- The cloudy solution was transferred into a Schott bottle and tightly sealed.
- The Schott bottle was placed inside a hot air oven and maintained at a temperature of 90^{o} C for 3.5 hours, allowing precipitation to occur.

- After the heating process, the Schott bottle was naturally cooled to room temperature.
- As the solution cooled, hydroxide precipitates formed.

Step 5: Oxidation and Formation of Doped Hydrated Nickel(III) Oxide then pure Nickel(III) oxide

- The hydroxide precipitate was treated with alkaline sodium hypochlorite (NaOCl) solution which was been prepared simultaneously.

- The mixture was left in contact with the NaOCl solution overnight until effervescence stopped. This prolonged oxidation process converted the doped hydroxide into doped hydrated Nickel(III) oxide.

Step 6: Washing and Drying

- The precipitate was carefully separated from the solution by filtration or centrifugation.
- The obtained precipitate was washed several times with deionized water to remove any impurities or residual reactants.
- The washed precipitate was thoroughly dried to obtain pure doped Ni_2O_3.

3.2 Slurry preparation and fabrication of working electrode for electrochemical sensing

3.2.1 Materials and chemicals used

Polyvinylidene fluoride (PVDF), N-methyl-2-pyrrolidone (NMP), and activated carbon

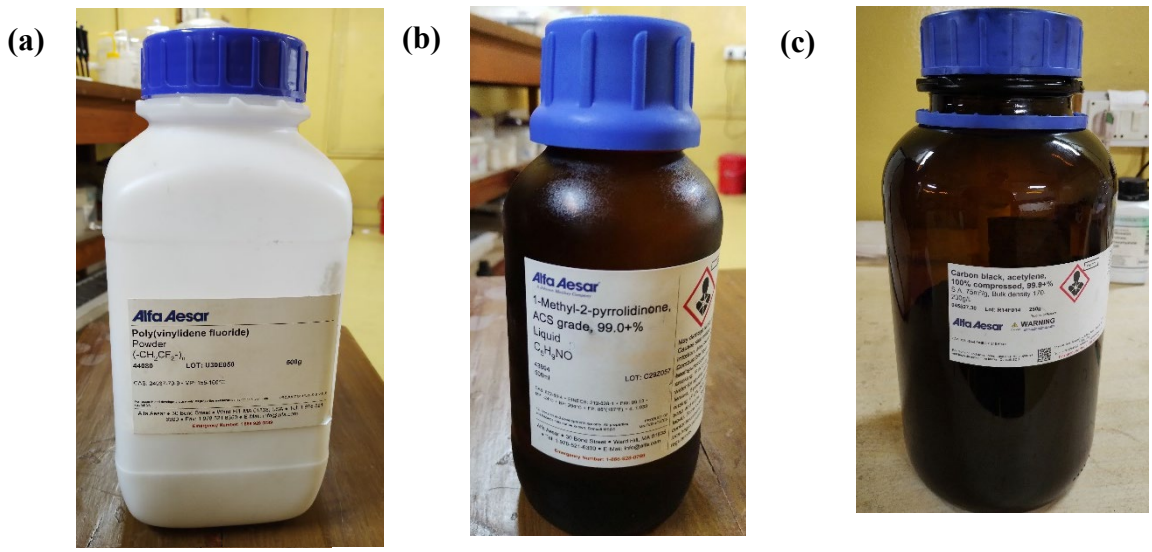

Figure 3.5: (a) Polyvinylidene fluoride (PVDF), (b) N-methyl-2-pyrrolidone (NMP), (c) activated carbon

3.2.2 Slurry preparation

For the preparation of the electrode slurry, a total of 300 mg of Ni_2O_3 was carefully weighed out. To improve the stability and binding properties of the slurry, 24 g of

Polyvinylidene fluoride (PVDF), a commonly used binder, was added. Additionally, 24 g of activated carbon was incorporated into the slurry to enhance its conductivity. The measured quantities of the synthesized material, PVDF, and activated carbon were combined in a mortar and pestle, and an even mixture was obtained through thorough grinding and mixing. This process ensured that the components were evenly distributed within the slurry. Subsequently, the mixture was transferred into a small vial, which would serve as the container for the slurry. To achieve the desired consistency and facilitate the easy application of the slurry, 1.392 ml of N-methyl-2-pyrrolidone (NMP), a commonly used solvent, was added to the vial. NMP has excellent solvating properties and is often employed in slurry preparation for its ability to dissolve PVDF effectively. Once the NMP was added, the solution was stirred continuously overnight. This extended stirring duration allowed for complete dispersion and wetting of the components, resulting in the formation of a black, homogeneous substance. During this period, the PVDF dissolved in NMP, promoting the formation of a uniform slurry and ensuring the effective binding of the synthesized material and activated carbon.

Figure 3.6: Image of Ni_2O_3 slurry

3.2.3 Electrode fabrication

In the electrode preparation process, a piece of graphite sheet with precise dimensions of 5 mm x 30 mm was cut as the substrate. The graphite sheet, known for its excellent electrical conductivity and stability, served as a suitable foundation for the deposition of the synthesized material. To incorporate the synthesized material into the electrode, 10 µL of the slurry, carefully measured using a micropipette, was deposited on one side of the graphite sheet. The slurry was uniformly spread over an area of 22 mm x 5 mm, ensuring a consistent

and controlled distribution of the active material. This deposition area was chosen to optimize the utilization of the synthesized material while allowing sufficient space for subsequent analysis and measurements.

After the slurry was applied to one side of the electrode, the sheet was transferred to a vacuum oven for drying. The vacuum oven provided an environment of reduced pressure, which facilitated the evaporation of the solvent from the slurry. Concurrently, the oven maintained a controlled temperature, ensuring gentle and efficient drying without causing damage to the electrode or synthesized material. The drying process continued until all traces of the solvent were removed, leaving behind a dry and stable layer of the synthesized material adhered to the electrode surface. Following the completion of the first-side drying, the electrode was flipped, and the same deposition and drying procedure was repeated for the other side. This symmetrical approach ensured that both sides of the electrode contained an equal amount of the synthesized material, promoting uniformity in the electrochemical properties and performance.

Once the slurry was deposited on both sides of the electrode and dried, the weight of the dry material deposited on the sheet was precisely measured, yielding a value of 9.5 mg. This measurement was crucial as it provided quantitative information regarding the loading density of the synthesized material on the electrode. Once both sides of the electrode were

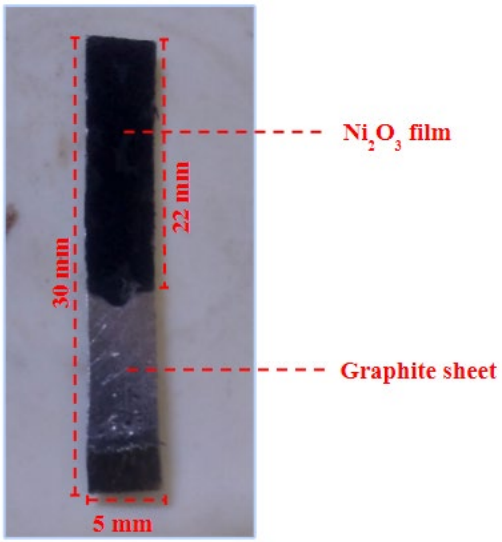

Figure 3.7: Image of working electrode

coated with the slurry, the electrode was subjected to thorough drying in the vacuum oven. This drying process enabled the complete removal of residual solvent, resulting in a dry and

stable layer of the synthesized material on both sides of the electrode. The weight of the dry material deposited on the graphite sheet was precisely measured to be 9.5 mg. This measurement provided valuable information about the loading density of the synthesized material on the electrode and served as a reference for future calculations and comparisons.

3.3 Fabrication of the resistive sensor

To prepare a thin film of nickel oxide (Ni_2O_3) on a gold-plated interdigitated electrode (IDE) for potential sensing applications. The procedure involved dispersing 5 mg of Ni_2O_3 powder in 1 ml of deionized water using ultrasonication for 30 minutes. Subsequently, a 10 µL aliquot of the resulting suspension was drop cast onto the IDE and allowed to dry at 70°C for 2 hours, resulting in the formation of a thin film of Ni_2O_3.

To facilitate the drying process and promote the adhesion of the Ni_2O_3 film, the drop-cast sample was dried at 70°C for 2 hours. This temperature was chosen based on previous studies indicating that it is sufficient to evaporate the water while maintaining the integrity of the film. The gold-plated IDE offers good electrical conductivity and serves as a substrate for the Ni_2O_3 film. Figure X shows the image of the fabricated device with the drop-cast Ni_2O_3 film on the IDE.

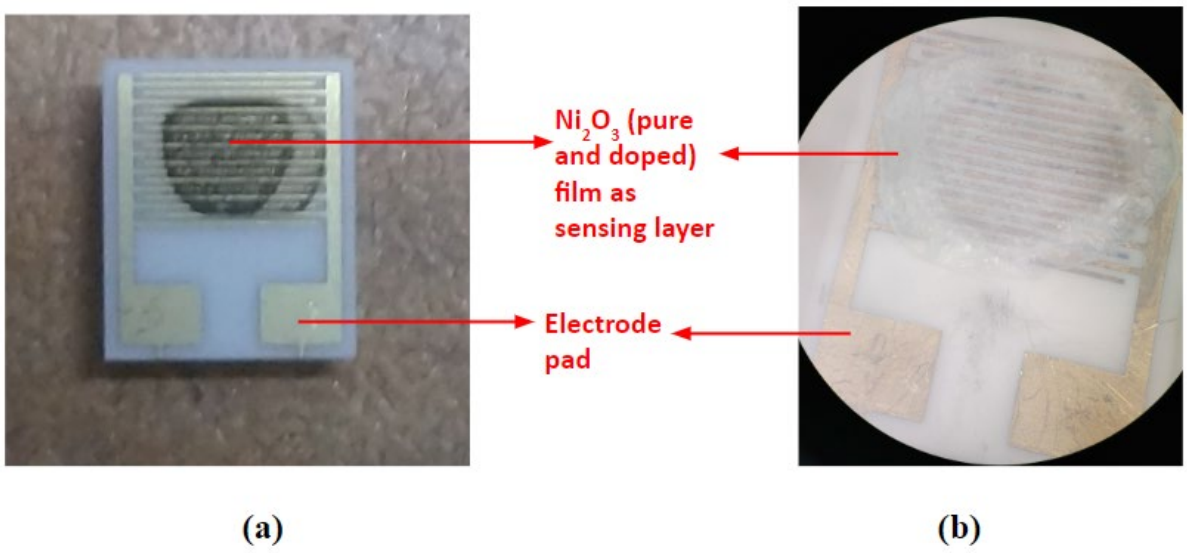

Figure 3.8: Ni_2O_3 (both pure and doped) based sensing device using IDE (a) normal image (b) under the microscope

References

[1] H. Li, Z. Lu, J. Wu, H. Yu, X. Yu, and R. Chen, "Hydrothermal synthesis of transition metal oxide nanomaterials in HEPES buffer solution," Materials Letters, vol. 64, no. 18, pp. 1939-1942, 2010.

[2] A. Nandagudi et al., "Hydrothermal synthesis of transition metal oxides, transition metal oxide/carbonaceous material nanocomposites for supercapacitor applications," Materials Today Sustainability, p. 100214, 2022.

[3] S. Dey, S. Santra, S. Sen, D. Burman, S. K. Ray, and P. K. Guha, "Photon-assisted ultra-selective formaldehyde sensing by defect induced NiO-based resistive sensor," IEEE Sensors Journal, vol. 18, no. 14, pp. 5656-5661, 2018.

[4] M. Bhattacharya, S. Dey, and C. K. Ghosh, "N-type TiO_2-based reusable sensor for photon-assisted Cd (II) ion detection," IEEE Transactions on Electron Devices, vol. 68, no. 6, pp. 2951-2956, 2021.

[5] S. Dey, S. Bhattacharjee, M. G. Chaudhuri, R. S. Bose, S. Halder, and C. K. Ghosh, "Synthesis of pure nickel (III) oxide nanoparticles at room temperature for Cr (VI) ion removal," RSC Advances, vol. 5, no. 67, pp. 54717-54726, 2015.

CHAPTER 4

4 Instruments

This chapter describes the instrumentation involved, including the morphological and structural study. It also covers the sensing setup, which includes the electrochemical and semiconductor parameter analyzers.

4.1 Structural and morphological study

There are two steps in the characterization of these nanomaterials, which involves morphological analysis and structural analysis. Morphological characterizations were carried out using microscopic techniques such as electron microscopy, optical microscopy, scanning probe microscopy (SPM), etc. Structural analysis was carried out using X-ray diffraction (XRD), Fourier transform infrared spectroscopy (FTIR), Raman spectroscopy, etc [[1,2]

The study of new physical properties and applications of nanomaterials or nanostructures are possible only when nanostructured materials are made available with the desired size, morphology, and chemical composition[3]. The electronic structure of nanoparticles can reveal semiconductor, metallic, or insulator character. The unique chemical and physical properties of metal oxide nanoparticles are attributed to the high density and limited size of corners and edges on their surface [4].

4.1.1 Scanning Electron Microscope (SEM)

The scanning electron microscope (SEM) is a highly versatile tool for analyzing and interpreting the morphology of microstructures. It employs a focused electron beam to scan the surface of an object, generating a multitude of signals. These electron signals are converted into an image displayed on a cathode ray tube (CRT).

The SEM utilizes two methods to generate the electron beam:

1) Thermionic emission
2) Field emission.

Thermionic emission involves using thermal energy to control the emission of electrons from the source. However, in modern electron microscopes, field emission electron guns (FEG) are commonly used instead of thermionic electron guns. The FEG allows for the observation of very fine surface topographic features on whole or fragmented objects. This technique is extensively utilized by researchers in biology, chemistry, and physics to examine structures as small as 1 nanometer, providing insights into organelles and DNA material within cells, synthetic polymers, and microchip coatings.

4.1.1.1 Components of FESEM

- **Electron Guns**

Modern field emission scanning electron microscope (FESEM) systems consist of a continuous electron beam emitted by the electron gun, characterized by high current, small spot size, adjustable energy, and minimal energy dispersion. Various types of electron guns are employed in FESEM systems, and the quality of the electron beam they produce varies significantly. The initial FESEM systems used tungsten "hairpin" or lanthanum hexaboride (LaB_6) cathodes, but these have been replaced by field emission sources that offer higher current and reduced energy dispersion. When selecting electron sources, the longevity of the emitter is a critical factor to consider.

- **Electron lenses**

Electron beams can be focused using either electrostatic or magnetic fields, but the FESEM system relies exclusively on a magnetic field due to its ability to minimize aberrations in the electron beam. Electromagnets can be utilized to manipulate the paths of the electrons.

♦ **Condenser lenses**

After passing through an anode plate, the electron beam tends to scatter. However, to achieve a parallel and concentrated stream, the condenser lens is used. This lens effectively converges and aligns the beam to make it nearly parallel. To accomplish this, a magnetic lens consisting of two symmetrical iron pole pieces, accompanied by a copper winding, is employed. The copper winding generates a magnetic field, while the pole pieces have a central aperture through which the electron beam can travel. The magnetic field, formed between the two pole pieces, plays a crucial role in shaping and focusing the

electron beam. By adjusting the current in the condenser lens, the focal point of the beam can be modified, providing control and versatility in the functioning of the instrument.

- **Scan coils**

The electron beam undergoes a zigzag motion as it traverses the object due to the action of scan coils. This zigzag scanning pattern is synchronized with the image formation on the display. The scan speed not only determines the refresh rate of the screen but also affects the level of noise present in the resulting image. To prevent the formation of circular shadows at low magnification, it is common practice to employ both upper and lower coils in the scan coil system.

- **Objective lens**

Below the condenser aperture, the electron beam tends to spread out. To counter this divergence, objective lenses are employed to further de-magnify the beam and concentrate it into a specific probe point on the surface of the specimen. The size of the electron beam on the specimen surface, known as the spot size, plays a crucial role in determining the image resolution. As the aperture size and the fundamental principles of Scanning Electron Microscopy are enhanced, the spot size of the electron beam decreases, leading to improved image resolution.

- **Stigmator coil**

The stigmator coils are employed to correct any irregularities in the x and y deflection of the electron beam, ensuring its circular shape. When the beam deviates from a perfect circle and becomes ellipsoidal, it leads to a distorted and blurry image. By utilizing the stigmator coils, these inconsistencies are rectified, resulting in a crisp and accurately proportioned beam.

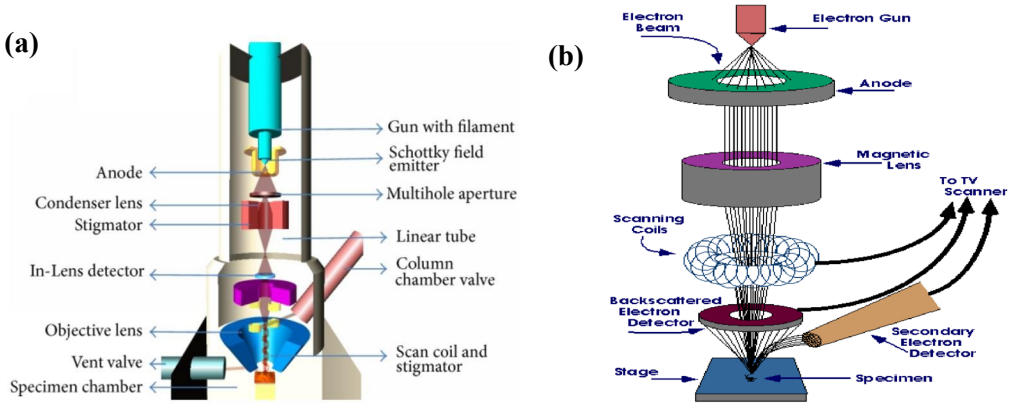

Figure 4.1: (a) Principle of Operation of FESEM (b) Schematic Diagram of FESEM (adopted from [1], [5])

- **Object chamber**

Prior to placement on a specialized holder, the object undergoes a process of coating with a conductive material. This coated object is securely positioned on a movable stage, which is then introduced into the high vacuum section of the microscope through an exchange chamber. Within the chamber, the secondary electron emission detector, known as the scintillator, is positioned behind the object holder.

- **Image information**

In a FESEM, when an electron beam strikes the surface of a specimen, a range of complex interactions occur, resulting in the generation of various signals that are crucial for FESEM analysis. These signals include secondary electrons, backscattered electrons (BSEs), transmitted electrons, and specimen current, which can be collected and displayed on a monitor. Additionally, to determine the composition of the specimen, the excited x-ray or Auger electrons are examined. This section will delve into the interactions between the electron beam and the specimen surface, as well as the underlying principles involved in producing images from different signal types.

4.1.2 X-ray diffraction (XRD)

X-ray is a type of electromagnetic radiation, that possesses high energy and short wavelengths that are similar in scale to the atomic spacing within solids. When a beam of X-rays interacts with a solid material, some of the X-ray photons will be scattered in all directions due to their interaction with the electrons associated with each atom or ion in the beam's path. Now, let's explore the necessary conditions for X-ray diffraction by a periodic arrangement of atoms. Diffraction occurs when a wave encounters a series of regularly spaced obstacles capable of scattering the wave, with spacing comparable to the wavelength. The occurrence of diffraction is a consequence of specific phase relationships that form between two or more waves scattered by the obstacles. The phase relationship depends on the difference in path length between the scattered waves, where an important case arises when the path length is a whole number of wavelengths.

- **Bragg's law**

Let's consider two parallel planes of atoms with identical h, k, and l Miller indices, separated by a distance called the interplanar spacing (d). Now, imagine a parallel,

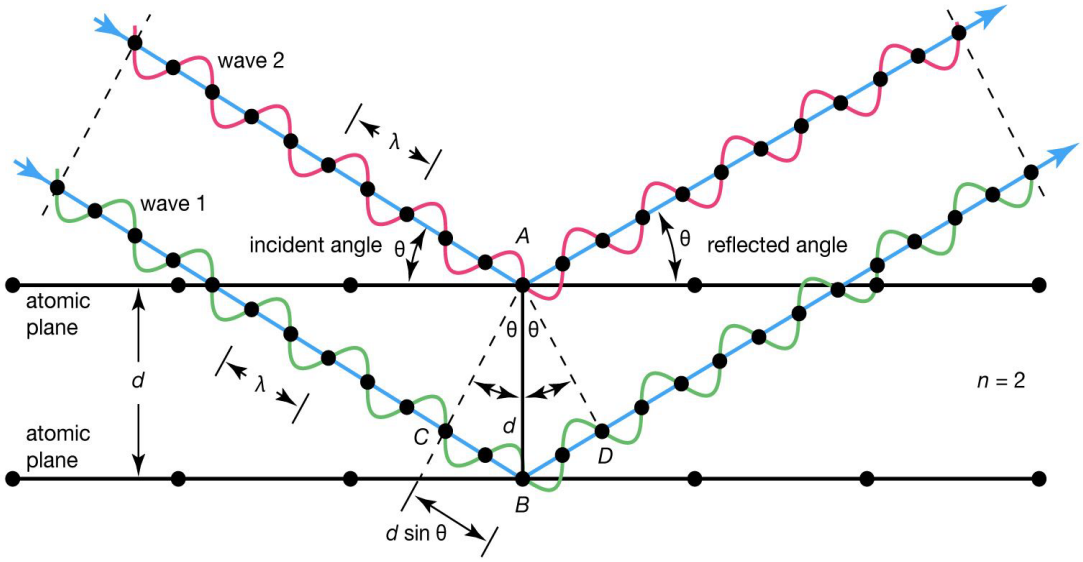

Figure 4.2: Brag's Law of diffraction (adopted from [6])

monochromatic, and coherent (in-phase) beam of X-rays with a wavelength (λ) incident on these planes at an angle (θ). As the X-rays interact with atoms A and B, two scattered rays are formed. When the path length difference (CB+BD) between these scattered waves is equal to a whole number (n) of wavelengths, constructive interference occurs at an angle (θ) relativeto the planes. This condition is crucial for diffraction to take place.

So, the condition for diffraction is

$$n\lambda = CB + BD$$

$$\text{or, } n\lambda = d\sin\theta + d\cos\theta$$

$$\text{or, } n\lambda = 2d\sin\theta \qquad (4.1)$$

- **Production of X-ray**

X-rays are generated by directing a stream of electrons emitted from a heated filament (typically made of tungsten) towards a metallic target, commonly copper (Cu) or molybdenum (Mo). When the incident electron beam interacts with the target atoms, it causes

the ionization of electrons from the K-shell (1s) of the target atom. As a result, X-rays are emitted as other electrons transition from the higher energy L (2p) or M (3p) levels to fill the resulting vacancies in the K-shell. These transitions give rise to specific X-ray spectral lines known as K_α and K_β lines.

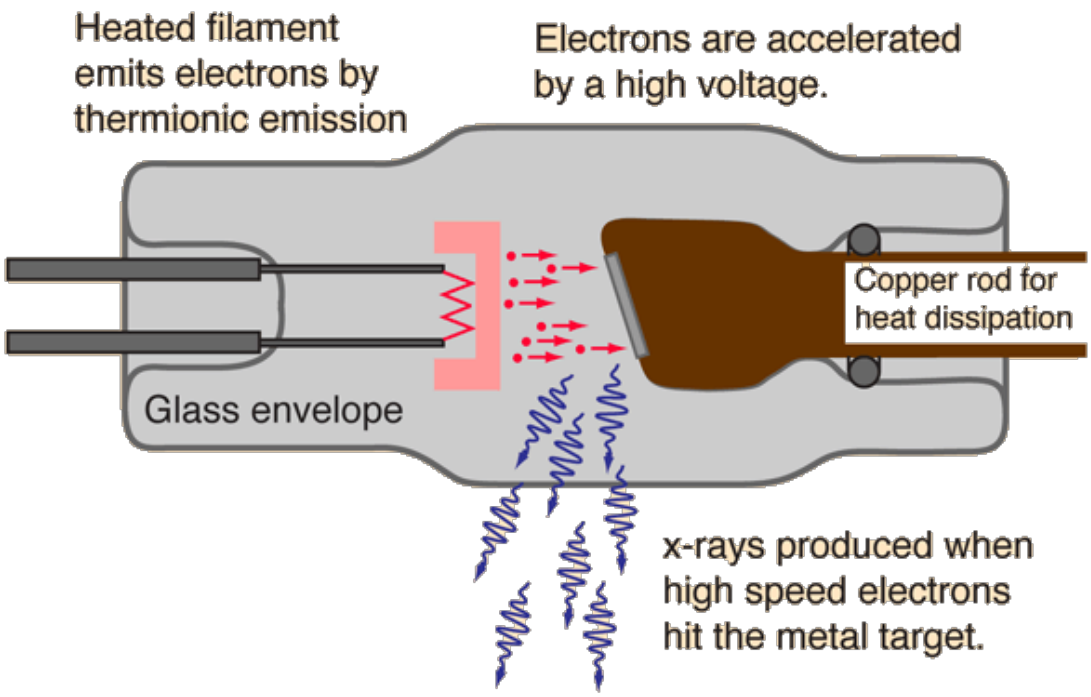

Figure 4.3: Production of X-Rays (adopted from [7])

4.1.2.1 Scherrer equation

In 1918, P. Scherrer conducted an experiment that demonstrated a phenomenon wherein a broadening of the diffracted beam occurs when parallel monochromatic X-ray radiation is directed onto a collection of randomly oriented crystals of small particle size. This observation by Scherrer holds significant relevance in the context of my thesis, as it highlights the relationship between particle size and the resulting diffraction patterns. By investigating this broadening effect, we can gain a deeper understanding of the structural characteristics and properties of materials at the nanoscale. This phenomenon has since become an essential tool in the field of crystallography, enabling researchers to analyze and quantify the particle size distribution in a variety of crystalline materials [8].

The average grain size of the samples was calculated using Scherrer's formula:

$$D = \frac{0.94\lambda}{\beta \cos\theta} \qquad (4.2)$$

Where λ is the wavelength of x-rays, and β is the full width at half maximum intensity in radians.

It is crucial to understand that the Scherrer's formula provides a conservative estimate for the particle size, setting a lower limit. This is due to the fact that various factors, such as inhomogeneous strain and instrumental errors, can contribute to the broadening of a diffraction peak. While particle size is an important factor, it is not the sole determinant of peak width. If all the other factors influencing peak width were absent, the particle size would exclusively determine the width, aligning with the applicability of Scherrer's formula. However, in real-world scenarios where these additional contributors exist, the particle size may exceed the prediction provided by the formula. Consequently, the observed peak width can be broader than expected, with the "extra" width attributed to these other factors.

It is crucial to recognize that relying solely on Scherrer's formula may underestimate the particle size due to the presence of these contributing factors. Therefore, a comprehensive analysis should consider and account for these additional influences to accurately determine the particle size and interpret diffraction peak characteristics [9].

4.1.2.2 Microstrain

Microstrain in a crystal lattice refers to the local distortions or deviations from the ideal lattice structure on a microscopic scale. It is typically caused by a variety of factors, such as impurities (doping), defects, thermal expansion, and external stresses [10]. When a crystal lattice is subjected to any of these influences, the regular arrangement of atoms or ions within the lattice is perturbed. These perturbations can manifest as local strain fields that affect the interatomic distances, bond angles, and overall symmetry of the lattice [11,12]. The magnitude of the microstrain is typically expressed as a fractional change in the lattice parameters or interatomic distances. It is commonly measured using techniques such as X-ray diffraction, neutron diffraction [13,14].

X-ray diffraction (XRD) peak shifts can be used to analyze microstrain in crystals. By applying Bragg's law, we can explain how microstrain influences the peak positions in XRD patterns.

Bragg's law relates the scattering of X-rays from crystal planes to the interplanar spacing (d), the incident angle (θ), and the wavelength of X-rays (λ). According to Bragg's law:

$2d \sin(\theta) = n\lambda$ (explained in detail in section 4.1.2)

Microstrain causes a variation in the interplanar spacing across different regions of the crystal lattice. As a result, the XRD peaks associated with specific crystal planes will experience slight shifts due to the different effective interplanar spacings in different regions [15,16].

The magnitude and direction of the peak shift depend on the nature of the microstrain. For instance, if there is tensile microstrain, the interplanar spacing increases, and the corresponding diffraction peaks shift to lower angles. Conversely, compressive microstrain decreases the interplanar spacing, resulting in peak shifts towards higher angles [11,16].

4.1.2.3 Williamson-Hall analysis

The Scherrer formula focuses solely on the influence of crystallite size on XRD peak broadening and does not provide information about the lattice's microstructures or intrinsic strain in nanocrystals resulting from factors like point defects, grain boundaries, triple junctions, and stacking faults [17, 18]. Several techniques, including Williamson's Hall method, Warren-Averbach method, etc., take into account the influence of strain-induced XRD peak broadening and can be employed to calculate both the intrinsic strain and particle size. Among these methods, the Williamson-Hall (W-H) method is a simplified and straightforward approach [19, 20]. According to which, physical line broadening of X-ray diffraction peak occurs due to the size and microstrain of the nanocrystals and the total broadening can be written as,

$$\beta_{hkl} = \beta_{size} + \beta_{strain} \qquad (4.3)$$

Where, β_{hkl} is the full width at half of the maximum intensity for different diffraction planes.

$$\beta_{hkl} = \frac{0.94\lambda}{D}.\frac{1}{\cos\theta} + 4\varepsilon.tan\theta$$

$$\text{or, } \beta_{hkl}.cos\theta = \frac{0.94\lambda}{D} + 4\varepsilon.sin\theta \qquad (4.4)$$

This is the equation of a straight line. The slope of this straight line provides the value of the intrinsic strain, whereas the intercept gives the average particle size of the nanocrystals. The lattice strain in nanocrystals primarily arises from the expansion or contraction of the lattice structure caused by size confinement. When nanocrystals are constrained in size, their atomic arrangement undergoes slight modifications compared to their bulk counterparts, leading to lattice strain. Additionally, size confinement induces the formation of various defects within the lattice structure, further contributing to lattice strain.

4.1.2.4 Size-strain plot

The Williamson-Hall method takes into account the broadening of peaks based on the diffraction angle (2θ), assuming it is a result of both size-induced and strain-induced broadening. However, there are alternative models that analyze the peak profile in a different way. One such method is the Size-Strain plot (SSP), which considers the X-ray diffraction (XRD) peak profile as a combination of a Lorentzian function and a Gaussian function. In this approach, the size-broadened XRD profile is represented by the Lorentzian function, while the strain-broadened profile is represented by the Gaussian function [18].

$$\beta_{hkl} = \beta_L + \beta_G \qquad (4.5)$$

Where β_L and β_G are the peak broadening due to Lorentz and Gaussian function respectively

Furthermore, the SSP approach consistently delivers better outcomes for isotropic broadening because it emphasizes low-angle reflections, which have greater accuracy and precision than reflections at higher angles. This is due to the decreased quality of XRD data at higher angles and the typical significant peak overlap at higher diffracting angles. As a result, the SSP calculation is carried out using equation [21], as shown below.

$$(d_{hkl}.\beta_{hkl}.cos\theta)^2 = \frac{k\lambda}{D}.\left(d_{hkl}{}^2.\beta_{hkl}.cos\theta\right) + \frac{\varepsilon^2}{4} \qquad (4.6)$$

Where d_{hkl} is the lattice distance between the (hkl) planes and for the cubic crystal. This equation represents a straight line. The slope of the straight line provides the average size and the intercept gives the intrinsic strain of the nanocrystals.

4.1.2.5 Rietveld refinement

The Rietveld refinement method was developed by Hugo Rietveld during the late 1960s as a powerful technique for characterizing crystalline materials. Initially introduced in 1967 and subsequently documented in 1969, it focused on the analysis of monochromatic neutron diffraction data. Rietveld modestly named the method the "Profile Refinement Method" in recognition of the earlier contributions made by other researchers. However, during a notable Neutron conference held in Cracow, Terry Sabine and Ray Young proposed renaming it the "Rietveld Method," a suggestion that gained acceptance from the Commission on Neutron Diffraction [22].

The Rietveld refinement method has also found wide application in X-ray diffraction (XRD) analysis and remains the most commonly used technique for powder XRD refinement today. It involves fitting a calculated profile, incorporating structural and instrumental parameters, to experimental data. This process relies on the non-linear least squares method and necessitates reasonable initial approximations of various free parameters, including peak shape, unit cell dimensions, and atomic coordinates within the crystal structure [23]. At its core, the Rietveld refinement method employs a least squares approach to iteratively refine a theoretical line profile until it aligns with the measured profile. The success of the refinement hinges on the data quality, the accuracy of the initial model approximations, and the expertise of the user [24].

4.2 Sensing instruments

All the electrochemical and resistive sensing measurements have been conducted using electrochemical workstation (CHI6054E) and semiconductor parametric analyzer (Agilent 4156C). The semiconductor parametric analyzer was connected with custom made heavy metal ion sensing set up. All the description of the instruments has been given below.

4.1.3 Electrochemical workstation

An electrochemical workstation provides several techniques, including cyclic voltammetry, linear sweep voltammetry, differential pulse voltammetry, square wave voltammetry, chronoamperometry, and impedance spectroscopy. These techniques are often accompanied by windows-based software and integrated digital CV simulators and impedance simulation and fitting programs. These features provide powerful tools for understanding reaction kinetics, trace level analysis, fundamental research, corrosion, energy conversion and storage studies. Electrochemical studies have several applications in multiple fields, and hence a clear idea of the electrochemical characterization techniques is a must because they help in understanding the basic electrochemistry of a substance [25]. Electrochemical workstations can also be used for sensing through the use of electrochemical biosensors, which provide an attractive means to analyze the content of a biological sample due to the direct conversion of a biological event to an electronic signal [26]. Electrochemical workstations have a wide range of applications in fields such as electrochemical energy storage, electrochemical sensors, biochemistry and biosensing, and materials science [27].

4.1.3.1 Composition of electrochemical workstation

Electrochemical workstations typically consist of essential components, including electrodes, electrochemical cells, potentiometers, electrochemical analysis instruments, computers with dedicated software, and solution preparation and processing equipment.

- **Electrodes**

Electrodes play a crucial role in electrochemical workstations, where they can be categorized as either two-electrode or three-electrode systems, with the latter being more commonly employed. In the three-electrode system, three distinct electrodes are utilized: the working electrode (WE), the reference electrode (RE), and the counter/auxiliary electrode (CE). The working electrode serves as the primary site for the electrochemical reaction and is typically composed of a precious metal, such as platinum or gold, that is coated with a specific electrocatalyst to enhance the reaction efficiency. The reference electrode ensures precise and repeatable potential measurements by providing a reference potential. As for the counter/auxiliary electrode, its role involves current transfer, polarization, and activation of

the working and reference electrodes during electrochemical experiments, thereby enabling accurate control of electrochemical reactions.

- **Electrochemical cell**

Equipment used for holding electrodes and analyte solution; obtainable as a single electrode cell, double electrode cell, etc.

- **Computers and Software**

For collecting and interpreting information about electrochemical reactions, as well as for processing data and conducting statistical analysis.

- **Solution preparation and handling equipment**

All of these components come together to form the electrochemical workstation, which allows for accurate monitoring and control of electrochemical processes.

4.1.3.2 Electrochemical sensing measurement

Electrochemical measurements were conducted using a three-electrode setup, as shown in the figure. The electrochemical cell consisted of a thin film Ni_2O_3-deposited graphite sheet as the working electrode, platinum wire as the reference electrode, and an Ag/AgCl glass electrode as the counter electrode. The electrodes were connected to the potentiostat CHI6054E. Cyclic voltammetry (CV) was used to perform the electrochemical measurements, with a scan rate of 100 mV s^{-1} and a potential window ranging from -0.5 V to 0.8 V. The baseline was measured using deionized water. Five different concentrations of Cu(II) ion were measured, and all measurements were performed by dipping the reference electrode, counter electrode, and the Ni_2O_3 thin film portion (22 mm x 5 mm) of the working electrode.

Figure 4.4: (a) Electrochemical workstation (CHI6054E), (b) Electrochemical cell and electrode setup

4.1.4 Resistive sensing setup

The resistive heavy metal ion sensing setup used in this study was custom-made two electrode system for the purpose of detecting heavy metal ions and gases. The setup comprises components like electrodes, a sensing chamber, a reference electrode, and a measurement system. The device is placed inside the sensing chamber. The electrodes, positioned within the sensing chamber. To measure the electrical response of the sensing material, the setup is connected to a semiconductor parameter analyzer, specifically the Agilent 4156C. The connection between the custom sensing setup and the Agilent 4156C is established through a computer. The parameter analyzer is configured to apply voltage.

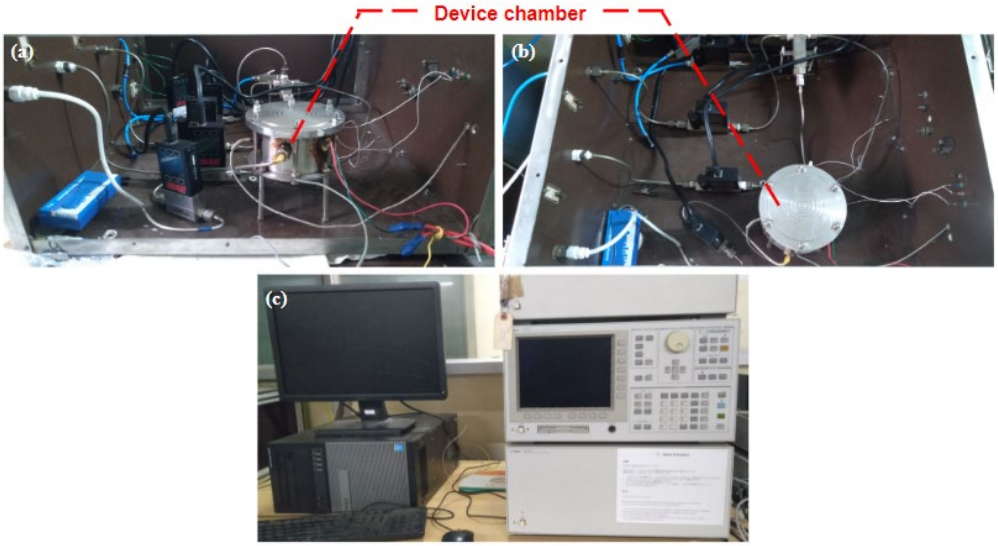

Figure 4.5: Custom-made heavy metal ion sensing setup (a) side view (b) top view, (c) semiconductor parameter analyzer (Agilent 4156C)

4.1.4.1 Resistive sensing measurement

Resistive measurements were conducted in the custom-made two-electrode setup. The device was placed inside the device chamber. The real-time change of the resistance was measured using the semiconductor parametric analyzer (Agilent 4156 C) (mentioned in details in section 4.1.4). The baseline resistance was set by using deionized water. Five different concentrations of analyte ion (0.01 ppm, 0.1 ppm, 1 ppm, 10 ppm and 100 ppm) were measured. All the measurements were performed by dropping 3 µL of each concentration. The response was calculated using the following formula.

$$Response = \frac{R_0}{R} \ (in\ times) \qquad (4.7)$$

R_0 is the base resistance (without analyte ion in the solution) and R is the resistance of the analyte solution.

References

[1] I. Khan, K. Saeed, and I. Khan, "Nanoparticles: Properties, applications and toxicities," Arabian journal of chemistry, vol. 12, no. 7, pp. 908-931, 2019.

[2] A. Mayeen, L. K. Shaji, A. K. Nair, and N. Kalarikkal, "Morphological characterization of nanomaterials," in Characterization of Nanomaterials: Elsevier, 2018, pp. 335-364.

[3] J. A. Adekoya, K. O. Ogunniran, T. O. Siyanbola, E. O. Dare, and N. Revaprasadu, "Band structure, morphology, functionality, and size-dependent properties of metal nanoparticles," Noble and Precious Metals—Properties, Nanoscale Effects and Applications; Seehra, M., Bristow, AD, Eds, pp. 15-42, 2018.

[4] M. S. Chavali and M. P. Nikolova, "Metal oxide nanoparticles and their applications in nanotechnology," SN applied sciences, vol. 1, no. 6, p. 607, 2019.

[5] R. P. R. Senthil Prabhu, M. Vijay and G.R. Kaviya Vikashini, "Field Emission Scanning Electron Microscopy (Fesem) with A Very Big Future in Pharmaceutical Research," International Journal of Pharmacy and Biological Sciences, vol. 11 , pp. 183-187, 2021.

[6] https://www.britannica.com/science/Bragg-law

[7] http://hyperphysics.phy-astr.gsu.edu/hbase/quantum/xtube.html

[8] P. Scherrer, "Nachr Ges wiss goettingen," Math. Phys., vol. 2, pp. 98-100, 1918.

[9] U. Holzwarth and N. Gibson, "The Scherrer equation versus the'Debye-Scherrer equation'," Nature nanotechnology, vol. 6, no. 9, pp. 534-534, 2011.

[10] A. K. Deb and P. Chatterjee, "Microstrain and lattice disorder in nanocrystalline titanium dioxide prepared by chemical route and its relation with phase transformation," Journal of Theoretical and Applied Physics, vol. 14, pp. 285-293, 2020.

[11] S. Dolabella, A. Borzì, A. Dommann, and A. Neels, "Lattice Strain and Defects Analysis in Nanostructured Semiconductor Materials and Devices by High-Resolution X-Ray Diffraction: Theoretical and Practical Aspects," Small methods, vol. 6, no. 2, p. 2100932, 2022.

[12] Q. Wang, H. Xue, B. Zhang, and Y. Chong, "Observation of protected photonic edge states induced by real-space topological lattice defects," Physical Review Letters, vol. 124, no. 24, p. 243602, 2020.

[13] Y. Zhao and J. Zhang, "Microstrain and grain-size analysis from diffraction peak width and graphical derivation of high-pressure thermomechanics," Journal of applied Crystallography, vol. 41, no. 6, pp. 1095-1108, 2008.

[14] W. Woo, T. Ungár, Z. Feng, E. Kenik, and B. Clausen, "X-ray and neutron diffraction measurements of dislocation density and subgrain size in a friction-stir-welded aluminum alloy," Metallurgical and Materials Transactions A, vol. 41, pp. 1210-1216, 2010.

[15] J. Madhavi, "Comparison of average crystallite size by X-ray peak broadening and Williamson–Hall and size–strain plots for VO^{2+} doped ZnS/CdS composite nanopowder," SN Applied Sciences, vol. 1, no. 11, p. 1509, 2019.

[16] G. A. Yakaboylu, N. Gupta, E. M. Sabolsky, and B. Mishra, "Mineralogical characterization and macro/microstrain analysis of the Marcellus shales," International Journal of Rock Mechanics and Mining Sciences, vol. 134, p. 104442, 2020.

[17] R. Das and S. Sarkar, "Determination of intrinsic strain in poly (vinylpyrrolidone)-capped silver nano-hexapod using X-ray diffraction technique," Current Science, pp. 775-778, 2015.

[18] D. Balzar and H. Ledbetter, "Voigt-function modeling in Fourier analysis of size-and strain-broadened X-ray diffraction peaks," Journal of Applied Crystallography, vol. 26, no. 1, pp. 97-103, 1993.

[19] B. Warren and B. Averbach, "The separation of cold-work distortion and particle size broadening in X-ray patterns," Journal of applied physics, vol. 23, no. 4, pp. 497-497, 1952.

[20] R. Jacob and J. Isac, "X-ray diffraction line profile analysis of $Ba_0.6Sr_0.4FexTi_{(1-x)}$ O3-δ,(x= 0.4)," Int. J. Chem. Stud, vol. 2, pp. 12-21, 2015.

[21] V. Mote, Y. Purushotham, and B. Dole, "Williamson-Hall analysis in estimation of lattice strain in nanometer-sized ZnO particles," Journal of theoretical and applied physics, vol. 6, pp. 1-8, 2012.

[22] T. Runcevski and C. M. Brown, "The Rietveld refinement method: Half of a century anniversary," vol. 21, ed: ACS Publications, 2021, pp. 4821-4822.

[23] N. Döbelin, R. Archer, and V. Tu, "A free and open-source solution for Rietveld refinement of XRD data from the CheMin instrument onboard the Mars rover Curiosity," Planetary and Space Science, vol. 224, p. 105596, 2022.

[24] N. Sahu and S. Panigrahi, "Mathematical aspects of Rietveld refinement and crystal structure studies on $PbTiO_3$ ceramics," Bulletin of Materials Science, vol. 34, pp. 1495-1500, 2011.

[25] Y. S. Choudhary, L. Jothi, and G. Nageswaran, "Electrochemical characterization," in Spectroscopic Methods for Nanomaterials Characterization: Elsevier, 2017, pp. 19-54.

[26] D. Grieshaber, R. MacKenzie, J. Vörös, and E. Reimhult, "Electrochemical biosensors-sensor principles and architectures," Sensors, vol. 8, no. 3, pp. 1400-1458, 2008.

[27] Z. Zhou, J. Wang, G. Li, Y. Chen, T. Xu, and X. Zhang, "Wireless USB-like electrochemical platform for individual electrochemical sensing in microdroplets," Analytica Chimica Acta, vol. 1197, p. 339526, 2022.

CHAPTER 5

5 Results and discussions

This section presents the compilation of deductions and performance analysis of the conducted experiments. The chapter includes discussions on the relevant characterizations of the synthesized pure Ni_2O_3 and its doped counterparts and the analysis of the obtained results. It is divided into two main sections: characterization analysis and sensor performance analysis.

5.1 Characterization analysis

In the following sections, the obtained results will be discussed, and an analysis of the XRD patterns and FESEM images will be provided. By synergistically employing these characterization techniques, valuable insights will be revealed regarding the structural and morphological features of pure and metal-doped Ni_2O_3. Through comprehensive analysis, the presence of doping will be confirmed, and further elucidation will be achieved using Rietveld analysis.

5.1.1 Structural and morphological analysis

For the morphological and structural analysis of Ni_2O_3, X-ray diffraction (XRD) is performed. The method and instrument are described in detail in the section 5.1.1. Microstrain and crystallite size are determined from the Williamson-Hall plot, size-strain plot, and Rietveld analysis, and these parameters are compared.

5.1.1.1 X-ray diffraction (XRD) analysis

The crystalline structure of the sensing material was performed by X-ray diffraction. The diffraction pattern of pure Ni_2O_3 and hydrothermally synthesized metal (Cu and Fe) doped Ni_2O_3 is shown in Figure 4.1 (a). The obtained diffraction peaks were at 27.66^o, 32.10^o, 45.82^o, 56.79^o and 66.56^o which are readily indexed with the planes (101), (002), (111), (202) and (004) respectively. The peaks were matched with ICDD (The International Centre for Diffraction Data) card Number 14-0481, CAS (Chemical Abstracts Service) Number 1314-06-3. Figure 4.1 (b) shows the peak shift of the doped material with respect to

pure Ni_2O_3. The peak shift of 5% Cu and 5% Fe doped Ni_2O_3 is approximately 0.086° and 0.2°, respectively. The possible cause of the peak shift is the strain generated due to doping. Structural deformity occurs due to the introduction of Cu^{2+} and Fe^{2+} ions in place of Ni^{2+} ions within the Ni_2O_3 lattice. Cu^{2+}, Fe^{2+}, and Ni^{2+} ions have different ionic radii, resulting in the generation of microstrain in the crystal lattice. The right shift of the XRD peak shows the generated microstrain is compressive type. The right shift of the XRD peak indicates that the generated microstrain is of the compressive type.

5.1.1.2 Rietveld analysis

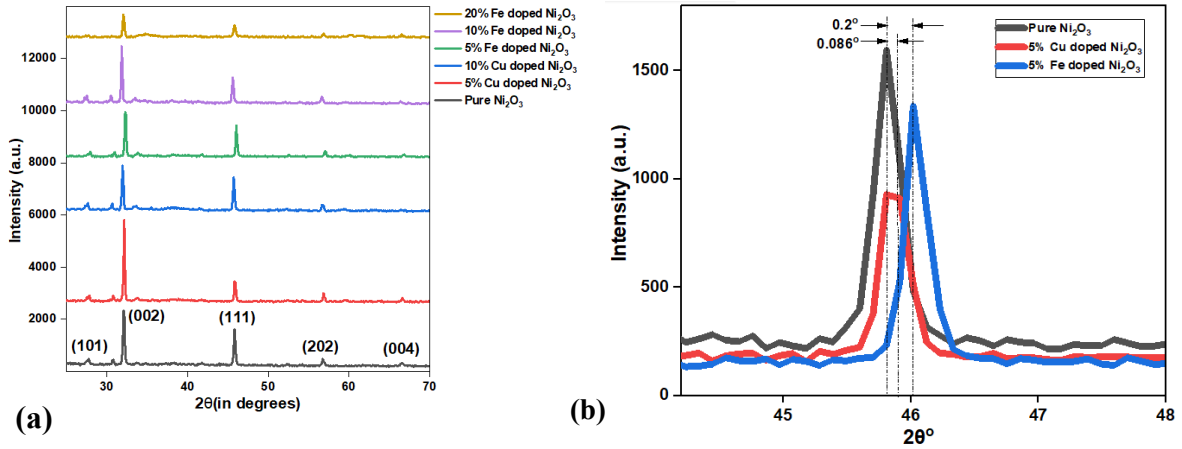

Figure 5.1: (a) XRD plot of pure, Cu-doped Ni_2O_3 and Fe-doped Ni_2O_3, (b) Peak shift for doped Ni_2O_3 in comparison to pure Ni_2O_3

Rietveld analysis, a robust method for refining crystal structures from X-ray diffraction (XRD) data, is extensively described in Section 4.1.2.5. This powerful technique allows for the determination of accurate crystallographic parameters, such as lattice constants, crystallite size, microstrain etc. In this study, the Rietveld refinement was carried out using the MAUD (Material Analysis Using Diffraction) software package. MAUD is a widely utilized program in analyzing crystal structures from XRD data. It employs the Rietveld method, which involves iteratively fitting the observed XRD pattern with a calculated pattern using a trial crystal structure, refining various parameters until an optimized fit is achieved. The refinement process involves adjusting parameters such as atomic positions, thermal vibrations (B-factors), scale factors, and background contributions to minimize the discrepancy between the observed and calculated diffraction patterns. Additionally, various instrumental parameters, including zero error, sample displacement, and instrumental resolution, are considered during the refinement process to account for

experimental factors. Figure 4.2 depicts the fitting of XRD data using the MAUD software. The crystal structures obtained from the Rietveld refinement are presented in Table 5.1.

Table 5.1: Data of Rietveld refinement

Sample	Crystal size (in nm)	Microstrain	Cell length, a (in Å)	Cell volume (in $Å^3$)	Goodness of fit
Pure Ni_2O_3	170.846	1.40×10^{-04}	5.66	181.37	1.53
Cu-doped Ni_2O_3 (5%)	257.86	7.10×10^{-04}	5.65	180.37	1.66
Cu-doped Ni_2O_3 (10%)	344.979	1.33×10^{-03}	5.64	179.63	1.85
Cu-doped Ni_2O_3 (20%)	Phase not obtained				
Cu-doped Ni_2O_3 (30%)	Phase not obtained				
Cu-doped Ni_2O_3 (50%)	Phase not obtained				
Cu-doped Ni_2O_3 (70%)	Phase not obtained				
Fe-doped Ni_2O_3 (5%)	275.72	8.04×10^{-04}	5.65	180.18	1.60
Fe-doped Ni_2O_3 (10%)	391.3	1.12×10^{-03}	5.64	179.78	1.64
Fe-doped Ni_2O_3 (20%)	244.293	2.10×10^{-03}	5.64	179.76	1.26
Fe-doped Ni_2O_3 (30%)	Phase not obtained				
Fe-doped Ni_2O_3 (50%)	Phase not obtained				
Fe-doped Ni_2O_3 (70%)	Phase not obtained				

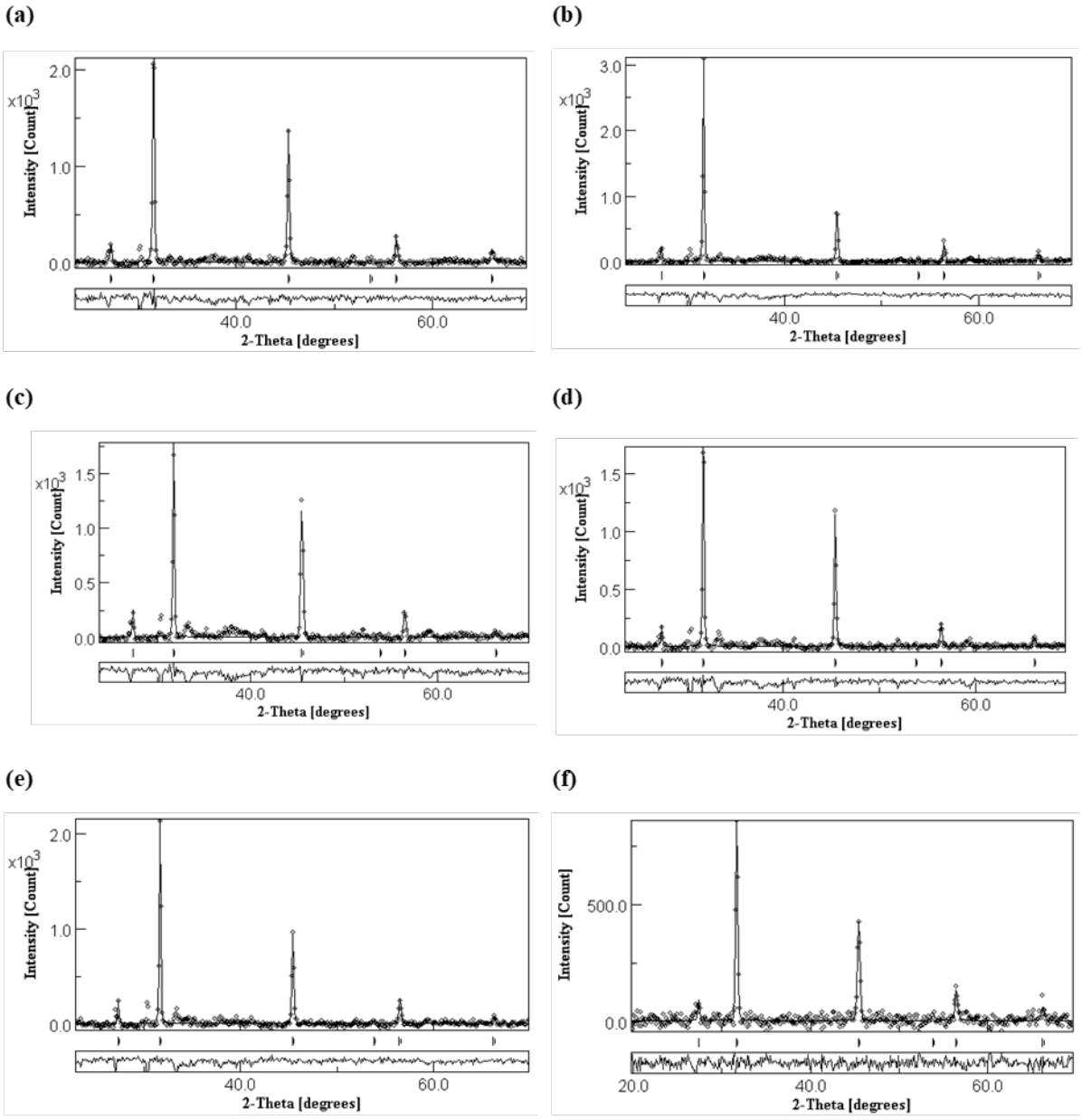

Figure 5.2: Rietveld refinement of (a) Ni_2O_3, (b) 5% Cu-doped Ni_2O_3, (c) 10 % Cu-doped Ni_2O_3, (d) 5% Fe-doped Ni_2O_3, (e) 10 % Fe-doped Ni_2O_3, and (f) 20 % Fe-doped Ni_2O_3

5.1.1.3 Comparison of crystallite size and microstrain

Table 5.2 showcases the changes in crystallite size by varying the doping concentration, as obtained from various analytical techniques. On the other hand, Table 5.3 presents the alterations in microstrain achieved through the same doping variations, as determined by different analytical methods. In Figure 5.3 (a) and (b), bar graphs are plotted to demonstrate the crystallite size of pure (0% doped), 5%, 10%, and 20% (Fe) doped samples. The values are obtained from the Rietveld refinement, Williamson-Hall (W-H) plot, Scherrer equation, and size-strain analysis techniques. This comprehensive representation allows for a clear comparison of the crystallite sizes across different doping concentrations and analytical approaches.

Table 5.2: Comparison of particle size from Scherrer equation, Williamson-Hall plot, and Size-strain plot

Sample	Particle size from Scherrer equation (nm)	Particle size from W-H plot (nm)	Particle size from Size-strain plot (nm)	Particle size from Rietveld analysis (nm)
Pure Ni_2O_3 (0%)	97.425	89.913	56.546	170.846
Cu-doped Ni_2O_3 (5%)	134.008	174.103	136.566	257.86
Cu-doped Ni_2O_3 (10%)	128.122	166.452	166.644	344.979
Fe-doped Ni_2O_3 (5%)	125.505	178.782	180.938	275.72
Fe-doped Ni_2O_3 (10%)	111.252	161.810	231.616	391.3
Fe-doped Ni_2O_3 (20%)	101.480	130.414	79.104	244.293

For both Cu and Fe-doped Ni_2O_3, it can be observed that the crystallite size increases with increasing doping concentration, as evident from the Rietveld refinement and size-strain plot. However, according to the W-H plot and Scherrer equation, the crystallite size increases up to 5% doping and then starts to decrease (Shown in Figure 4.3 (a) and (b)).

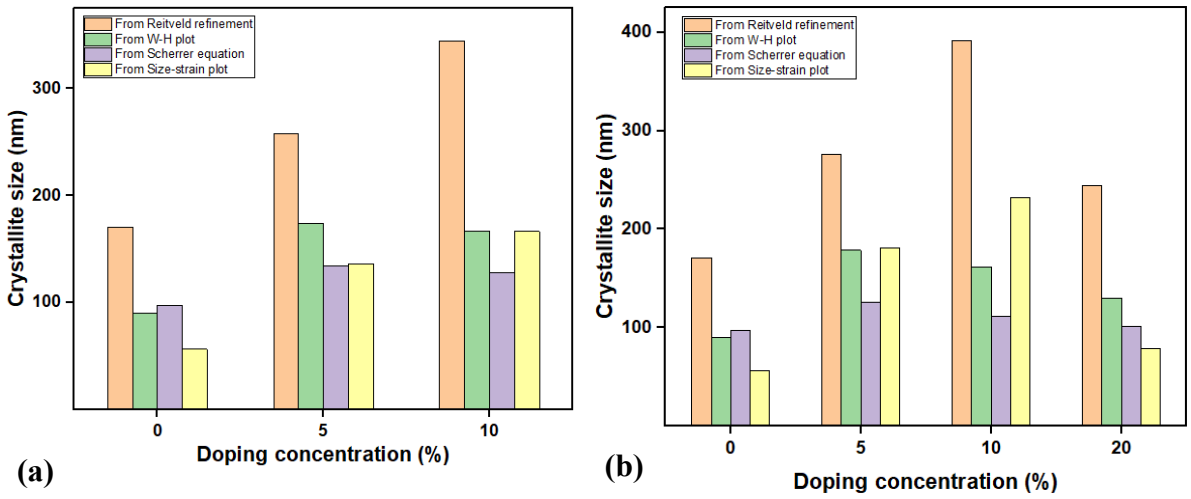

Figure 5.3: Variation of crystallite size of Ni_2O_3 in comparison with different doping concentrations of (a) Cu, (b) Fe, obtained from Rietveld refinement, W-H plot, Scherrer equation and size strain plot

Table 5.3: Comparison of particle size from Scherrer equation, Williamson-Hall plot, and Size-strain plot

Sample	Microstrain from W-H plot	Microstrain from Size-strain plot	Microstrain from Rietveld refinement
Pure Ni_2O_3 (0 %)	2.40×10^{-3}	5.36×10^{-3}	1.40×10^{-04}
Cu-doped Ni_2O_3 (5%)	9.90×10^{-4}	6.85×10^{-3}	7.10×10^{-04}
Cu-doped Ni_2O_3 (10%)	1.61×10^{-3}	2.44×10^{-3}	1.33×10^{-03}
Fe-doped Ni_2O_3 (5%)	7.88×10^{-4}	3.31×10^{-3}	8.04×10^{-04}
Fe-doped Ni_2O_3 (10%)	1.57×10^{-3}	3.00×10^{-3}	1.12×10^{-03}
Fe-doped Ni_2O_3 (20%)	1.52×10^{-3}	1.90×10^{-3}	2.10×10^{-03}

According to Figure 5.4 (a) and (b), in the W-H plot, microstrain initially decreases until 5% doping and then increases for both Fe and Cu doping. In the size-strain plot, Cu-doped samples show a decrease in microstrain at 5% doping, while Fe-doped samples exhibit a steady decreasing trend. Furthermore, Rietveld refinement results indicate that microstrain increases with increasing doping concentration for both Fe and Cu doping.

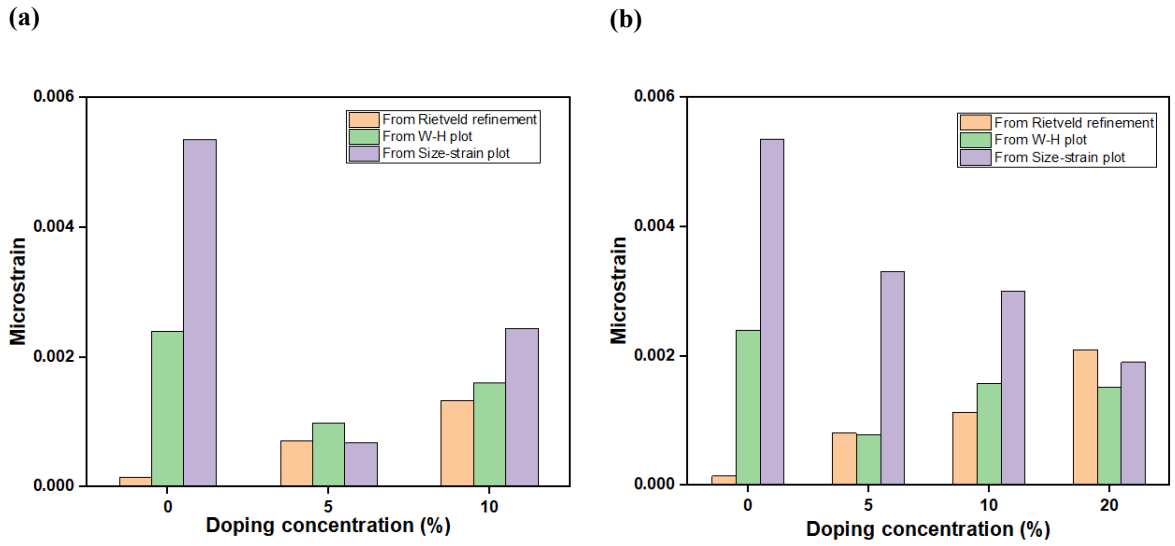

Figure 5.4: Variation of microstrain inside Ni_2O_3 crystal in comparison with different doping concentrations of (a) Cu, (b) Fe, obtained from Rietveld refinement, W-H plot, and size strain plot

5.1.2 FESEM analysis

Figure 5.5 (a) to (e) showcases the FESEM images of all the samples under investigation. Upon careful examination, it becomes apparent that both the pure Ni_2O_3 samples and their copper-doped counterparts do not exhibit any discernible hierarchical morphology (Figure 5.5 (a) to (c)). The surface structure of these samples lacks any distinct features at the microscale.

However, in stark contrast, the iron-doped samples exhibit a striking hierarchical morphology. The FESEM images of the iron-doped samples reveal the presence of intricate structures with multiple levels of organization. The presence of such hierarchical morphology

in the iron-doped samples suggests the influence of iron doping on the surface morphology and highlights its potential role in inducing structural modifications (Figure 5.5 (d) to (e)).

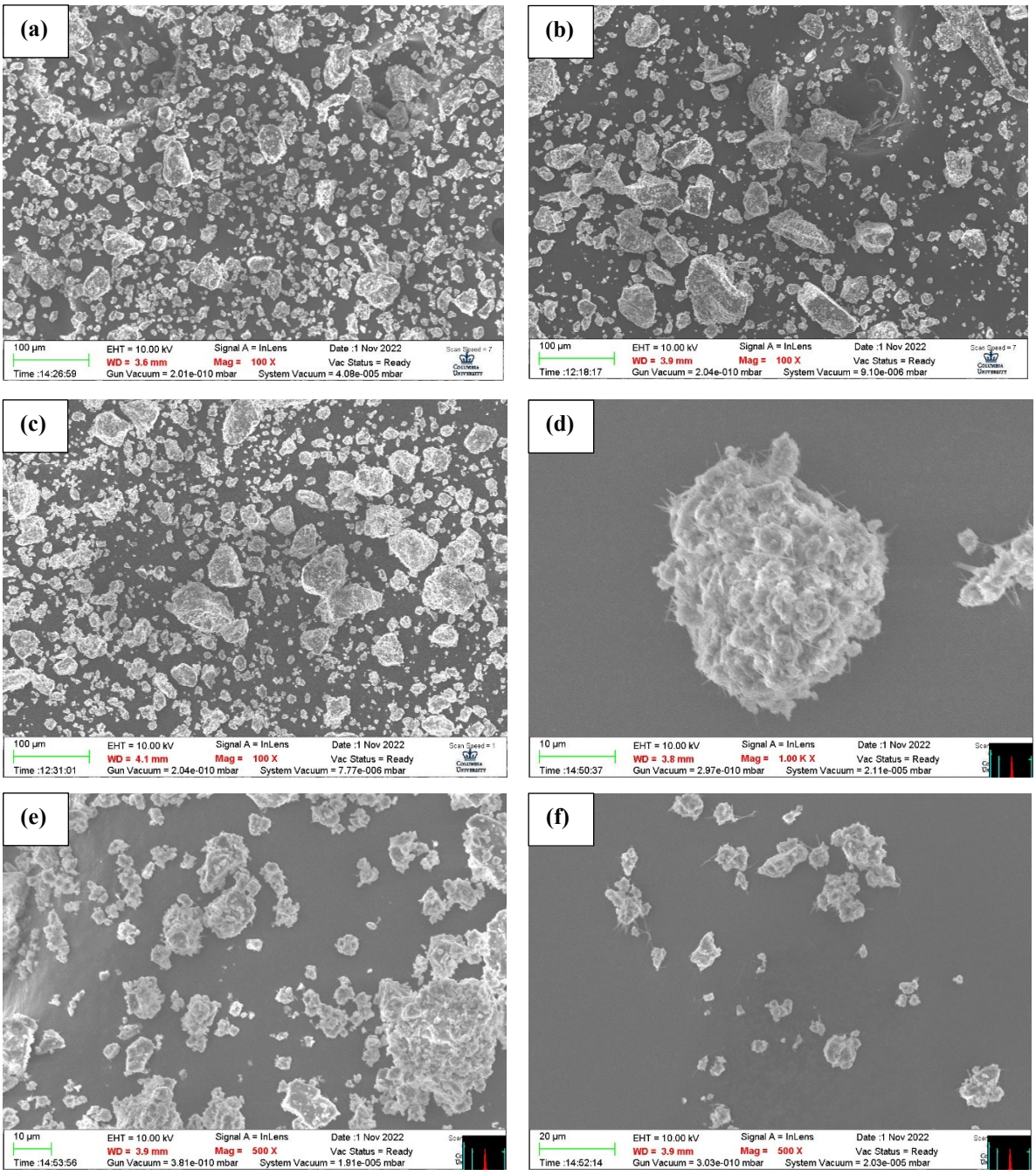

Figure 5.5: FESEM images of (a) Pure Ni_2O_3, (b) 5% Cu, (c) 10% Cu, (d) 5% Fe, (e) 10% Fe and (d) 20% doped Ni_2O_3

5.2 Sensing measurement analysis

Electrochemical (pure Ni_2O_3 based working electrode) and resistive (pure, 5% Fe and Cu doped Ni_2O_3 based device) sensing experiments were performed to further investigate the properties and sensing capabilities of the materials.

5.2.1 Electrochemical sensing

The electrochemical sensing set up is described in detail in section 4.1.3. To investigate the electrochemical sensing capabilities of the samples, cyclic voltammetry (CV) experiments were conducted. The CV technique involved sweeping the potential applied to the samples over a specified range (information given in section 4.1.3.2) and recording the resulting current response. The obtained CV curves provided valuable information about the electrochemical behavior at the electrode-electrolyte interface. Figure 5.6 (a) and (b) display the CV graphs obtained during the electrochemical sensing experiments. These CV curves were recorded while varying the concentration of the target analyte, specifically Cu^{2+} ions, in the electrolyte solution. By increasing the concentration of Cu^{2+} ions, it was observed that the area of the CV curve decreased. This behavior indicates a reduction in the electrochemical activity or reactivity of the samples towards the Cu^{2+} ions with increasing concentration. The decrease in the CV curve's area can be attributed to the formation of surface complexes or adsorption of Cu^{2+} ions on the electrode surface. A single CV cycle took 45 minutes.

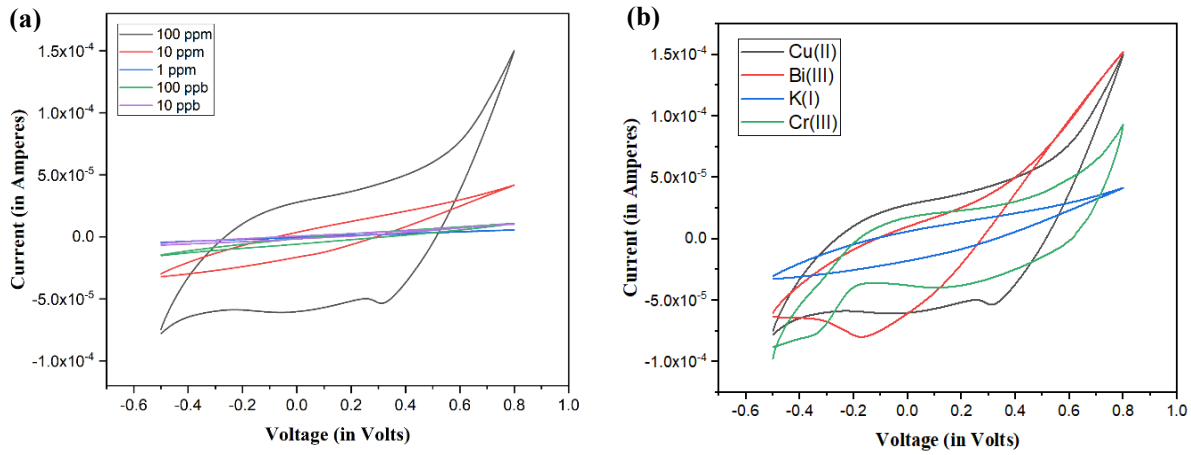

Figure 5.6: (a) CV of different concentration of Cu ion, (b) CV of different ion in 100 ppm

Figure 5.7 (a), (b), and (c) present the relationship between analyte concentration and various response characteristics of the samples. In Figure 5.7 (a), the analyte concentration is plotted against the corresponding response characteristics, such as the amplitude or magnitude of the sensor's response. This graph provides insights into the sensitivity of the samples towards different analyte concentrations. As the concentration of the analyte increases, the response characteristics of the sensor exhibit a corresponding change, allowing

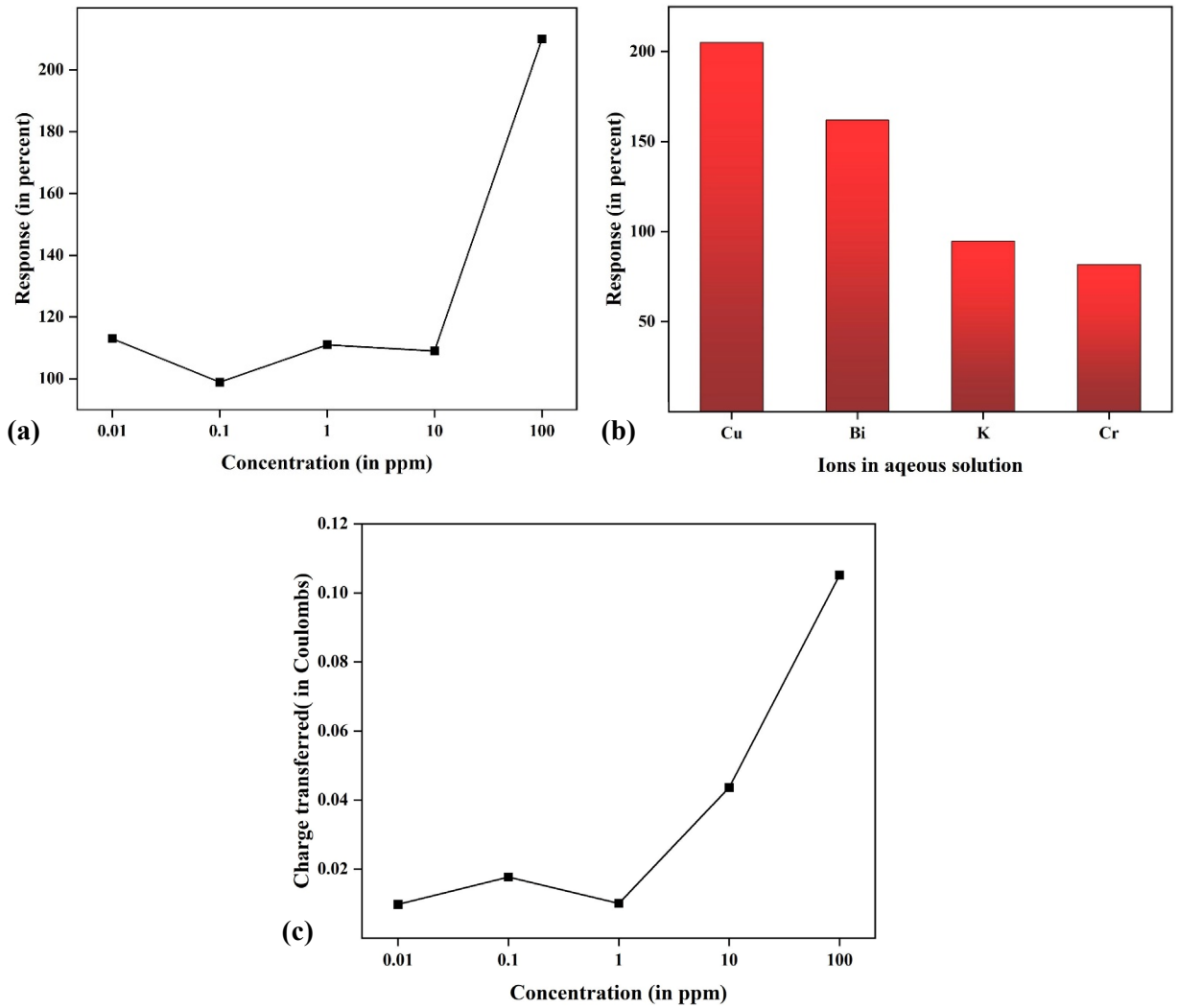

Figure 5.7: (a) Response of different concentrations of Cu(II) ion, (b) Response of different ions of 100 ppm, (c) Amount of charge transferred at different concentration of Cu(II) ion

for quantitative analysis and determination of the analyte concentration. Figure 5.7 (b) showcases the response of the samples when exposed to multiple ions. By plotting the analyte concentration of multiple ion species against the respective sensor response, the selectivity of the sensor shows toward Cu^{2+} ion. In Figure 5.7 (c), the charge transfer characteristics of the samples are depicted with respect to the analyte concentration. This graph illustrates how the

charge transfer, typically measured as current or charge, varies as a function of the analyte concentration.

5.2.2 Resistive sensing

The details of the resistive sensing setup are described in detail in section 4.1.4. This section provides a comprehensive explanation of the experimental apparatus and methodology employed for conducting the resistive sensing experiments. It outlines the configuration of the sensor setup, including the sensing element, measurement circuit, and data acquisition system.

The resistive sensing experiments discussed, pure Ni_2O_3 and 5% Fe-doped Ni_2O_3 based devices were investigated for their response towards Cu^{2+} ions. The measurements aimed to evaluate the sensing capabilities of these samples towards detecting and quantifying Cu^{2+} ions in the surrounding environment. Additionally, a 5% Cu-doped variant of the samples was utilized to detect Bi^{3+} ions. This allowed for the examination of the sensing performance and selectivity of the Cu-doped samples towards Bi^{3+} ions. The analysis included the evaluation of key parameters such as sensitivity, response time, and the relationship between analyte concentration and the resulting resistance change. Five different concentrations of the copper ion (0.01 ppm, 0.1 ppm, 1 ppm, 10 ppm and 100 ppm) dropped on the sensor and the change of resistance was observed after setting the base resistance using deionized water.

5.2.2.1 Cu(II) ion detection

5.2.2.1.1 Pure Ni_2O_3

With an increasing concentration of Cu^{2+} ions in the solution, the resistance of the sensor exhibited a decrease. The maximum response was observed at 100 ppm of Cu(II) ion solution, resulting in a significant resistance change of 38 times, as depicted in Figure 5.8 (c). The detailed sensing data, including the resistance values at different Cu^{2+} ion concentrations, are provided in Table 5.4.

To assess the selectivity of the sensor, it was exposed to 100 ppm solutions of five different ions, that are Cu(II), Cr(III), Ca(II), K(I), Na(I), and Bi(III). The results revealed that the sensor exhibited high selectivity towards Cu(II) ions, as illustrated in Figure 5.8 (d).

The resistance change observed with the Cu(II) ion was significantly higher compared to the other tested ions, indicating the sensor's ability to specifically detect and differentiate Cu(II) ions from the surrounding environment.

In order to determine the response time of the sensor, amperometric measurements were conducted. It was found that the sensor achieved a response time of 5 seconds after the injection of a 100 ppm Cu(II) solution, as shown in Figure 5.8 (a). The staircase plot obtained from amperometric measurements, depicted in Figure 5.8 (b), demonstrates the increasing response of the sensor upon the injection of different concentrations of Cu(II) ions (1 ppm and 10 ppm, respectively). The detailed results presented in Figures 5.8 (a), (b), (c), and (d) provide a comprehensive understanding of the sensor's performance characteristics, including

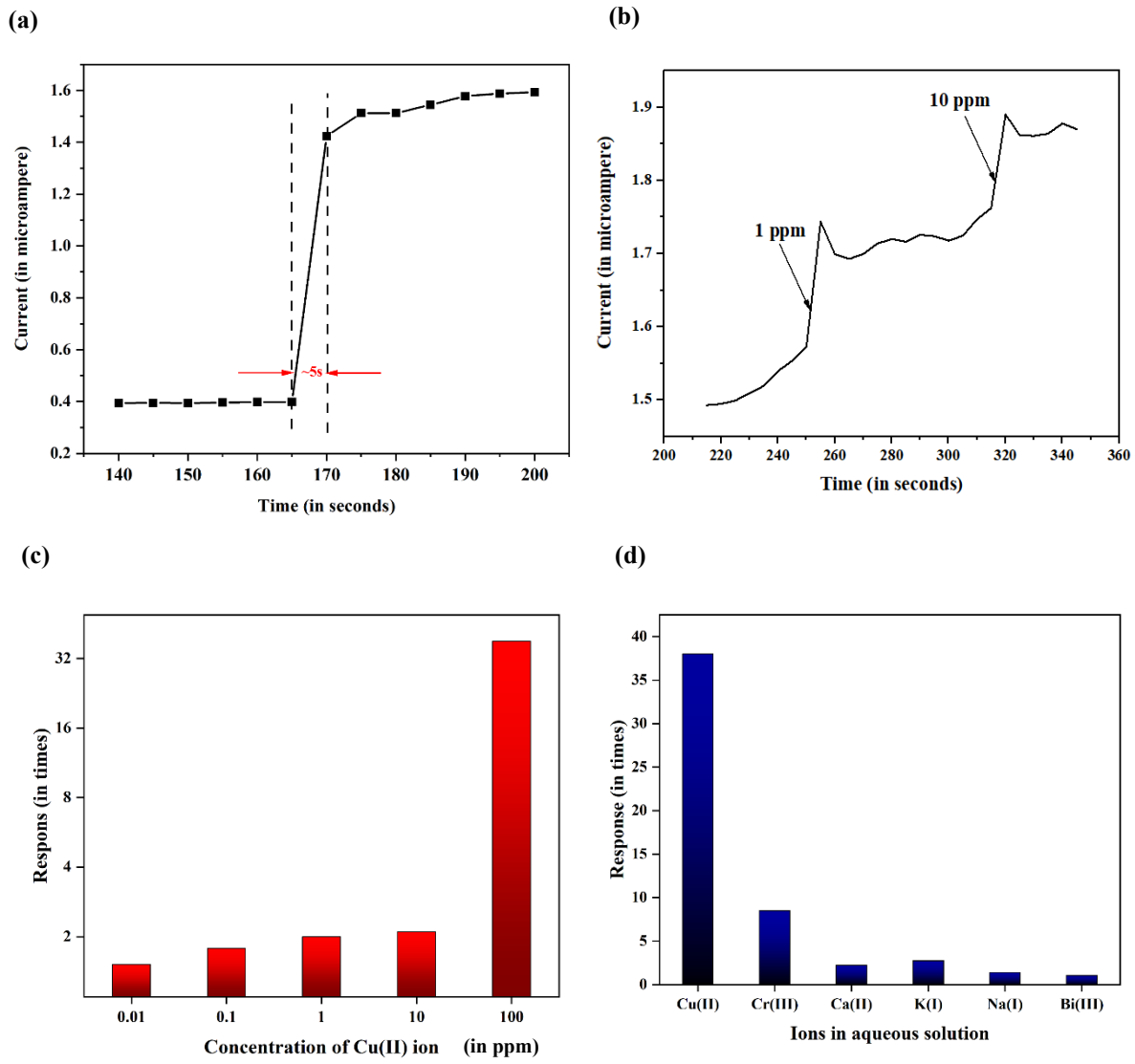

Figure 5.8: (a) Response time, (b) Amperometric plot, (c) Sensing response and, (d) Selectivity (Cu(II) sensing using pure Ni_2O_3-based sensor)

its response to Cu(II) ions at varying concentrations, selectivity towards different ions, and response time.

The I-V characteristics of the sensing device are illustrated in Figure 5.9 (a) to (e). Each curve represents a distinct I-V relationship obtained at different concentrations of Cu(II) ions. All the I-V measurements were conducted within a test window of 0 V to 5 V. The

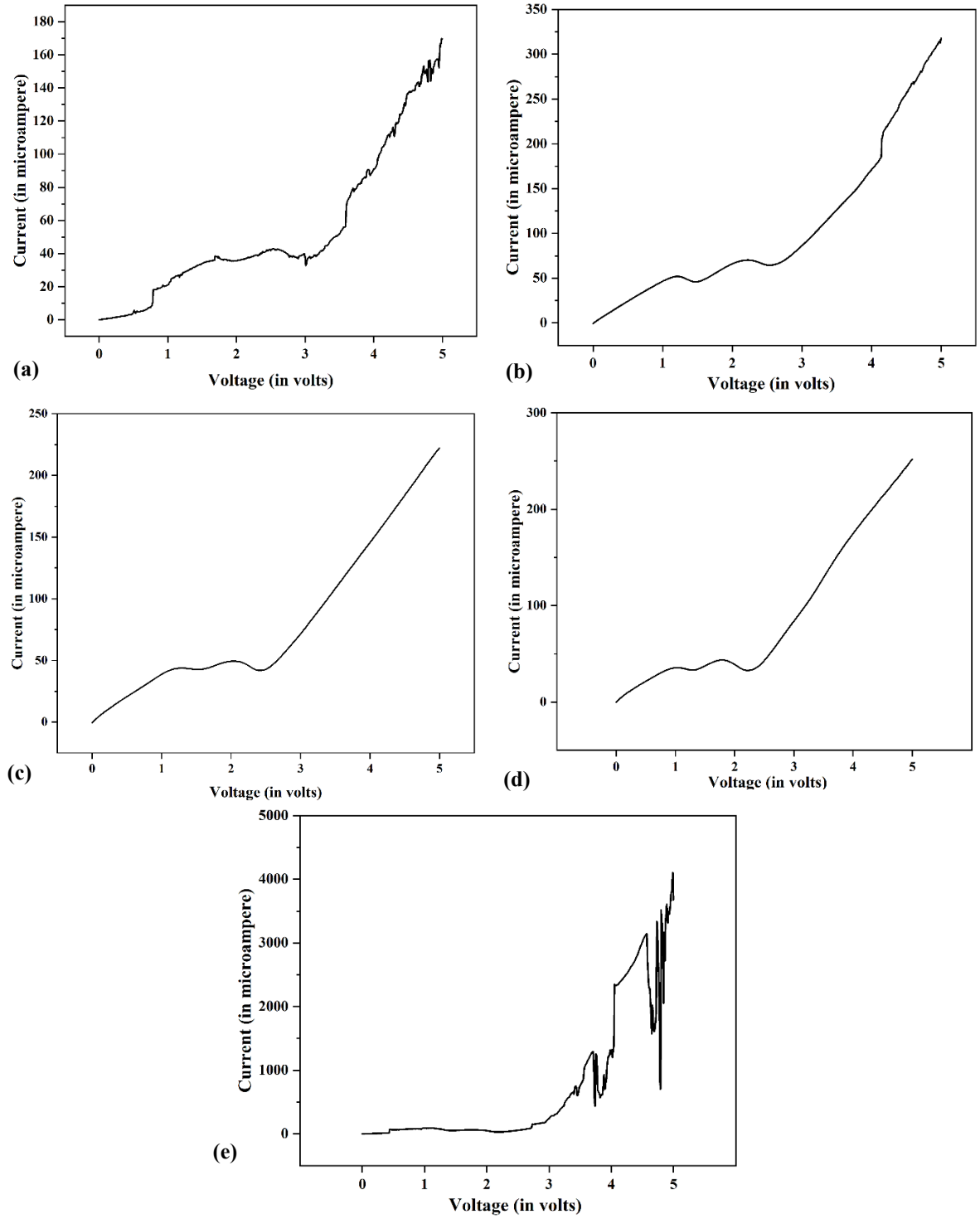

Figure 5.9: I-V characteristics of pure Ni_2O_3-based sensor during measurement of (a) 10 ppb, (b) 100 ppb, (c) 1 ppm, (d) 10 ppm and, (e) 100 ppm Cu(II) ion

resistance is recorded at 5 V bias.

Ni_2O_3 is a wide bandgap p-type semiconductor with a negative surface potential. Majority carriers are holes and minority carriers are electrons. When Cu^{2+} ion was introduced being an oxidizing it takes the electrons from the conduction band and creates more holes. Due to these holes conductivity of the sensor increases and resistance decreases. The electron transfer is shown by the following.

$$Cu^{2+} + 2e^- \rightarrow Cu \qquad (5.1)$$

5.2.2.1.2 Fe-doped Ni_2O_3

Fe-doped Ni_2O_3 demonstrates an enhanced response towards Cu(II) ions compared to pure Ni_2O_3. The maximum response was observed at a concentration of 100 ppm Cu(II) ions, as depicted in Figure 4.10 (a). To evaluate the selectivity of the sensor, it was exposed to 100 ppm solutions of five different ions, including Cu(II), Cr(III), Cd(II), and Ca(II). The results indicated that the sensor exhibited high selectivity towards Cu(II) ions, as illustrated in Figure 4.10 (b). The observed change in resistance with Cu(II) ions was significantly higher compared to the other tested ions. This finding suggests that the sensor possesses the ability to specifically detect and differentiate Cu(II) ions from other ions present in the solution. Amperometric measurements were conducted to determine the response time of the sensor. It was found that the sensor achieved a response time of 5 seconds after the injection of a 100 ppm Cu(II) solution, as shown in Figure 4.10 (c).

These results provide compelling evidence of the enhanced response of iron-doped Ni_2O_3 towards Cu(II) ions compared to pure Ni_2O_3. The selectivity test demonstrates the sensor's ability to distinguish Cu(II) ions from other tested ions, indicating its potential for targeted and accurate detection.

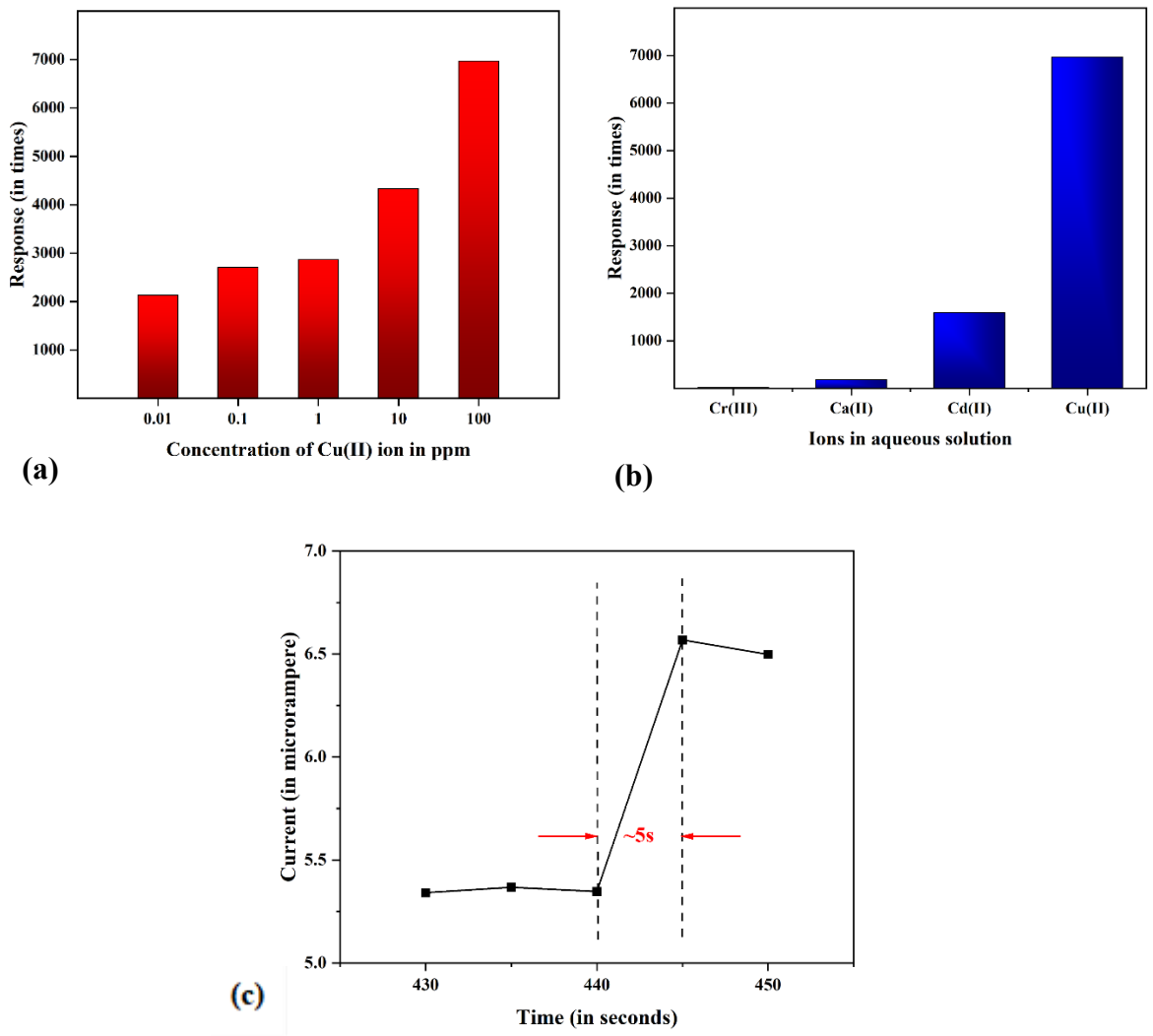

Figure 5.10: (a) Response time, (c) Sensing response and, (d) Selectivity (Cu(II) sensing using 5% Fe-doped Ni_2O_3-based sensor)

5.11 (a) to (e) display the I- characteristics of the Fe doped Ni_2O_3 based sensing device, with each curve representing a unique I-V relationship obtained at varying concentrations of Cu(II) ions. All measurements were performed within a test window spanning from -500 mV to 500 mV. The resistance values were recorded at a bias voltage of 500 mV.

Doping Ni_2O_3 with iron leads to an increase in the number of electrons in the conduction band. The introduction of Cu(II) ions causes the absorption of additional electrons from the conduction band, resulting in the generation of more holes. This increased hole

generation leads to a decrease in the resistance of the device, consequently resulting in an increase in the current.

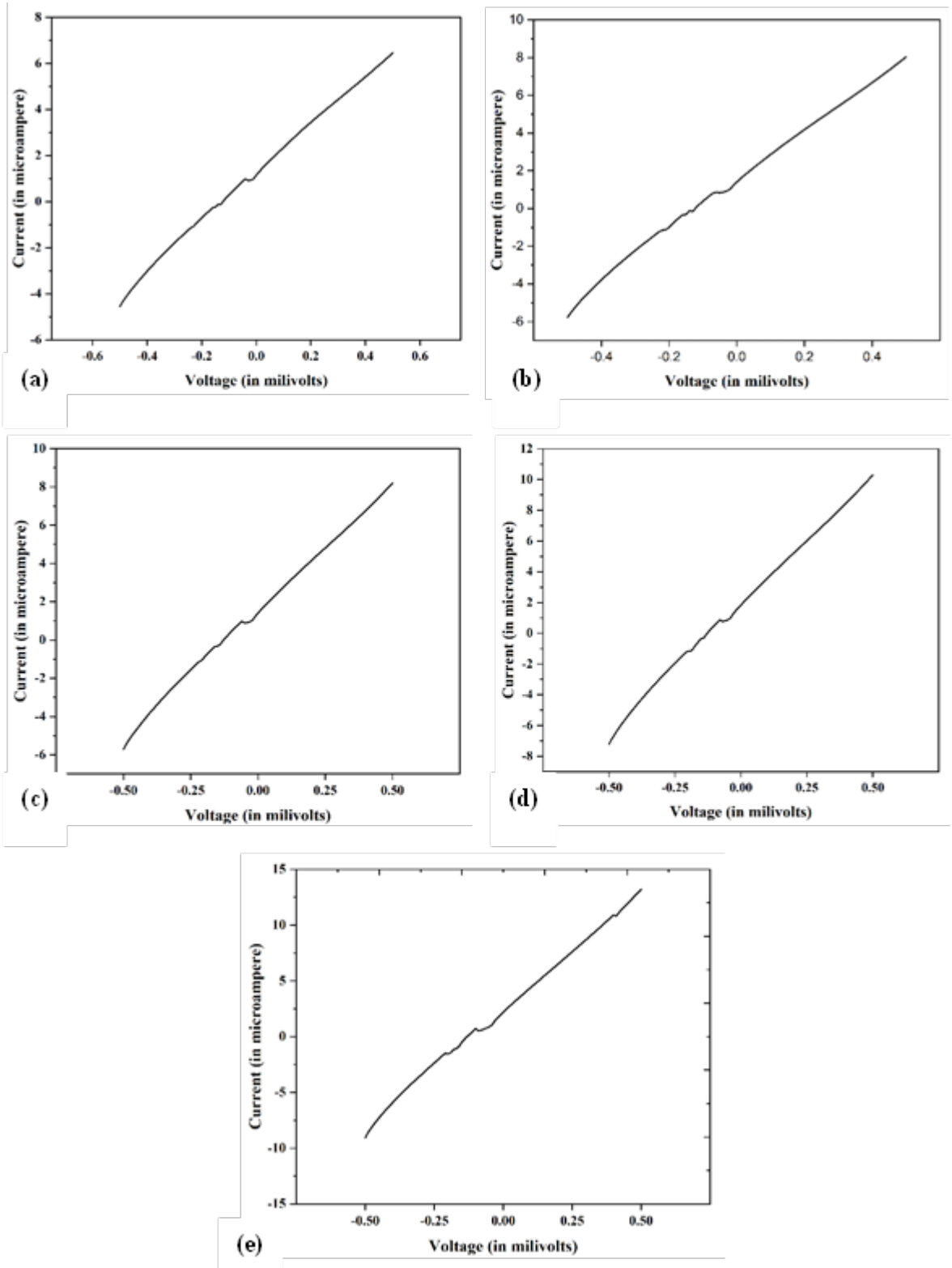

Figure 5.11: I-V characteristics of 5 % Fe-doped Ni_2O_3-based sensor during measurement of (a) 10 ppb, (b) 100 ppb, (c) 1 ppm, (d) 10 ppm and, (e) 100 ppm Cu(II) ion

5.2.2.2 Bi (III) ion detection using Cu-doped Ni_2O_3

Cu-doped Ni_2O_3 exhibited a highly promising and noteworthy response when exposed to Bi^{3+} ions. As the concentration of Bi^{3+} ions increased in the solution, the sensor's resistance showed a decline. The sensor demonstrated its highest sensitivity at a concentration of 100 ppm Bi(III) ions, as shown in Figure 5.8 (c). The table provides comprehensive data on the sensor's resistance values at various Bi^{3+} ion concentrations.

To evaluate the sensor's selectivity, it was exposed to 100 ppm solutions containing five different ions: Cu(II), Cr(III), Ca(II), Cd(II), Na(I), and Bi(III). The findings indicated that the sensor exhibited remarkable selectivity towards Cu(II) ions, as depicted in Figure 5.8 (d). The resistance change observed with Bi(III) ions surpassed that of the other tested ions, indicating the sensor's exceptional capability to specifically detect and distinguish Bi(III) ions from the surrounding environment.

To evaluate the response time, amperometric measurements were conducted. The results indicated that the sensor achieved a response time of 5 seconds upon injecting a 100 ppm Bi(III) solution, as depicted in Figure 5.8 (a). This indicates that the sensor can rapidly detect and measure the presence of Bi(III) ions, making it suitable for real-time monitoring and quick analysis. Figure 5.8 (b) presents a staircase plot derived from the amperometric measurements, illustrating the increasing response of the sensor as different concentrations of Bi(III) ions (1 ppm, 10 ppm, and 100 ppm) were injected.

The response time of the sensor, as depicted in Figure 5.8 (a), was determined to be 5 seconds upon exposure to a 100 ppm Bi(III) solution. This indicates that the sensor can rapidly detect and measure the presence of Bi(III) ions, making it suitable for real-time monitoring and quick analysis.

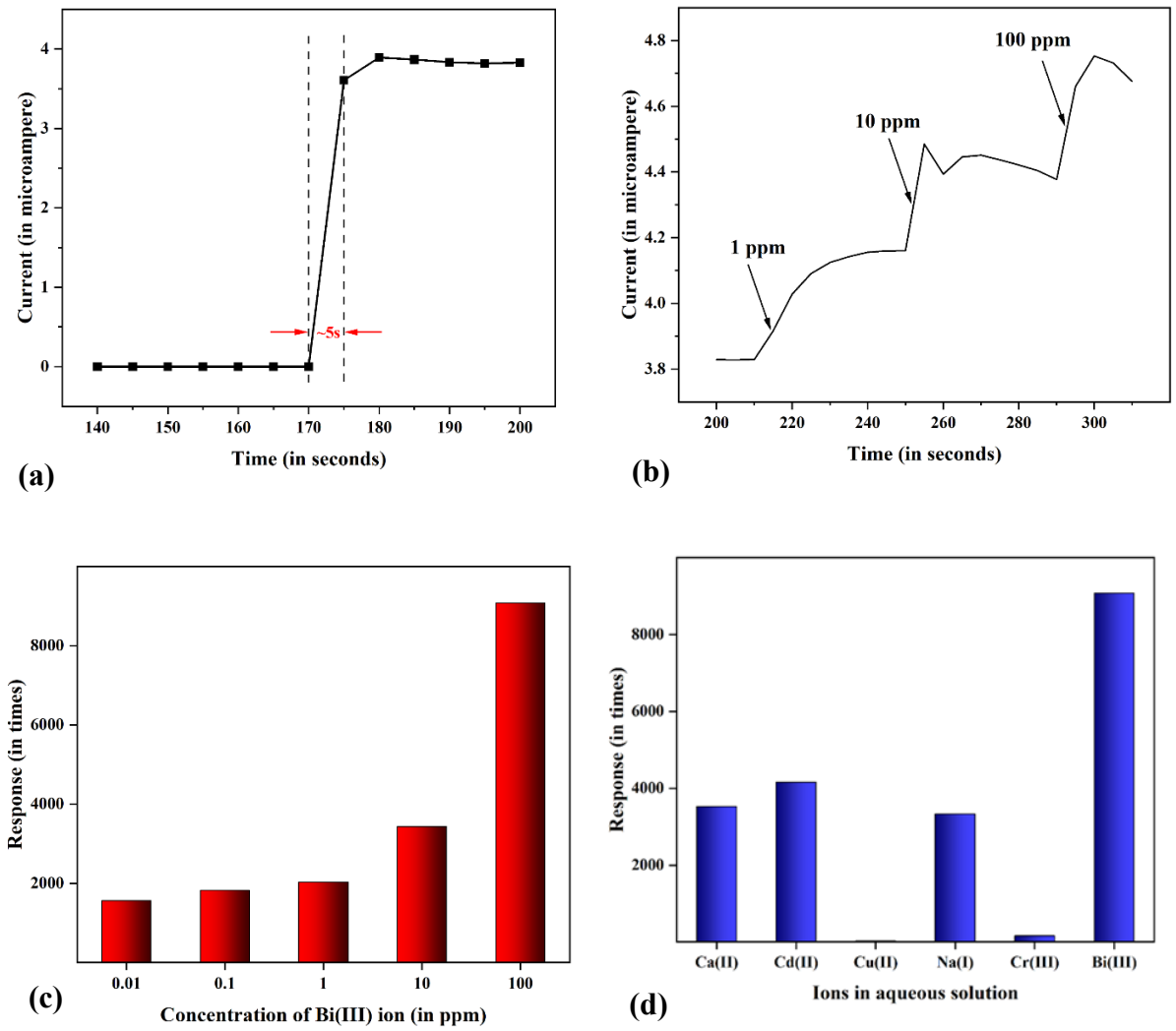

Figure 5.12: (a) Response time, (b) Amperometric plot, (c) Sensing response and, (d) Selectivity (Bi(III) sensing using 5 % Cu-doped Ni_2O_3-based sensor)

The I-V characteristics of the sensing device are showcased in Figure 5.13 (a) to (e), illustrating the relationship between current and voltage. Each curve represents I-V profile obtained at different concentrations of Bi(III) ions. The measurements were conducted within a test range spanning from -500 mV to 500 mV. The resistance values were recorded specifically at a bias of 500 mV.

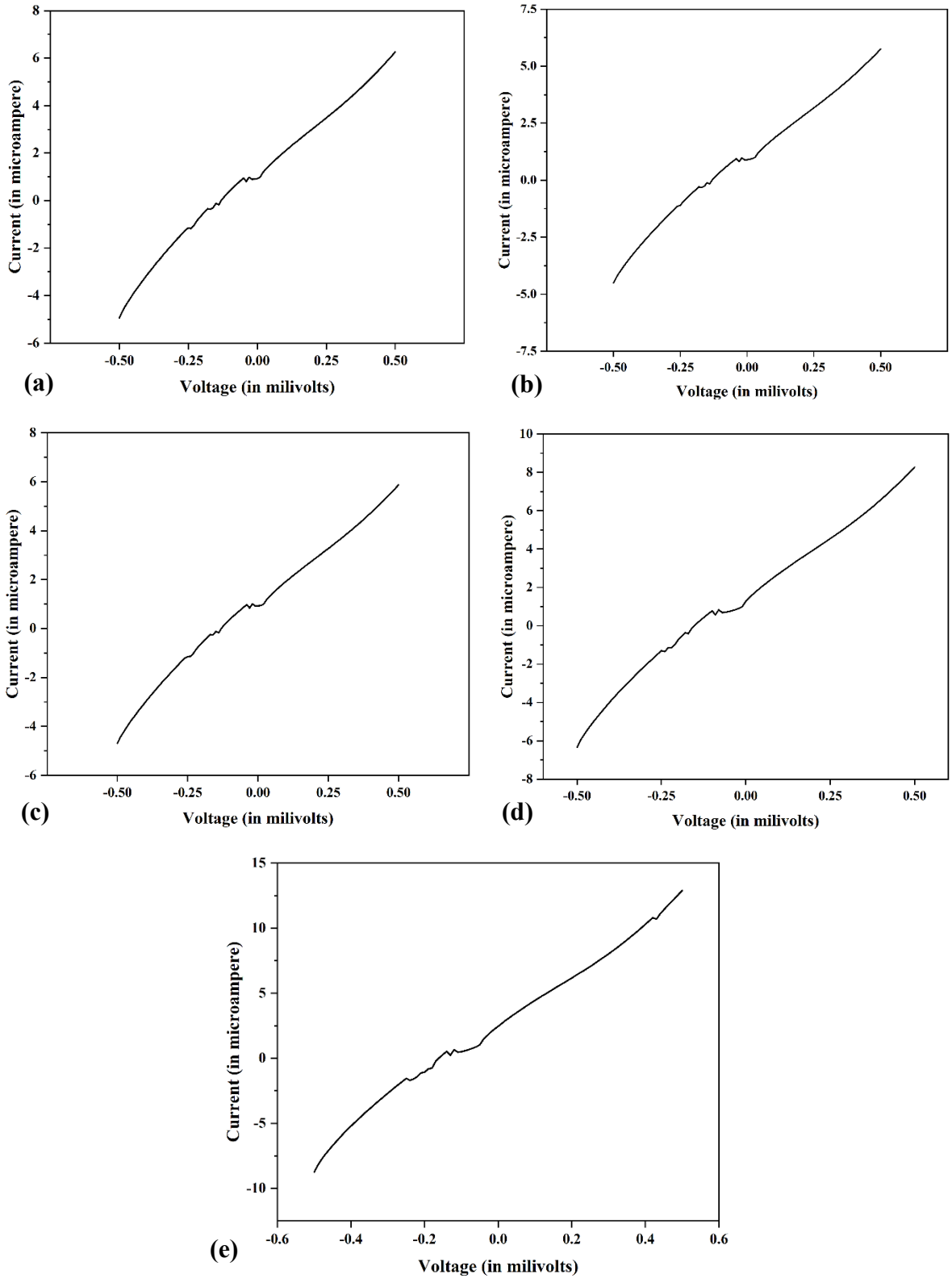

Figure 5.13: I-V characteristics of 5 % Cu-doped Ni_2O_3-based sensor during measurement of (a) 10 ppb, (b) 100 ppb, (c) 1 ppm, (d) 10 ppm and, (e) 100 ppm Cu(III) ion

The addition of Cu as a dopant in Ni_2O_3 results in an augmentation of the electron population in the conduction band. When Bi(III) ions are introduced, they absorb additional electrons from the conduction band, leading to the creation of more holes. This elevated hole generation subsequently leads to a reduction in the device's resistance, resulting in an upsurge in the current. When Bi(III) ions are present in the vicinity of the Cu-doped Ni_2O_3 material, they tend to undergo a redox reaction. The Bi(III) ions act as electron acceptors, absorbing electrons from the conduction band of the material. This electron transfer process leads to the generation of holes within the material. The electron transfer is shown by the following.

$$Bi^{3+} + 3e^- \rightarrow Bi \qquad (5.2)$$

Table 5.4: Comparison of response of the different materials with variation of concentration of analytes

Materials	Analyte measured	Analyte concentration	Resistance of DI water before measurement (KΩ)	Resistance after adding analyte solution (KΩ)	Response (in times)
Pure Ni_2O_3	Cu(II)	100 ppm	38	1	38
		10 ppm	42	20	2.1
		1 ppm	45	22.5	2
		100 ppb	41	23	1.78
		10 ppb	44	29	1.52
5% Fe-doped Ni_2O_3	Cu(II)	100 ppm	265000	38	6973.68
		10 ppm	208000	48	4333.33
		1 ppm	175000	61	2868.85
		100 ppb	168000	62	2709.67
		10 ppb	160000	75	2133.33
5% Cu-doped Ni_2O_3	Bi(III)	100 ppm	345000	38	9078.95
		10 ppm	206000	60	3433.33
		1 ppm	173000	85	2035.30
		100 ppb	146000	80	1825
		10 ppb	136000	87	1563.22

Table 5.5: Properties of the fabricated devices

Device based on	Operating temperature	Operating voltage	Response time (in seconds)
Pure Ni_2O_3	Room temperature	5 V	5
5% Fe-doped Ni_2O_3	Room temperature	500 mV	5
5% Cu-doped Ni_2O_3	Room temperature	500 mV	5

CHAPTER 6

6 Conclusion and future work

In conclusion, this thesis presented the fabrication and characterization of efficient sensors using Ni2O3 and its Fe and Cu-doped variants for the detection of Cu2+ and Bi3+ ions. The synthesized materials were thoroughly characterized using XRD and FESEM, and Rietveld refinement was performed to determine the microstrain generated in the crystal structure due to doping.

Pure Ni2O3 was synthesized using a room temperature chemical synthesis method, while the doped materials were prepared using an in situ hydrothermal method. The fabricated sensors, based on Ni2O3 and its doped variants, were drop-casted on interdigitated electrodes (IDE) to form the sensing platforms.

Contrary to previous knowledge, this work demonstrated that Ni2O3 can be utilized as a resistive sensor for the detection of heavy metal ions. The sensors exhibited remarkable performance, with a fast response time of 5 seconds, which was significantly quicker compared to the electrochemical measurements that took 45 minutes for each sample. Moreover, all the sensors operated at room temperature, making them practical and energy-efficient.

The results revealed that Fe doping of Ni2O3 significantly enhanced the response of the sensor, indicating its potential for improved detection of Cu2+ ions. Additionally, the resistive sensors exhibited selectivity towards the targeted ions, as they displayed negligible responses when exposed to other types of ions, demonstrating their specificity and reliability.

In addition to the aforementioned conclusions, an important observation made in this thesis is the reduced operating voltage for the doped material-based sensors compared to pure Ni2O3. While pure Ni2O3 exhibited a lower response at 5V, the doped variants showed efficient sensing capabilities at a significantly lower operating voltage of 500 mV. This finding indicates that the doped sensors are more energy-efficient, reducing power consumption during detection processes. The lower operating voltage requirement of the doped sensors is a significant advantage as it contributes to energy savings and makes them

more suitable for practical applications. By reducing the voltage, the doped sensors not only demonstrate their enhanced performance and sensitivity but also contribute to a more sustainable and eco-friendly sensing platform.

The findings of this research open up new possibilities for the application of Ni2O3-based sensors as efficient and fast-response devices for heavy metal ion detection. The unexpected resistive sensing behavior of Ni2O3 highlights its potential as a promising material for future sensing applications. The enhanced response observed in Fe-doped Ni2O3 suggests that further investigations into doping strategies could lead to even more sensitive and selective sensors.

This thesis successfully demonstrated the feasibility and efficiency of Ni2O3 and its doped variants as sensing platforms for the detection of Cu2+ and Bi3+ ions. The results provide valuable insights into the development of novel sensor materials and pave the way for future research in the field of heavy metal ion detection, environmental monitoring, and water safety.

Future works

- Explore the potential of other dopants or combinations of dopants to enhance the sensing capabilities of Ni2O3-based sensors.
- Further investigate the doping strategies for Ni2O3 to optimize the sensing performance and selectivity for a wider range of heavy metal ions.
- Study the sensing behavior of doped Ni2O3 sensors under different environmental conditions, such as varying pH levels and temperature, to evaluate their robustness and reliability.
- Explore the integration of doped Ni2O3 sensors into portable or wearable devices for on-site and real-time monitoring of heavy metal ion contamination.